Development of Monoliths with Introduced Straight Microchannels for Applications in Continuous Wastewater Treatment

直状マイクロ流路を導入したモノリス体の開発と連続式廃水処理への応用

Academic Year 2019

Graduate School of Chemical Sciences and Engineering,
Hokkaido University

Kasama URKASAME

Table of Contents

Chapter 1 General Introduction **1**

1.1 Impacts of Soluble Aromatics ⋯ 1

1.2 Treatment Techniques ⋯ 2

1.2.1 Adsorption ⋯ 5

1.2.2 Photocatalysis as Advanced Oxidation Process ⋯ 6

1.3 Configurations of Treatment Systems ⋯ 7

1.3.1 Monolithic Honeycombs ⋯ 8

1.3.2 Microreactors and Microdevices ⋯ 9

1.4 Microhoneycombs ⋯ 10

1.4.1 Ice Templating Method ⋯ 10

1.4.2 Applications of Microhoneycombs ⋯ 13

1.5 Research Objectives ⋯ 14

References ⋯ 16

Part 1 Continuous Photocatalytic Degradation of Organic Compounds in Wastewater Using TiO_2−SiO_2 Microhoneycombs Synthesized by the Ice Templating Method **25**

Chapter 2 TiO_2−SiO_2 Microhoneycombs Synthesized from Inexpensive Precursors as Monolithic Photocatalyst Systems **27**

2.1 Introduction ⋯ 27

2.2 Materials and Methods ⋯ 28

2.2.1 Chemicals ⋯ 28

2.2.2 Synthesis of TiO_2−SiO_2 Microhoneycombs ⋯ 29

2.2.3 Characterization ⋯ 30

2.2.4 Photocatalytic Activity Measurement ⋯ 31

2.3 Results and Discussion ⋯ 32

2.3.1 Synthesis of TiO_2−SiO_2 Microhoneycombs ⋯ 32

2.3.2 Calcination of Microhoneycombs ⋯ 33

2.3.3 Hydraulic Resistance ⋯ 35

2.3.4 Photocatalytic Activity in a Batch System ⋯ 35

2.3.5 Photocatalytic Activity in a Continuous Flow System ⋯ 37
2.4 Conclusions ⋯ 38
References ⋯ 39
Chapter 3 Improvement of Synthesis Method of TiO_2−SiO_2 Microhoneycombs 43
3.1 Introduction ⋯ 43
3.2 Materials and Methods ⋯ 44
3.2.1 Chemicals ⋯ 44
3.2.2 Synthesis of TiO_2−SiO_2 Microhoneycombs ⋯ 44
3.2.3 Characterization ⋯ 45
3.2.4 Photocatalytic Activity Measurement ⋯ 46
3.3 Results and Discussion ⋯ 48
3.3.1 Synthesis of TiO_2−SiO_2 Microhoneycombs ⋯ 48
3.3.2 Hydraulic Resistance ⋯ 53
3.3.3 Adsorption and Decolorization of MB ⋯ 54
3.4 Conclusions ⋯ 58
References ⋯ 58

Part 2 Continuous Adsorption of Phenol in Wastewater using Carbon Gel Monoliths with Introduced Straight Microchannels Synthesized by the Fiber Templating Method 61

Chapter 4 Development of Carbon Gel Monoliths with Introduced Straight Microchannels by the Fiber Templating Method 63
4.1 Introduction ⋯ 63
4.2 Materials and Methods ⋯ 65
4.2.1 Chemicals ⋯ 65
4.2.2 Synthesis of FCGMs ⋯ 65
4.2.3 Characterization ⋯ 66
4.2.4 Phenol Adsorption ⋯ 66
4.3 Results and Discussion ⋯ 68
4.3.1 Synthesis of FCGMs ⋯ 68
4.3.2 Hydraulic Resistance ⋯ 71

4.3.3 Activation of FCGMs ⋯ 71
4.3.4 Adsorption of Phenol ⋯ 73
4.4 Conclusions ⋯ 79
References ⋯ 79
Chapter 5 Determination of Optimal Dimensions of Fiber Templated Carbon Gel Monoliths (FCGMs) via Breakthrough Curve Simulation 85
5.1 Introduction ⋯ 85
5.2 Theory ⋯ 85
5.2.1 Simulation of Breakthrough Curves ⋯ 85
5.2.2 Resistances in Mass Transfer and Diffusion Time ⋯ 87
5.2.3 Critical Void Fraction ⋯ 89
5.2.4 Pressure Drop ⋯ 89
5.3 Experimental Section ⋯ 89
5.4 Results and Discussion ⋯ 90
5.4.1 Simulation of Breakthrough Curves ⋯ 90
5.4.2 Pressure Drop ⋯ 94
5.4.3 Comparison with a Packed Bed of Particles ⋯ 95
5.5 Conclusions ⋯ 97
References ⋯ 98
Chapter 6 Conclusions 99
Research Achievements 103
Acknowledgements 105

Chapter 1

General Introduction

Treatment of soluble aromatics, such as phenolic compounds and dyes, in industrial wastewater are essential due to their toxicity and environmental impacts. Although many treatment techniques are proposed and used, there are many limitations that should be improved to achieve more effective treatment. This work focused on improvement of mass transfer in wastewater treatment, using monoliths with introduced straight microchannels. In this chapter, the treatment techniques and limitations, the configurations of the treatment systems, and the importance of this work, are introduced.

1.1 Impacts of Soluble Aromatics

Phenol and its derivatives are frequently found in wastewater effluents from many industries, such as refineries, petrochemical production, plastics factories, pharmaceuticals, and paper industries.[1–5] Phenol is also an intermediate compound formed during the oxidation of larger aromatic hydrocarbons.[6] Phenol dissolved in drinking water causes a bad taste, even at a low concentration of 0.5 ppm.[1,3] Moreover, phenol is toxic to fish as well as human. Phenol could be readily adsorbed through human skin and causes skin and eye burn, as well as damages to circular systems.[1] The lethal dose of phenol is 50–500 mg kg^{-1} for human[7] while the lethal concentration is 5–25 ppm for fish.[3] Because of its toxicity, many governments and agencies worldwide impose strict standards and regulations for concentration of phenol in water (as low as 15 ppm for plastic production industries in the US,[8] up to 0.3 ppm in the EU,[9] 5 ppm in Japan)[10].

It has been estimated that 1–20% of the dyes produced are lost during the dyeing process and released to wastewater effluents.[11,12] The dyes used in industries have deep color. Human eye could detect the color of these dyes at as low as 0.005 ppm in a clear river, especially at red and reddish-purple hues.[13] Therefore, only a small amount of dyes would cause serious aesthetic problems. Water contaminated with dyes would be rendered unsuitable for human consumption, and the complaints are usually made by the general public.[14] The ability of the dyes to absorb lights would affect the photosynthesis of aquatic plants due to decreased light transmission.[15] Moreover, the aromatic rings and the heavy metals contained in the structure of the dyes are toxic not only to the aquatic life but also to humans.[15] Many dyes used in industries are synthesized by humans. These anthropogenic compounds are developed to be

high in stability (fastness) and therefore difficult to be biologically treated.[16] In fact, it was reported that some of the dyes could leave the treatment process barely treated.[15]

1.2 Treatment Techniques

Treatment techniques of soluble aromatics are summarized in Table 1.1 for phenols and Table 1.2 for dyes. Among these techniques, adsorption is widely used for the treatment of many recalcitrant pollutants which biological treatments are ineffective, while photocatalysis is a promising way to nonselectively degrade the pollutants at mild conditions. These two techniques are selected for the study in this work, and are discussed in the next subsections.

Table 1.1 Selected treatment techniques for phenol in wastewater (summarized from Ref. [1–4,17,18])

Technique	**Initial concentration / ppm**	**Advantages**	**Disadvantages**
Distillation	~3000	Nondestructive, complete separation possible	Expensive, energy demanding
Liquid-liquid extraction	20–6000	Nondestructive	Expensive
Adsorption	300–4000	High capacity, low operation cost	Secondary pollution/regeneration required, adsorbents not efficiently used, commercial activated carbons are expensive
Membrane pervaporation	up to 10000	Nondestructive	Vacuum required
Membrane-based solvent extraction	> 5000	Nondestructive, compact	Regeneration required
Emulsion liquid membrane	300–3000	High contact area	May not be stable against fluid shear

Table 1.1 Selected treatment techniques for phenol in wastewater (continued)

Technique	**Initial concentration / ppm**	**Advantages**	**Disadvantages**
Wet air oxidation (noncatalytic)	~3000	Can handle toxic wastewater not suitable for biological treatment, minimal air pollution discharge	High temperature & pressure, cannot fully mineralize phenol
Catalytic wet air oxidation	~3000	Milder conditions than noncatalytic counterpart	Expensive, catalyst leaching
Ozonation	~50	Fast kinetics	High generation cost, low solubility
Chemical/electrochemical oxidation	~50	Complete mineralization possible	Secondary pollution (metal ions)
Photocatalytic oxidation	~50	Inexpensive, nontoxic catalyst	Currently not working under visible light
Biodegradation	< 50	Inexpensive, complete mineralization possible	Limited to low concentration of phenol, slow

Table 1.2 Selected treatment techniques for dyes in wastewater (summarized from Ref. [11,15,19,20])

Technique	Advantages	Disadvantages
Adsorption by activated carbon (AC)	Good removal for various types of dyes	Commercial ACs are expensive
Membrane filtration	Applicable for all types of dyes	Production of concentrated sludge
Ion exchange	No adsorbent loss (by regeneration)	Not applicable for some dyes
Irradiation	Effective (lab scale)	Require a large amount of dissolved O_2
Electrokinetic coagulation	Economically feasible	High sludge production
Oxidative process	Simplicity of application	H_2O_2 agent needs to be activated
Fenton's reagent	Effective decolorization	Sludge production
Ozonation	Sludge volume not increased (applied in gaseous state)	Short half-life (~ 20 min)
Photochemical process	No sludge production, odor reduced	Formation of by-products
Sodium hypochlorite	Acceleration of azo bond cleavage	Release of aromatic amines
Electrochemical destruction	No consumption of chemicals, no sludge buildup, nontoxic intermediates	High electricity cost
White-rot fungi (enzymes)	High capacity	Unreliable enzyme production

Table 1.2 Selected treatment techniques for dyes in wastewater (continued)

Technique	Advantages	Disadvantages
Other microbial cultures	Decolorized in ~ 30 h	Not effective for azo dyes under aerobic conditions
Adsorption by microbial biomass	High affinity for certain dye-microorganism pairs	Not applicable for some dyes
Anaerobic bioremediation	Effective for azo & other water soluble dyes	Production of H_2S

1.2.1 Adsorption

Adsorption is the process where accumulation of a substance at the interface of two phases occurs. The substance that accumulates is called an "adsorbate", while the solid phase where accumulation occurs is called an "adsorbent".[16,21] Adsorption can be classified as chemical adsorption (chemisorption) and physical adsorption (physisorption).[15,22] Chemical adsorption occurs when a strong chemical bond is formed between the adsorbate and the surface of the adsorbent. It is limited to one layer, and is usually irreversible. On the other hand, physical adsorption occurs by weaker van der Waals forces, so multilayer adsorption is permitted, and the process is generally reversible. Commercial adsorbents which have sufficient adsorption capacity generally have high specific surface area, usually over 300 m^2 g^{-1}. Such adsorbents usually contain micropores and large porosity (void fraction of 30–85 vol%).

Among commercial adsorbents, activated carbons (ACs) are the most commonly used in water treatment, due to their ability to adsorb many pollutants, including recalcitrant and toxic compound that cannot be treated biologically.[21] Commercially available ACs are usually derived from natural sources, such as coconut shells, coal, and wood/sawdust. They contain well-defined micropores and a high specific surface area of 600–2000 m^2 g^{-1}.[23] Common types of activated carbons are granular activated carbons (GACs) and powdered activated carbons (PACs). GACs is larger in size and are usually regenerated after use. However, the large granular size results in slow mass transfer, and the GACs are not effectively used. On the other hand, PACs are smaller in size and shorter contact times than GACs can be used. However, PACs are usually mixed with the fluid to be treated in the form of a slurry, and are usually

separated and discarded after use.[20] In addition, since the cost of activated carbon is generally high, many research groups reported the use of alternative low cost adsorbents, such as agricultural wastes, to replace the use of commercial ACs.[20,24–26] Adsorption technique can also be thought as merely concentrating the pollutant without actually degrading them to benign substances.

1.2.2 Photocatalysis as Advanced Oxidation Process

To degrade recalcitrant pollutant to benign substances, such as water and carbon dioxide, advanced oxidation processes (AOPs) have been suggested for wastewater treatment. These processes are characterized by *in situ* generation of hydroxyl radicals. Such generated hydroxyl radicals are strong oxidizing agents and can be used to nonselectively degrade organic substances, including those difficult to degrade by biological means.[27–29] The examples of AOPs are those using ozone and hydrogen peroxide, (photo-)Fenton and similar reactions, and photocatalysis.[16,30] Among these processes, photocatalysis using solid semiconductors are widely studied for wastewater treatment.

The use of semiconductors as photocatalysts was first reported by Honda and Fujishima for water splitting.[31] The first report for the application of semiconductor photocatalysts for remediation of pollutants in water is by Frank and Bard, for the reduction of CN^-.[32,33] Semiconductor photocatalysts generate reactive radicals from the photoexcitation of electrons in the filled valence band to the vacant conduction band, separated by the band gap (Fig. 1.1). This process require the energy of the photon to be at least equal to the band gap energy. The excited electron in the conduction band and the positive hole formed in the valence band then react with adsorbed species in subsequent redox reactions. The reactive hydroxyl radical usually mentioned in AOPs is formed by the reaction between the positive hole and adsorbed water, which could react with organic pollutants and degrade them. Here, the term “catalysis” is included to specify accelerated photoreaction by the presence of semiconductors, and not imply that light is the catalyst which remains unconsumed after the reaction.[34]

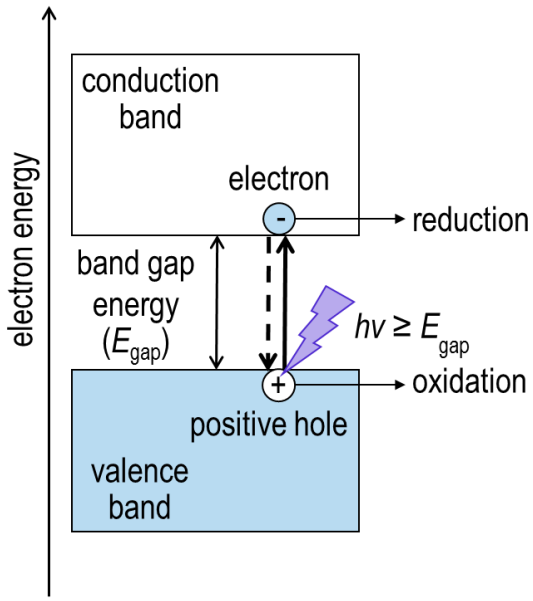

Fig. 1.1 Schematic drawing of the mechanism of semiconductor photocatalysts.

Since the pioneer works, many researches about the use of semiconductors as photocatalysts for wastewater treatment were reported. Similar to other AOPs, the degradation reaction of pollutants is nonselective, and can be written in a general form as Eq. 1.1:[35]

$$\text{pollutant} + O_2 \xrightarrow[h\nu \geq E_{gap}]{\text{semiconductor}} CO_2 + H_2O + \text{mineral acids} \qquad (1.1)$$

Among the semiconductors, titanium dioxide is the most widely studied due to its high photocatalytic activity, stability, nontoxicity, and availability.[34,36,37] P25, the most common commercial photocatalyst usually used as a standard in comparing the photocatalytic activity, is a mixture of TiO_2 in its anatase and rutile form at approximately 8:2 ratio.[38] The major drawback of TiO_2 as a photocatalyst is its large band gap (3.2 eV for anatase, 3.0 eV for rutile), so only the light in ultraviolet (UV) region could be used for unmodified TiO_2, making it ineffective to use in solar light.[39] Since TiO_2 gains superhydrophilicity under light irradiation, the adsorption capacity of organic pollutants, especially hydrophobic molecules, is generally low as well.[28,40]

1.3 Configurations of Treatment Systems

GACs used in water purification are generally used as a fixed bed. The size of GACs are in the range of 1.2 to 1.6 mm.[41] This granular size is selected to minimize the pressure drop caused by fluid flow.[22] However, as mentioned in Section 1.2.1, the GACs commonly used in adsorption of pollutants suffers from mass transfer limitations due to their large granular size.

Although the mass transport rate could be increased by decreasing the granular (particle) size, the pressure drop would increase. The trade-off relationship which is inherent for the use of particles as a packed column makes it difficult to design a process in which both rapid mass transport and low pressure drop could be realized together.

The configurations of photocatalytic systems for wastewater treatment can be generally divided into two main types: suspended systems and immobilized systems. In suspended systems, photocatalyst particles are directly mixed with wastewater in the form of slurry. Although this configuration could ensure adequate mass transfer due to the mixing between the photocatalyst and the fluid to be treated, subsequent separation to recover the photocatalyst particles is necessary. The cost of the separation step is expensive and the system is difficult to scale up. Immobilization of photocatalysts by coating or inclusion in supports could eliminate the separation step. However, the contact surface area between the photocatalyst and the fluid is generally reduced, so the systems are limited by mass transfer.

To overcome the mass transfer limitations mentioned earlier, many system configurations are suggested, such as modified slurry systems, monolithic honeycombs, and microreactors. Two of the configurations, monolithic honeycombs and microreactors, are explained in the next subsections.

1.3.1 Monolithic Honeycombs

Monolithic honeycombs consist of straight, parallel channels with various opening shapes, such as squares, rectangles or triangles. The size of these opening are generally in the millimeter range. Because of the straight channels, monolithic honeycombs would cause lower hydraulic resistance than beds packed with particles. The monoliths are used especially in applications in which hydraulic resistance should be kept minimal, such as three-way catalytic converters in automobiles and other air pollution control devices in general.[42–44]

The use of monolithic honeycombs are also suggested for applications in continuous adsorption of pollutants, both in gas phase and liquid phase.[45–47] The low hydraulic resistance of these monoliths would allow high flow rates of the wastewater to be treated.

Monoliths were also studied, both in catalysis (without light irradiation)[48] and in photocatalysis (Fig. 1.2).[37,49] Monoliths could be used to reduce the pressure drop and increase the interfacial surface area at the same time, and also to facilitate the scale up of the process. However, the study of light irradiation inside the monolith revealed that the light was attenuated along the

length of the monolith due to shadowing effect of the opaque walls.[50] It was also found that the light intensity would drop to only 1% of the value at the monolith entrance at the axial position three times of the opening size, regardless of the opening shape (Fig. 1.3).[50,51]

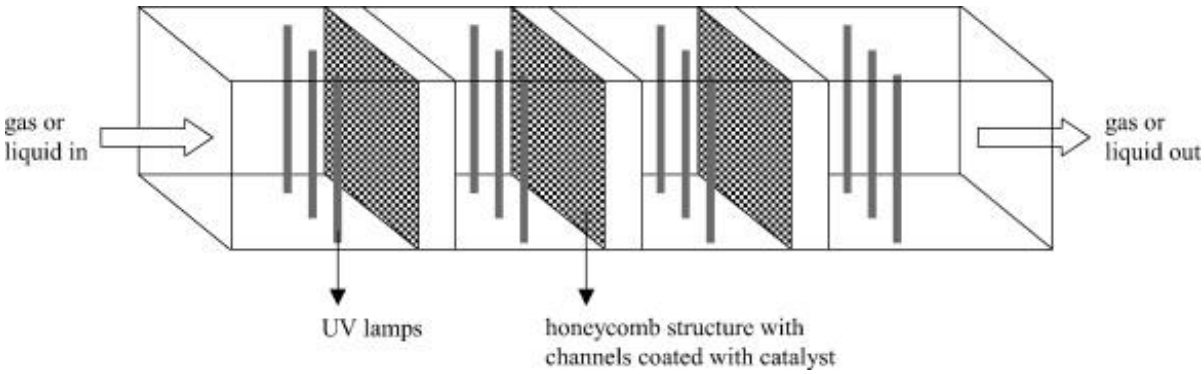

Fig. 1.2 Monolithic honeycomb photoreactor with multiple light sources (reprinted from Ref. 37 with permission from Elsevier)

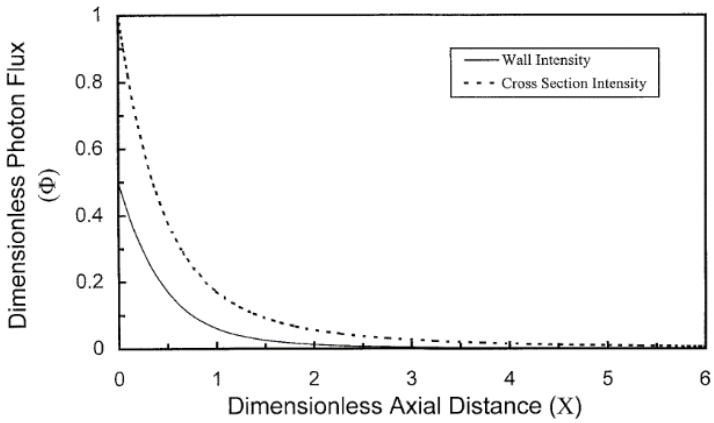

Fig. 1.3 Light intensity profile inside the monolith with circular channels and non-reflective walls. Φ: the ratio between the intensity of light at a given position to that at the entrance, X: ratio between the axial distance from the entrance and channel diameter. (reprinted from Ref. 50 with permission from Elsevier)

1.3.2 Microreactors and Microdevices

Microreactors, a miniaturized version of conventional reactors, have small dimensions in which at least one dimension does not exceed 1 mm.[52] Because of their small dimensions, the surface area per volume is usually at least one order of magnitude higher than those of conventional reactors.[53] As a result, mass and energy transport rates are high, and reaction conditions can be

more precisely controlled.[52,54] The use of microreactors are also suggested for photocatalysis, as efficient irradiation could be achieved in such reactors (Fig. 1.4).[37,54–57]

For applications of small tubes related to adsorption, capillary columns in which the inner diameter is up to 100 μm, are frequently used in chromatography.[58–60] These smaller columns could produce sharper peaks than larger columns at the same amount of injected analyte. Research about the use of microfluidic devices is also very popular in the biochemical field, and microdevices for batch adsorption of biomolecules, such as proteins, have been reported.[61] However, because these microdevices rely on their small dimensions, the only way to increase the volume of the fluid to be treated is by increasing the number of the devices, which is typically expensive.

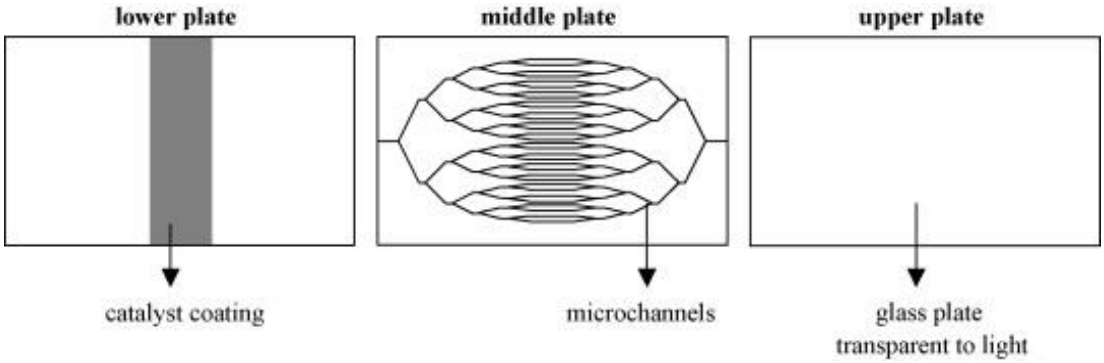

Fig. 1.4 An example of photocatalytic microreactors (reprinted from Ref. 37 with permission from Elsevier)

1.4 Microhoneycombs

1.4.1 Ice Templating Method

The use of ice crystals to mold materials into a desirable morphology was firstly reported by Mahler and Bechtold for SiO_2 polygonal fibers,[62,63] by slowly dipping hydrogels into a cold bath in one direction at a constant speed. During this "unidirectional freezing" step, the water content in the hydrogels would separate and ice crystals would form in one direction, which could be used to mold the gels into their final morphology.

Later, Mukai and coworkers reported that the ice templating method could be used to synthesize materials having morphologies other than polygonal fibers, such as lamella, flat fibers, and microhoneycombs (Fig. 1.5).[64,65] The final morphology was found to depend on the firmness of the gels before unidirectional freezing (Fig. 1.6).[66] Softer gels would give lamella morphology (Fig. 1.7), moderately firm gels would give microhoneycombs (Fig. 1.8), and firm

gels would give polygonal fibers (like those reported by Mahler and Bechtold, Fig. 1.9) or powders. The microhoneycomb morphology was selected among the possible morphologies obtained because it resembles larger honeycombs, so the reduction of hydraulic resistance when used under fluid flow was expected. Walls of the synthesized microhoneycombs were also thin, in the micrometer order. These thin walls are also expected to facilitate mass transfer as well.

Although the ice templating method was originally developed from SiO_2 systems, it can also be applied to other inorganic gels, such as Al_2O_3,[67,68] ZrO_2,[69] TiO_2,[70,71] and the mixture of these gels,[72,73] as well as organic (carbon) gels,[74,75] polymers,[76] carbon nanotubes,[77] and ion-exchange resins.[78]

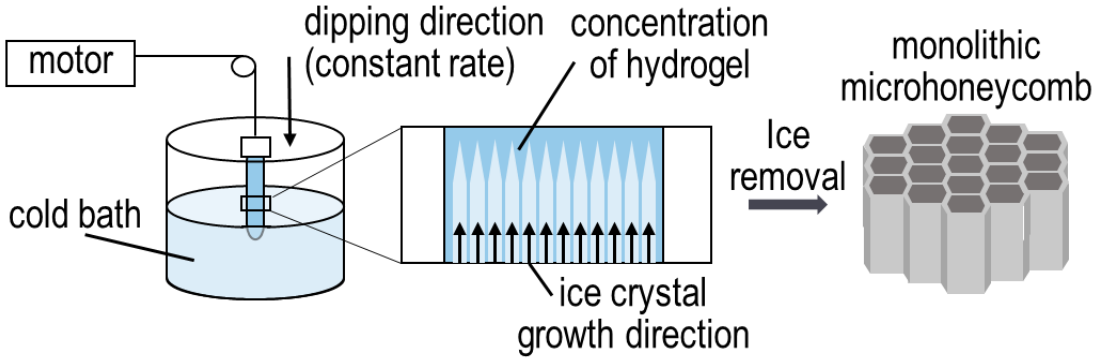

Fig. 1.5 The ice templating method for the synthesis of microhoneycombs

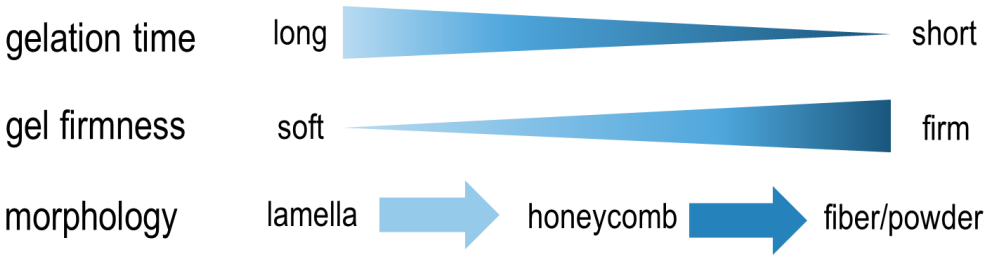

Fig. 1.6 Effect of gelation time to the final morphology in ice templating method

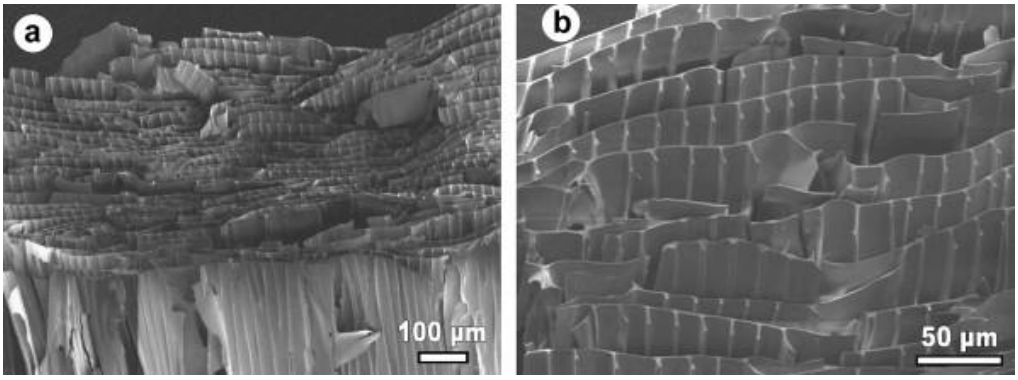

Fig. 1.7 SEM image of SiO_2 gel having lamella morphology obtained from ice templating of silica sol before gelation, showing (a) overall image and (b) enlarged image (reprinted from Ref. 66 with permission from Elsevier)

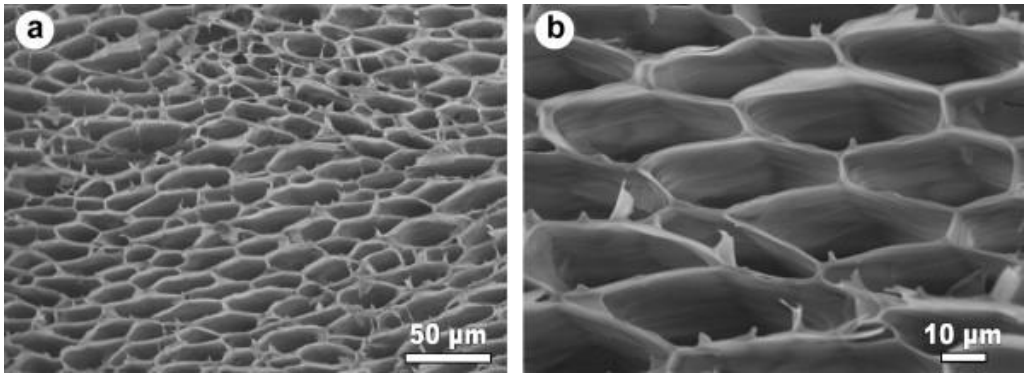

Fig. 1.8 Cross-sectional SEM image of a SiO_2 microhoneycomb, showing (a) overall image and (b) enlarged image (reprinted from Ref. 66 with permission from Elsevier)

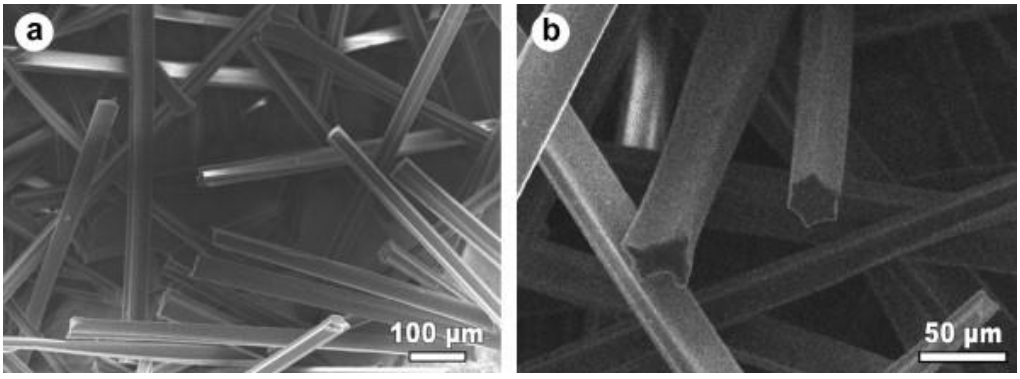

Fig. 1.9 SEM image of SiO_2 polygonal fibers synthesized by ice templating of firm silica hydrogel, showing (a) overall image and (b) enlarged image (reprinted from Ref. 66 with permission from Elsevier).

1.4.2 Applications of Microhoneycombs

As mentioned in the previous subsection, the ice templating method can be applied to a variety of hydrogels. Therefore, synthesized materials with microhoneycomb morphology can be used in many applications which both rapid mass transfer and low hydraulic resistance are preferred. There are reports about using microhoneycombs synthesized by ice templating method as sorbents,[79,80] ion-exchange resins,[78] as well as solid catalysts.[81–83] Yoshida et al. reported the use of carbon microhoneycombs synthesized from resorcinol-formaldehyde (RF) gels for continuous phenol adsorption.[79] It was found that the thin walls of the microhoneycombs could facilitate mass transfer, and high utilization of the monoliths could be achieved even for monoliths as short as 15 mm. For photocatalytic applications, Nishihara et al. reported the synthesis of TiO_2−SiO_2 microhoneycombs from alkoxide precursors.[73] The binary sol system was selected to facilitate morphology control, as well as to obtain samples with high specific surface area (more than 500 $m^2\ g^{-1}$) which is difficult to achieve for pure TiO_2. The high surface area of the monoliths could facilitate both mass and radiative transport, and the photocatalytic activity in degradation of salad oil in batch systems of the microhoneycombs were higher than P25 powder frequently used as a reference.

Although there are many reports regarding the applications of microhoneycombs, there are still inadequate reports about the use of such monoliths in continuous treatment of water soluble aromatics. The previously reported photocatalytic work contains only the applications in batch systems, possibly because it is difficult to synthesize the monoliths having sufficiently large diameter to be evaluated in continuous flow systems, in which flow velocity control is difficult for samples with small cross-sectional area. Furthermore, the effect of monolith dimensions (channel size and wall thickness) has not been reported. Possibly because it is difficult to independently control the channel size and wall thickness in the ice templating method (Fig. 1.10).[84] Such investigations are crucial to study the use of the monoliths in continuous treatment of soluble aromatics in wastewater.

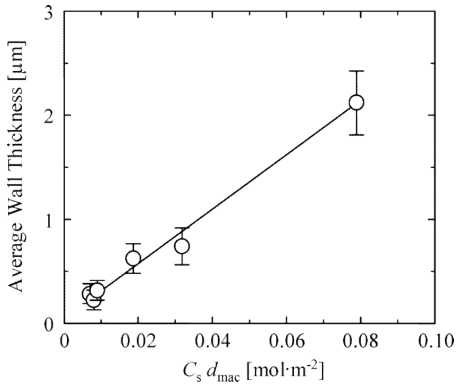

Fig. 1.10 Relationship between the wall thickness and the product between C_s (concentration of SiO_2) and d_{mac} (channel size) of SiO_2 microhoneycombs. Note that C_s is generally kept constant at 1.9 mol L^{-1} in later work. Reprinted with permission from Ref. 84. Copyright (2005) American Chemical Society

1.5 Research Objectives

In Section 1.1 and 1.2, the necessity and the techniques to treat soluble aromatics in wastewater were discussed. Among those techniques, adsorption and heterogeneous photocatalysis, were introduced in detail. It was found that the problem to further improve the efficiency of both techniques is that the systems, using immobilized solid phase, are generally limited by mass transfer. To overcome such mass transfer limitations, the use of monolithic honeycombs and microdevices was suggested, as introduced in Section 1.3. Microhoneycombs synthesized by the ice templating method (Section 1.4) are thought to be a combination between larger monolithic honeycombs and numbered-up microdevices, due to the combination their straight microchannels and thin walls. This unique morphology could also allow the compatibility between rapid mass transfer and low hydraulic resistance. The synthesized monoliths also possess high specific surface area, which is desirable for heterogeneous processes. Therefore, the applications of such monoliths in the treatment of soluble aromatics in wastewater is thought to be able to increase the process efficiency.

In Part 1 (Chapter 2 and 3), gels consisting with TiO_2 and SiO_2 were molded into a microhoneycomb morphology, and the application of them in photocatalytic treatment of soluble aromatics in wastewater, was studied. There is a previous work reported by Nishihara et al. about the synthesis and applications of such TiO_2−SiO_2 microhoneycombs in photocatalysis.[73] However, the microhoneycombs were synthesized by alkoxide precursors, which are generally very reactive, therefore it is difficult to adjust synthesis conditions. The applications introduced in the previous work was also limited to batch systems, so the potential

of the microhoneycombs to minimize the pressure drop caused by a fluid flow has not been demonstrated in this case.

In Chapter 2, a synthesis method of TiO_2−SiO_2 microhoneycombs from sodium silicate solution was developed. A sodium silicate solution is a general precursor for silica gel production,[85,86] and it is cheaper than its alkoxide counterpart. Commercial TiO_2 sol was used as a source of TiO_2. The applications of such monoliths in photocatalysis, both in batch and continuous flow systems, were studied. Finally, the effect of calcination temperature to specific surface area and the photocatalytic activity were investigated.

In Chapter 3, the synthesis method of TiO_2−SiO_2 microhoneycombs from sodium silicate solution was improved, by using two sources of commercial TiO_2 sols stabilized at different pH. As mentioned in Section 1.4, the final morphology of the samples synthesized by the ice templating method can be controlled by adjusting the gel firmness before unidirectional freezing. In SiO_2 systems, this could be done by adjusting the pH of the sol before gelation.[87] Therefore, by adjusting the ratio between the two TiO_2 sols, the morphology of the samples could be adjusted independently from TiO_2 content. Similar to Chapter 2, the effect of calcination temperature to the photocatalytic activity was investigated. In addition, the effect of surface properties to the adsorption and reaction of the substrates were studied. Finally, the photocatalytic activity of the monolith synthesized by the improved method introduced in this chapter was compared with that of the monolith synthesized by the method described in Chapter 2, as well as that of the bed packed with crushed microhoneycombs, to study the effect of synthesis method and sample morphology.

The design guidelines for monolithic adsorbents reported in the literature stated that being able to tune the channel size and the wall thickness is crucial to obtain monoliths with optimal performance. It was also found that, when larger monolithic honeycombs are used in photocatalytic systems, the light intensity inside the monolith rapidly decreases along the length of the monolith due to wall shadowing. Therefore, it is also crucial to be able to adjust the channel size and wall thickness of the microhoneycombs. However, even though the ice templating method allows the adjustment of the channel size by either changing the dipping rate or the bath temperature, the wall thickness would also change with the channel size, so it is difficult to independently adjust the channel size and the wall thickness. Therefore, an alternative method to synthesize monoliths with straight microchannels is preferred. Such a method was developed and described in Part 2 (Chapter 4 and 5).

In Chapter 4, a new method to synthesize monolithic samples, the "fiber templating method" was developed. This method uses straight fibers with circular cross section as templates to introduce straight, parallel channels into the samples. Polyesters fibers used as templates could be removed by heating to a temperature above the decomposition temperature of the fibers, and the channel size and wall thickness could be independently adjusted by changing the size and the amount of the fibers, respectively. Carbon gels were selected as the material for the monolith due to its ability to tune the porosity,[88,89] and carbon gel monoliths were synthesized by this fiber templating method. In addition, to study the effect of channel size and wall thickness, the application of such monoliths in continuous adsorption of phenol was studied.

In Chapter 5, a method to find the optimal monolith dimensions (channel size and wall thickness) was developed based on mass transfer in the monoliths with different dimensions, similar to the method suggested for the larger monolithic adsorbents. The parameters related to mass transfer were obtained via breakthrough curve simulation, and the optimal channel size and wall thickness were determined. To verify the results, the behavior of the systems using the monoliths with different dimensions, and different flow rate, was predicted based on the previously determined mass transfer data. Finally, the breakthrough curve of the monolith with optimal dimensions was simulated and compared with the breakthrough curves of beds packed with particles, to illustrate the advantages in using the monolithic adsorbents.

Finally, in Chapter 6, the results and conclusions of the previous chapters are summarized, and the potential of the monoliths with introduced straight microchannels to be used in continuous treatment of wastewater is shown.

References

(1) Busca, G.; Berardinelli, S.; Resini, C.; Arrighi, L. Technologies for the Removal of Phenol from Fluid Streams: A Short Review of Recent Developments. *J. Hazard. Mater.* **2008**, *160* (2–3), 265.

(2) Mohammadi, S.; Kargari, A.; Sanaeepur, H.; Abbassian, K.; Najafi, A.; Mofarrah, E. Phenol Removal from Industrial Wastewaters: A Short Review. *Desalin. Water Treat.* **2015**, *53* (8), 2215.

(3) Jiang, H.; Fang, Y.; Fu, Y.; Guo, Q.-X. Studies on the Extraction of Phenol in Wastewater. *J. Hazard. Mater.* **2003**, *101* (2), 179.

(4) Kim, K.-H.; Ihm, S.-K. Heterogeneous Catalytic Wet Air Oxidation of Refractory

Organic Pollutants in Industrial Wastewaters: A Review. *J. Hazard. Mater.* **2011**, *186* (1), 16.

(5) Veeresh, G. S.; Kumar, P.; Mehrotra, I. Treatment of Phenol and Cresols in Upflow Anaerobic Sludge Blanket (UASB) Process: A Review. *Water Res.* **2005**, *39* (1), 154.

(6) Ding, Z.-Y.; Aki, S. N. V. K.; Abraham, M. A. Catalytic Supercritical Water Oxidation: Phenol Conversion and Product Selectivity. *Environ. Sci. Technol.* **1995**, *29* (11), 2748.

(7) National Library of Medicine (US). Hazardous substances data bank [Internet] https://toxnet.nlm.nih.gov/cgi-bin/sis/search2/r?dbs+hsdb:@term+@DOCNO+113 (accessed Sep 18, 2018).

(8) Code of Federal Regulations, Title 40, section 414.91, Toxic pollutant effluent limitations and standards for direct discharge point sources that use end-of-pipe biological treatment. https://www.govinfo.gov/app/details/CFR-2018-title40-vol31/CFR-2018-title40-vol31-sec414-91/summary (1993) (accessed Sep 19, 2018)

(9) The European Commission. establishing best available techniques (BAT) conclusions for waste treatment, under Directive 2010/75/EU of the European Parliament and of the Council https://eur-lex.europa.eu/eli/dec_impl/2018/1147/oj (accessed May 9, 2019).

(10) Government of Japan. Ministry of the Environment.: National Effluent Standards http://www.env.go.jp/en/water/wq/nes.html (accessed Sep 19, 2018).

(11) Forgacs, E.; Cserháti, T.; Oros, G. Removal of Synthetic Dyes from Wastewaters: A Review. *Environ. Int.* **2004**, *30* (7), 953.

(12) Akpan, U. G.; Hameed, B. H. Parameters Affecting the Photocatalytic Degradation of Dyes Using TiO_2-Based Photocatalysts: A Review. *J. Hazard. Mater.* **2009**, *170* (2–3), 520.

(13) Pierce, J. Colour in Textile Effluents-the Origins of the Problem. *J. Soc. Dye. Colour.* **1994**, *110* (4), 131.

(14) Kao, C. .; Chou, M. .; Fang, W. .; Liu, B. .; Huang, B. . Regulating Colored Textile Wastewater by 3/31 Wavelength Admi Methods in Taiwan. *Chemosphere* **2001**, *44* (5), 1055.

(15) Yagub, M. T.; Sen, T. K.; Afroze, S.; Ang, H. M. Dye and Its Removal from Aqueous Solution by Adsorption: A Review. *Adv. Colloid Interface Sci.* **2014**, *209*, 172.

(16) Davis, M. L.; Cornwell, D. A. *Introduction to Environmental Engineering*, 5th ed.; McGraw-Hill Education (Asia): Singapore, 2013.

(17) Otero, M.; Zabkova, M.; Rodrigues, A. E. Adsorptive Purification of Phenol Wastewaters: Experimental Basis and Operation of a Parametric Pumping Unit. *Chem. Eng. J.* **2005**, *110* (1–3), 101.

(18) El-Naas, M. H.; Al-Muhtaseb, S. A.; Makhlouf, S. Biodegradation of Phenol by Pseudomonas Putida Immobilized in Polyvinyl Alcohol (PVA) Gel. *J. Hazard. Mater.* **2009**, *164* (2–3), 720.

(19) Robinson, T.; McMullan, G.; Marchant, R.; Nigam, P. Remediation of Dyes in Textile Effluent: A Critical Review on Current Treatment Technologies with a Proposed Alternative. *Bioresour. Technol.* **2001**, *77* (3), 247.

(20) Salleh, M. A. M.; Mahmoud, D. K.; Karim, W. A. W. A.; Idris, A. Cationic and Anionic Dye Adsorption by Agricultural Solid Wastes: A Comprehensive Review. *Desalination* **2011**, *280* (1–3), 1.

(21) Dąbrowski, A. Adsorption — from Theory to Practice. *Adv. Colloid Interface Sci.* **2001**, *93* (1–3), 135.

(22) Henley, E. J.; Seader, J. D.; Roper, D. K. *Separation Process Principles*, 3rd ed.; John Wiley & Sons (Asia): Hoboken, NJ, 2011.

(23) Streat, M.; Patrick, J. W.; Perez, M. J. C. Sorption of Phenol and Para-Chlorophenol from Water Using Conventional and Novel Activated Carbons. *Water Res.* **1995**, *29* (2), 467.

(24) Crini, G. Non-Conventional Low-Cost Adsorbents for Dye Removal: A Review. *Bioresour. Technol.* **2006**, *97* (9), 1061.

(25) Rengaraj, S.; Moon, S.-H.; Sivabalan, R.; Arabindoo, B.; Murugesan, V. Agricultural Solid Waste for the Removal of Organics: Adsorption of Phenol from Water and Wastewater by Palm Seed Coat Activated Carbon. *Waste Manag.* **2002**, *22* (5), 543.

(26) Srivastava, V. C.; Swamy, M. M.; Mall, I. D.; Prasad, B.; Mishra, I. M. Adsorptive

Removal of Phenol by Bagasse Fly Ash and Activated Carbon: Equilibrium, Kinetics and Thermodynamics. *Colloids Surfaces A Physicochem. Eng. Asp.* **2006**, *272* (1–2), 89.

(27) Mukherjee, P. S.; Ray, A. K. Major Challenges in the Design of a Large-Scale Photocatalytic Reactor for Water Treatment. *Chem. Eng. Technol.* **1999**, *22* (3), 253.

(28) Dong, H.; Zeng, G.; Tang, L.; Fan, C.; Zhang, C.; He, X.; He, Y. An Overview on Limitations of TiO_2-Based Particles for Photocatalytic Degradation of Organic Pollutants and the Corresponding Countermeasures. *Water Res.* **2015**, *79*, 128.

(29) Gmurek, M.; Olak-Kucharczyk, M.; Ledakowicz, S. Photochemical Decomposition of Endocrine Disrupting Compounds – A Review. *Chem. Eng. J.* **2017**, *310*, 437.

(30) Malato, S.; Fernández-Ibáñez, P.; Maldonado, M. I.; Blanco, J.; Gernjak, W. Decontamination and Disinfection of Water by Solar Photocatalysis: Recent Overview and Trends. *Catal. Today* **2009**, *147* (1), 1.

(31) Fujishima, A.; Honda, K. Electrochemical Photolysis of Water at a Semiconductor Electrode. *Nature* **1972**, *238* (5358), 37.

(32) Frank, S. N.; Bard, A. J. Heterogeneous Photocatalytic Oxidation of Cyanide and Sulfite in Aqueous Solutions at Semiconductor Powders. *J. Phys. Chem.* **1977**, *81* (15), 1484.

(33) Frank, S. N.; Bard, A. J. Heterogeneous Photocatalytic Oxidation of Cyanide Ion in Aqueous Solutions at TiO_2 Powder. *J. Am. Chem. Soc.* **1977**, *99* (1), 303.

(34) Mills, A.; Le Hunte, S. An Overview of Semiconductor Photocatalysis. *J. Photochem. Photobiol. A Chem.* **1997**, *108* (1), 1.

(35) Mills, A.; Davies, R. H.; Worsley, D. Water Purification by Semiconductor Photocatalysis. *Chem. Soc. Rev.* **1993**, *22* (6), 417.

(36) McCullagh, C.; Skillen, N.; Adams, M.; Robertson, P. K. J. Photocatalytic Reactors for Environmental Remediation: A Review. *J. Chem. Technol. Biotechnol.* **2011**, *86* (8), 1002.

(37) Van Gerven, T.; Mul, G.; Moulijn, J.; Stankiewicz, A. A Review of Intensification of Photocatalytic Processes. *Chem. Eng. Process. Process Intensif.* **2007**, *46* (9), 781.

(38) Ohtani, B.; Prieto-Mahaney, O. O.; Li, D.; Abe, R. What Is Degussa (Evonik) P25? Crystalline Composition Analysis, Reconstruction from Isolated Pure Particles and Photocatalytic Activity Test. *J. Photochem. Photobiol. A Chem.* **2010**, *216* (2–3), 179.

(39) Cataldo, S.; Weckhuysen, B. M.; Pettignano, A.; Pignataro, B. Multi-Doped Brookite-Prevalent TiO_2 Photocatalyst with Enhanced Activity in the Visible Light. *Catal. Letters* **2018**, *148* (8), 2459.

(40) Wang, R.; Hashimoto, K.; Fujishima, A.; Chikuni, M.; Kojima, E.; Kitamura, A.; Shimohigoshi, M.; Watanabe, T. Light-Induced Amphiphilic Surfaces. *Nature* **1997**, *388* (6641), 431.

(41) United States Environmental Protection Agency. Granular Activated Carbon https://iaspub.epa.gov/tdb/pages/treatment/treatmentOverview.do?treatmentProcessId=2074826383 (accessed May 19, 2019).

(42) de Nevers, N. *Air Pollution Control Engineering*, 2nd ed.; McGraw-Hill Education (Asia): Singapore, 2000.

(43) Farrauto, R. J.; Heck, R. M. Catalytic Converters: State of the Art and Perspectives. *Catal. Today* **1999**, *51* (3–4), 351.

(44) Roy, S.; Bauer, T.; Al-Dahhan, M.; Lehner, P.; Turek, T. Monoliths as Multiphase Reactors: A Review. *AIChE J.* **2004**, *50* (11), 2918.

(45) Gadkaree, K. P. Carbon Honeycomb Structures for Adsorption Applications. *Carbon N. Y.* **1998**, *36* (7–8), 981.

(46) Grande, C. A.; Cavenati, S.; Barcia, P.; Hammer, J.; Fritz, H. G.; Rodrigues, A. E. Adsorption of Propane and Propylene in Zeolite 4A Honeycomb Monolith. *Chem. Eng. Sci.* **2006**, *61* (10), 3053.

(47) Hosseini, S.; Khan, M. A.; Malekbala, M. R.; Cheah, W.; Choong, T. S. Y. Carbon Coated Monolith, a Mesoporous Material for the Removal of Methyl Orange from Aqueous Phase: Adsorption and Desorption Studies. *Chem. Eng. J.* **2011**, *171* (3), 1124.

(48) Beretta, A.; Orsenigo, C.; Ferlazzo, N.; Tronconi, E.; Forzatti, P.; Berti, F. Analysis of the Performance of Plate-Type Monolithic Catalysts for Selective Catalytic Reduction $DeNO_x$ Applications. *Ind. Eng. Chem. Res.* **1998**, *37* (7), 2623.

(49) Sauer, M. L.; Ollis, D. F. Acetone Oxidation in a Photocatalytic Monolith Reactor. *Journal of Catalysis*. **1994**, *149* (1), 81.

(50) Hossain, M. M.; Raupp, G. B. Radiation Field Modeling in a Photocatalytic Monolith Reactor. *Chem. Eng. Sci.* **1998**, *53* (22), 3771.

(51) Alexiadis, A. 2-D Radiation Field in Photocatalytic Channels of Square, Rectangular, Equilateral Triangular and Isosceles Triangular Sections. *Chem. Eng. Sci.* **2006**, *61* (2), 516.

(52) Tanimu, A.; Jaenicke, S.; Alhooshani, K. Heterogeneous Catalysis in Continuous Flow Microreactors: A Review of Methods and Applications. *Chem. Eng. J.* **2017**, *327*, 792.

(53) Kiwi-Minsker, L.; Renken, A. Microstructured Reactors for Catalytic Reactions. *Catal. Today* **2005**, *110* (1–2), 2.

(54) Visan, A.; Rafieian, D.; Ogieglo, W.; Lammertink, R. G. H. Modeling Intrinsic Kinetics in Immobilized Photocatalytic Microreactors. *Appl. Catal. B Environ.* **2014**, *150–151*, 93.

(55) Heggo, D.; Ookawara, S. Multiphase Photocatalytic Microreactors. *Chem. Eng. Sci.* **2017**, *169*, 67.

(56) Lindstrom, H.; Wootton, R.; Iles, A. High Surface Area Titania Photocatalytic Microfluidic Reactors. *AIChE J.* **2007**, *53* (3), 695.

(57) Gorges, R.; Meyer, S.; Kreisel, G. Photocatalysis in Microreactors. *J. Photochem. Photobiol. A Chem.* **2004**, *167* (2–3), 95.

(58) Randon, J.; Guerrin, J.-F.; Rocca, J.-L. Synthesis of Titania Monoliths for Chromatographic Separations. *J. Chromatogr. A* **2008**, *1214* (1–2), 183.

(59) Mistry, K.; Krull, I.; Grinberg, N. Capillary Electrochromatography: An Alternative to HPLC and CE. *J. Sep. Sci.* **2002**, *25* (15–17), 935.

(60) Gusev, I.; Huang, X.; Horváth, C. Capillary Columns with in Situ Formed Porous Monolithic Packing for Micro High-Performance Liquid Chromatography and Capillary Electrochromatography. *J. Chromatogr. A* **1999**, *855* (1), 273.

(61) Rho, H. S.; Hanke, A. T.; Ottens, M.; Gardeniers, H. A Microfluidic Device for the Batch Adsorption of a Protein on Adsorbent Particles. *Analyst* **2017**, *142* (19), 3656.

(62) Mahler, W.; Bechtold, M. F. Freeze-Formed Silica Fibres. *Nature* **1980**, *285* (5759), 27.

(63) Mahler, W. Siliceous Fibers and Method of Preparing Them. U.S. Patent 4,122,041, 1978.

(64) Mukai, S. R.; Nishihara, H.; Tamon, H. Porous Properties of Silica Gels with Controlled Morphology Synthesized by Unidirectional Freeze-Gelation. *Microporous Mesoporous Mater.* **2003**, *63* (1–3), 43.

(65) Mukai, S. R.; Nishihara, H.; Tamon, H. Formation of Monolithic Silica Gel Microhoneycombs (SMHs) Using Pseudosteady State Growth of Microstructural Ice Crystals. *Chem. Commun.* **2004**, No. 7, 874.

(66) Mukai, S. R.; Nishihara, H.; Tamon, H. Morphology Maps of Ice-Templated Silica Gels Derived from Silica Hydrogels and Hydrosols. *Microporous Mesoporous Mater.* **2008**, *116* (1–3), 166.

(67) Maki, T.; Sakka, S. Preparation of Porous Alumina Fibres by Unidirectional Freezing of Gel. *J. Mater. Sci. Lett.* **1986**, *5* (1), 28.

(68) Maki, T.; Sakka, S. Formation of Alumina Fibers by Unidirectional Freezing of Gel. *J. Non. Cryst. Solids* **1986**, *82* (1–3), 239.

(69) Kokubo, T.; Teranishi, Y.; Maki, T. Preparation of Amorphous ZrO_2 Fibers by Unidirectional Freezing of Gel. *J. Non. Cryst. Solids* **1983**, *56* (1–3), 411.

(70) Maki, T.; Teranishi, Y.; Kokubo, T.; Sakka, S. Preparation of Porous TiO_2 Fibers by Unidirectional Freezing of Gel. *J. Ceram. Assoc. Japan* **1985**, *93* (1079), 387.

(71) Mukai, S. R.; Nishihara, H.; Shichi, S.; Tamon, H. Preparation of Porous TiO_2 Cryogel Fibers through Unidirectional Freezing of Hydrogel Followed by Freeze-Drying. *Chem. Mater.* **2004**, *16* (24), 4987.

(72) Nishihara, H.; Mukai, S. R.; Fujii, Y.; Tago, T.; Masuda, T.; Tamon, H. Preparation of Monolithic SiO_2 –Al_2O_3 Cryogels with Inter-Connected Macropores through Ice Templating. *J. Mater. Chem.* **2006**, *16* (31), 3231.

(73) Nishihara, H.; Mukai, S. R.; Shichi, S.; Tamon, H. Preparation of Titania–Silica Cryogels with Controlled Shapes and Photocatalysis through Unidirectional Freezing.

Mater. Lett. **2010**, *64* (8), 959.

(74) Nishihara, H.; Mukai, S. R.; Tamon, H. Preparation of Resorcinol–Formaldehyde Carbon Cryogel Microhoneycombs. *Carbon N. Y.* **2004**, *42* (4), 899.

(75) Mukai, S. R.; Nishihara, H.; Yoshida, T.; Taniguchi, K.; Tamon, H. Morphology of Resorcinol–Formaldehyde Gels Obtained through Ice-Templating. *Carbon N. Y.* **2005**, *43* (7), 1563.

(76) Kim, J.-W.; Taki, K.; Nagamine, S.; Ohshima, M. Preparation of Porous Poly(L-Lactic Acid) Honeycomb Monolith Structure by Phase Separation and Unidirectional Freezing. *Langmuir* **2009**, *25* (9), 5304.

(77) Kwon, S.-M.; Kim, H.-S.; Jin, H.-J. Multiwalled Carbon Nanotube Cryogels with Aligned and Non-Aligned Porous Structures. *Polymer (Guildf).* **2009**, *50* (13), 2786.

(78) Mukai, S. R.; Satoh, Y. Development of a Strong Acid Ion Exchange Resin with a Monolithic Microhoneycomb Structure Using the Ice Templating Method. *Ind. Eng. Chem. Res.* **2010**, *49* (21), 10438.

(79) Yoshida, S.; Iwamura, S.; Ogino, I.; Mukai, S. R. Adsorption of Phenol in Flow Systems by a Monolithic Carbon Cryogel with a Microhoneycomb Structure. *Adsorption* **2016**, *22* (8), 1051.

(80) Yoshida, S.; Takahashi, K.; Kudo, S.; Iwamura, S.; Ogino, I.; Mukai, S. R. CO_2 Separation in a Flow System by Silica Microhoneycombs Loaded with an Ionic Liquid Prepared by the Ice-Templating Method. *Ind. Eng. Chem. Res.* **2017**, *56* (10), 2834.

(81) Murakami, K.; Satoh, Y.; Ogino, I.; Mukai, S. R. Synthesis of a Monolithic Carbon-Based Acid Catalyst with a Honeycomb Structure for Flow Reaction Systems. *Ind. Eng. Chem. Res.* **2013**, *52* (44), 15372.

(82) Satoh, Y.; Yokoyama, Y.; Ogino, I.; Mukai, S. R. Synthesis of Sulfonic Acid Functionalized Silica Honeycombs. *Ind. Eng. Chem. Res.* **2013**, *52*, 15293.

(83) Ogino, I.; Suzuki, Y.; Mukai, S. R. Tuning the Pore Structure and Surface Properties of Carbon-Based Acid Catalysts for Liquid-Phase Reactions. *ACS Catal.* **2015**, *5* (8), 4951.

(84) Nishihara, H.; Mukai, S. R.; Yamashita, D.; Tamon, H. Ordered Macroporous Silica

by Ice Templating. *Chem. Mater.* **2005**, *17* (3), 683.

(85) Patrick, W. A. Silica Gel and Process of Making Same. U.S. Patent 1,297,724, 1918.

(86) Tosoh Silica Corporation. Manufacturing Processes http://www.n-silica.co.jp/english/technology/manufact.html (accessed May 6, 2019).

(87) Iler, R. K. *The Chemistry of Silica*; Wiley: New York, 1979.

(88) Pekala, R. W. Organic Aerogels from the Polycondensation of Resorcinol with Formaldehyde. *J. Mater. Sci.* **1989**, *24* (9), 3221.

(89) Mori, T.; Iwamura, S.; Ogino, I.; Mukai, S. R. PMMA-Templated Carbon Gel Monoliths with Independently Tunable Micro-, Meso-, and Macropores. *J. Chem. Eng. Japan* **2017**, *50* (4), 315.

Part 1

Continuous Photocatalytic Degradation of Organic Compounds in Wastewater Using TiO_2−SiO_2 Microhoneycombs Synthesized by the Ice Templating Method

Chapter 2

TiO_2−SiO_2 Microhoneycombs Synthesized from Inexpensive Precursors as Monolithic Photocatalyst Systems

2.1 Introduction

Photocatalytic degradation has been suggested as a technique to treat organic pollutants in wastewater for decades.[1] The technique employs the *in situ* generation of reactive radicals, such as hydroxyl radicals, to degrade the pollutants to benign substances, such as water and carbon dioxide.[2,3] The reactions by the radicals are nonselective, and has been reported for the degradation of recalcitrant molecules that cannot be treated by biological processes.[4–6] Photocatalysis also has an advantage over techniques such as adsorption and coagulation, which merely transfer the pollutants to another concentrated phase without actually destroying them.[4,7,8] Moreover, the reaction conditions are mild, and there are some reports showing that sunlight, which is free and renewable, can be used for photocatalysis as well.[9,10]

Despite many advantages of photocatalysis, the applications of it in commercial scale remains very limited due to the difficulties in scaling up.[11] The configurations for photocatalytic treatment can generally be divided into two types, suspended and immobilized systems.[9,11,12] The suspended systems use photocatalysts in the form of a slurry mixture with the wastewater to be treated, to ensure adequate mixing and mass transfer. However, it is necessary to separate the photocatalysts from the treated effluent, which requires additional cost and makes it difficult to scale up. Immobilization of photocatalysts on a support could be used to avoid the separation step. However, the contact area between the photocatalysts and the fluid to be treated would generally be reduced, and the process is usually limited by mass transfer.

There have been many attempts to intensify photocatalytic reactors. One of the suggested reactor types is a monolithic photoreactor, which is easy to scale up.[13,14] The monoliths consist of straight, parallel channels in the millimeter order, so the surface area of the reactor per unit volume is relatively high compared with flat plate supports. These channels also cause minimal pressure drop when fluids flow through them, and the applications of such monoliths in catalytic converters in cars and other air pollution control devices are common. However, the light intensity would decrease along the length of the monolith due to the shadowing effect of the opaque walls.[15,16] Microreactors are also suggested to be used in photocatalytic reactions.

Because of their small dimensions, heat and mass transfer in them are rapid, so it is easier to adjust reaction conditions. The surface area per volume of the microreactors is also high.[17,18] However, the only way to "scale up" the microreactors is to increase the number of the reactors, which is usually costly. It can be seen that there are many possibilities to further improve photocatalytic systems for wastewater treatment.

There have been reports about the synthesis of porous monoliths with straight microchannels in the micrometer order by using ice crystals as templates.[19] These "microhoneycombs" can be though as a combination of a larger honeycomb and numbered-up microreactors. The thickness of their walls is in the micrometer range, so rapid mass transfer inside the walls could be realized together with a low hydraulic resistance. Because of this, the applications of such monolithic microhoneycombs as sorbents,[20,21] ion-exchange resins,[22] as well as catalysts[23–25] have been suggested. The thin walls are also thought to facilitate radiative transport due to their higher transparency. The previous work by Nishihara et al. demonstrates the application of TiO_2–SiO_2 microhoneycombs as a photocatalyst because it is easier to obtain microhoneycomb samples with high specific surface area (> 500 m^2 g^{-1}) than when pure TiO_2 gels are used.[26] It was found that the monoliths showed higher photocatalytic activities than P25 powder in the degradation of salad oil in batch systems. However, the precursor of TiO_2 used in the previous work is very reactive, so it is difficult to control gelation reactions and the morphology of the resulting material. Application of such microhoneycombs to continuous flow systems, where monoliths can be used to minimize the pressure drop of the systems, have not been conducted as well.

In this chapter, a synthesis method of TiO_2–SiO_2 microhoneycombs from an inexpensive sodium silicate solution and a commercial TiO_2 sol has been developed. The use of a sodium silicate solution as the precursor for SiO_2 resembles the commercial processes to produce silica gels.[27,28] The effect of specific surface area of the photocatalysts to photocatalytic activity was investigated. In addition to reaction experiments in batch systems, reactions in continuous flow systems using decolorization of methylene blue, a common dye, have been investigated as well.

2.2 Materials and Methods

2.2.1 Chemicals

Sodium silicate solution (assay 52.0−57.0 wt%, SiO_2 content 35.0−38.0 wt%, molar ratio between SiO_2 and Na_2O: 2.06−2.31) and 2-methyl-2-propanol (Special Grade, > 99.0%) were purchased from FUJIFILM Wako Pure Chemical Corporation. Ion exchange resin

(Amberlite^{TM} IR120B) was supplied by Organo Japan. Commercial TiO_2 sol (TKS-202, stabilized in nitric acid) was obtained from Tayca. Salad oil, used as a model compound in batch experiments, was obtained from Nisshin Oillio Group. Methylene blue trihydrate, used as a model compound in continuous flow experiments, was purchased from Kanto Chemical. All chemicals were used as received.

2.2.2 Synthesis of TiO_2−SiO_2 Microhoneycombs

TiO_2−SiO_2 microhoneycombs were synthesized according to the method for the synthesis of SiO_2 microhoneycombs previously reported,[19] but with the addition of commercial TiO_2 sol. A sodium silicate solution was first diluted with water to a SiO_2 concentration of 1.9 mol L^{-1}. Then, sodium ions in the solution were removed by ion exchange to obtain a SiO_2 sol at a pH near 3. The prepared sol was incubated at 30 °C. Commercial TiO_2 sol was added to the SiO_2 sol just before the gelation point and mixed in a planetary centrifugal mixer (AR-100, Thinky) at 2000 rpm for 3 min. The amount of TiO_2 in the monolith was set to be 25 mol%. The mixed sol was poured into polypropylene tubes (inner diameter: 12 mm, length: 125 mm) and returned to the incubator for aging. The aging time was set to be equal to the gelation time.

Aged gels were then molded into a microhoneycomb morphology by dipping them into a liquid nitrogen bath (-196 °C) at 6 cm h^{-1} using a modified microfeeder (JP-N, Furue Science, Fig. 2.1). Frozen gels were thawed and cut to 1−3 cm in length. Then, to prevent cracking during drying step, water left in the samples was exchanged with 2-methyl-2-propanol due to its small volume expansion during freezing.[29] The solvent exchange was done at 50 °C for 2 days. The samples were then freeze-dried at -10 °C for 2 days with 4 h prefreezing. After freeze drying, the samples were optionally calcined in air at 600 °C or 1000 °C for 4 h. For comparison, disk-shaped samples containing only TiO_2 were synthesized by drying a commercial TiO_2 sol.

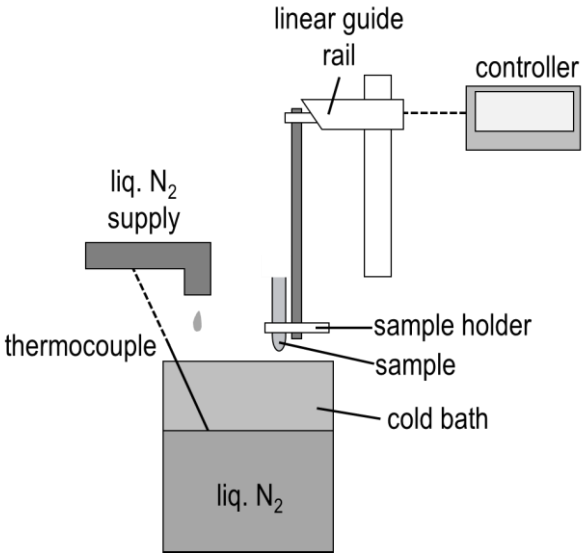

Fig. 2.1 Schematic drawing of a modified micro feeder for unidirectional freezing

2.2.3 Characterization

The morphology of the synthesized microhoneycombs was observed by a scanning electron microscope (SEM, JSM-5410, JEOL). Porous properties of the monolith were measured through nitrogen adsorption experiments conducted at -196 °C. The samples were crushed and pretreated at 250 °C under a nitrogen gas flow. Specific surface area of the samples was calculated by the Brunauer–Emmett–Teller (BET) method. Crystalline phase of TiO_2 in the monoliths was confirmed by x-ray diffraction (XRD, RINT-UltimaIV, Rigaku) using Cu Kα radiation (wavelength: 0.15405 nm).

Hydraulic resistance of the monoliths was determined by pressure drop measurement using a pressure indicator (PZ-200, Copal Electronics). The monoliths were fixed in a heat shrinkable fluorinated ethylene propylene (FEP) tube (FEP-100, AS ONE, inner diameter: 12 mm), and water at 20 °C was used as the testing fluid at a flow rate of 1−10 mL min^{-1}, using a cassette tube pump (SMP-23AS, AS ONE). The microhoneycombs can be modeled as bundles of capillary tubes with a circular open, in which the theoretical pressure drop can be calculated by the Hagen–Poiseuille equation (Eq. 2.1):

$$\Delta P = \frac{32\mu v_s L}{\varepsilon_v D^2} \tag{2.1}$$

Here, ΔP, μ, v_s, L, ε_v, and D denote the pressure drop, the dynamic viscosity of the testing fluid, the superficial velocity of the testing fluid, the length of the monolith, the monolith void fraction (excluding pores in the walls), and the channel diameter, respectively. The average

channel diameter was determined from SEM images. The obtained pressure drop was also compared with that of a packed bed of particles, using the Kozeny–Carman equation (Eq. 2.2):

$$\Delta P = 36k \frac{(1-\varepsilon_v)^2}{\varepsilon_v{}^3} \frac{\mu v_s L}{D_p{}^2} \tag{2.2}$$

Here, k denotes the Kozeny–Carman constant, and D_p denotes the diameter of the particles. The values of k and ε_v were set to 5 and 0.4, both typical values for a bed filled with spherical particles. The value of D_p, the particle size, was set to be equal to the average wall thickness of the microhoneycombs, so that the diffusion path lengths of both systems become the same.

2.2.4 Photocatalytic Activity Measurement

As a preliminary experiment, photocatalytic activity of the synthesized samples in a batch system was measured by the decomposition of salad oil, a common reaction for photocatalytic self-cleaning.[30,31] 12.5 wt% salad oil in 2-methyl-2-propanol was added to the samples. The solvent was removed by freeze drying. Then, dried samples loaded with salad oil were irradiated with a UV light- emitting diode (LED) lamp (LED365-9UV033B, OptoCode Corp.) as a light source at 10 W m^{-2}, and the weight loss was measured. Since weight loss was not observed in dark condition,[26] the weight loss observed during irradiation was solely attributed to photocatalytic decomposition.

Decolorization of methylene blue (MB), a common dye, was selected as a model reaction to measure photocatalytic activity of the samples in a continuous flow system shown in Fig. 2.2. A microhoneycomb sample was fixed in a heat shrinkable FEP tube, and the bottom of the tube was closed by a rubber cap. An aqueous MB solution was continuously fed to the bottom of the monolith by a cassette tube pump in dark condition for more than 24 h to assure adsorption equilibrium. After that, the UV lamp was turned on. The light intensity at the top surface of the sample was kept at 10 W m^{-2}. The liquid overflow was collected and analyzed with a UV-visible spectrophotometer (UV-2400PC, Shimadzu) at the peak absorption wavelength of 665 nm.

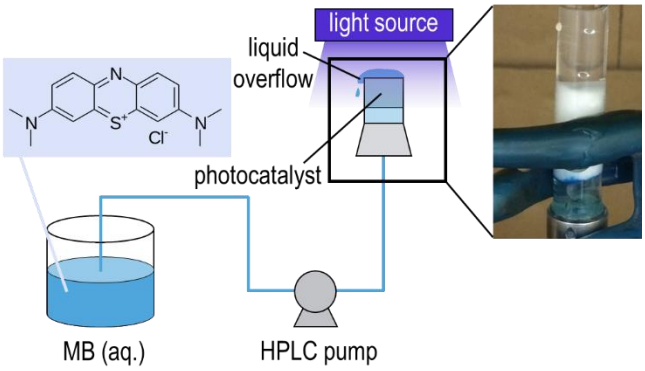

Fig. 2.2 Schematic setting of the photocatalytic system. The inset shows a photograph of a typical sample in the FEP tube, with a rubber cap (inside a stainless steel tube)

2.3 Results and Discussion

2.3.1 Synthesis of TiO_2−SiO_2 Microhoneycombs

Synthesized monoliths have a cylindrical shape molded by the tubes used during gelation. The morphology of the monolith observed by SEM (Fig. 2.3) showed a typical microhoneycomb morphology with an average channel size of 26 μm and a wall thickness of approximately 5 μm. The thin walls of the monolith is expected to facilitate rapid mass transfer.

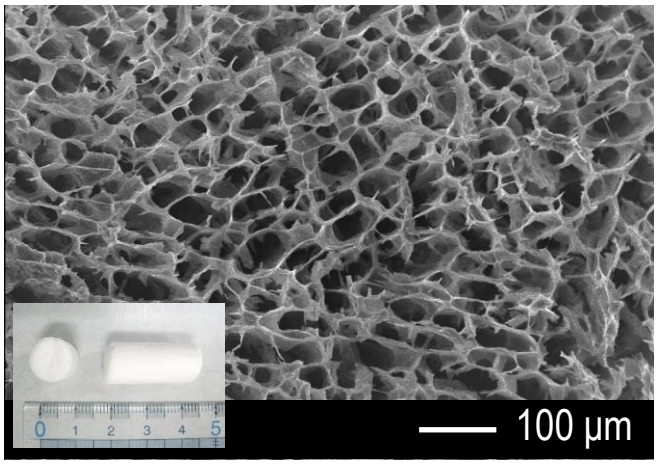

Fig. 2.3 SEM image of a typical uncalcined TiO_2−SiO_2 microhoneycomb. The inset photograph shows the visual appearance of the monolith

Nitrogen adsorption isotherms of a TiO_2−SiO_2 microhoneycomb and a TiO_2 disk are shown in Fig. 2.4. The microhoneycomb sample mainly consisted of micropores, while the TiO_2 disk also contained some small mesopores. In contrast, the BET surface area of the microhoneycomb was approximately twice that of the TiO_2 disk (583 and 250 m^2 g^{-1}, respectively). The kinetic dimensions of fatty acids in salad oil and MB are all approximately

1 nm.[32,33] Therefore, adsorption could occur in micropores. However, the longest dimensions of stearic acid in salad oil and MB molecule are 2.47 nm[34,35] and 1.634 nm,[33] respectively, which suggests that small mesopores might be necessary to facilitate mass transport. Therefore, both the effects from surface area and mesopore volume has to be considered for photocatalytic activity.

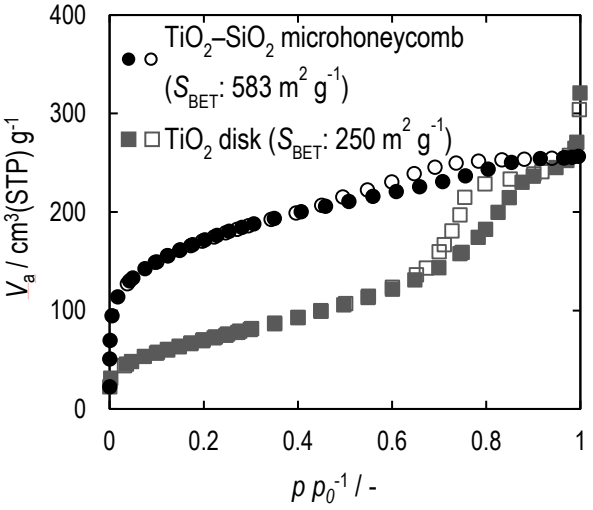

Fig. 2.4 Nitrogen adsorption-desorption isotherms of a typical TiO_2−SiO_2 microhoneycomb (uncalcined), and a TiO_2 disk (solid symbols: adsorption, open symbols: desorption)

2.3.2 Calcination of Microhoneycombs

Metastable anatase, the main crystalline phase of TiO_2 used in photocatalysis, is known to transform to stable rutile after calcination at temperatures over 400 °C.[36–38] Rutile is also generally considered as a less active photocatalyst than anatase.[37] Therefore, calcination at too high a temperature should be avoided. However, as shown in Fig. 2.5, synthesized TiO_2−SiO_2 microhoneycombs did not show any phase transformation even after calcination at 1000 °C, the temperature that lead to complete phase transformation in many experiments. This is probably because of the SiO_2 included in the samples, which is known to inhibit phase transformation of TiO_2 to rutile by restricting intraparticle contact and grain growth.[37,39,40] Calcination in air is also known to inhibit phase transformation (compared with using an inert atmosphere) due to the filling of oxygen vacancies to inhibit the rearrangement of ions to form the rutile phase.

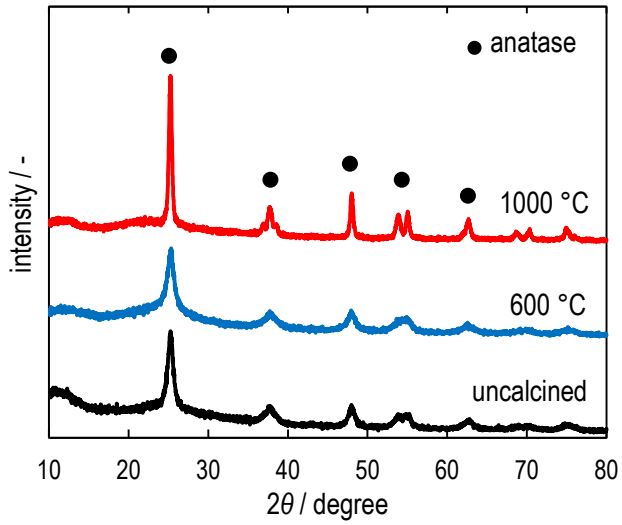

Fig. 2.5 XRD patterns of 10 mol% TiO_2–SiO_2 microhoneycombs calcined at various temperatures

Fig. 2.6 shows the nitrogen adsorption isotherms of TiO_2−SiO_2 microhoneycombs calcined under different temperatures. As expected, densification of SiO_2 occurred,[41] so the BET surface area of the samples decreased with increasing calcination temperature due to pore collapsing. Although the sample calcined at 600 °C could still retain the relatively high surface area of 423 $m^2\ g^{-1}$, the samples calcined at 1000 °C can be considered nonporous. This decrease in surface area is thought to adversely affect the photocatalytic activity.

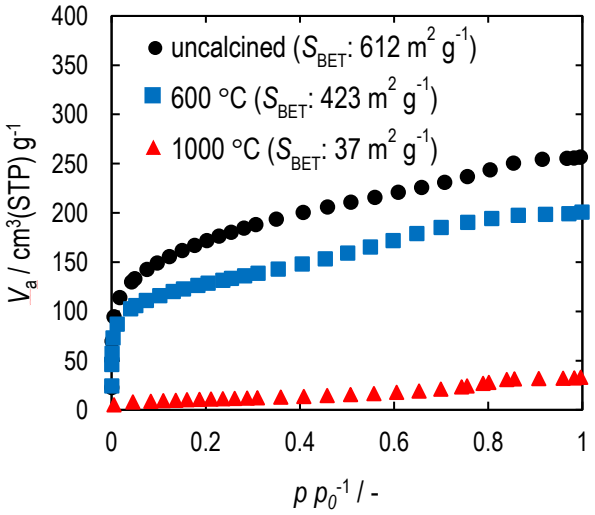

Fig. 2.6 Nitrogen adsorption isotherms of typical TiO_2–SiO_2 microhoneycombs calcined at various temperatures

2.3.3 Hydraulic Resistance

The relatively straight channels of the monolith are expected to cause substantially lower pressure drops in continuous flow systems. This was verified by measuring the pressure drop occurring when water was passed through an uncalcined monolith, and by comparing the values with calculated ones. As shown in Fig. 2.7, the measured pressure drop value was slightly higher than that calculated using the average channel size. This indicates the microhoneycombs can be thought as bundles of capillaries with some tortuosity in the channels. The pressure drop caused by the microhoneycombs was less than a hundredth of that occurring in beds packed with particles with the same diffusion path length. Therefore, it is possible to use such monoliths in systems requiring high flow rate without causing an excessive pressure drop. The result is also in agreement with other studies regarding applications of microhoneycombs in continuous flow systems.[20,23]

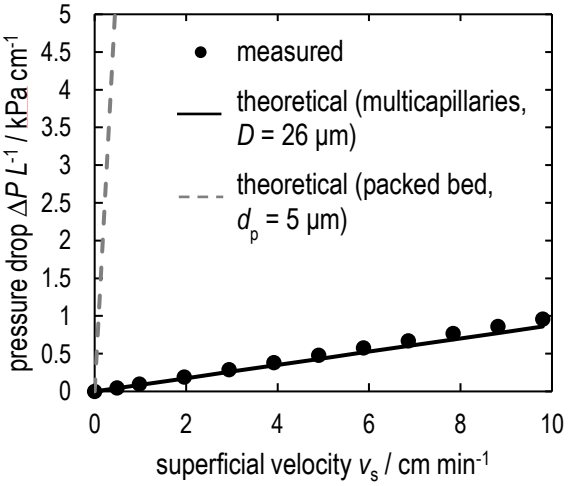

Fig. 2.7 Pressure drop of water (20 °C) flowing through a typical uncalcined TiO_2–SiO_2 microhoneycomb compared with calculated data for multicapillaries and a packed bed column

2.3.4 Photocatalytic Activity in a Batch System

The photocatalytic degradation of salad oil in a batch system using a TiO_2−SiO_2 microhoneycomb, compared with that using a TiO_2 disk, is shown in Fig. 2.8. Synthesized TiO_2−SiO_2 microhoneycombs showed a higher photocatalytic activity than a TiO_2 disk, despite being a composite containing inactive SiO_2. This is because the microhoneycombs have a higher surface area for irradiation due to the inclusion of high surface area SiO_2. The result is

also in agreement with the report about TiO_2−SiO_2 microhoneycombs synthesized from more expensive alkoxides.[26]

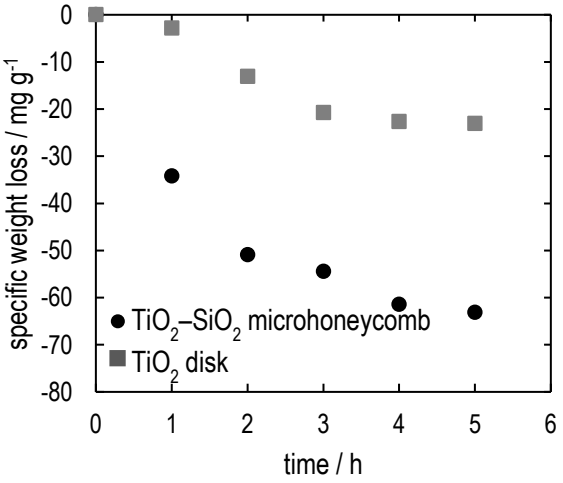

Fig. 2.8 Photocatalytic activity of an uncalcined TiO_2−SiO_2 microhoneycombs and TiO_2 disk in the degradation of salad oil in batch systems

It is known that a monolith with a larger channel size having too high an aspect ratio could not be used effectively for photocatalytic reaction, since the part located farther away from the light source would essentially be in dark condition.[15,16,42] Therefore, the effect of the monolith length was studied. Fig. 2.9a shows that by increasing the length of the monolith from 10 mm to 30 mm, the weight loss also increased. However, when the weight loss was divided by the mass of the monolith, the 30-mm monolith showed a decrease in activity, as shown in Fig. 2.9b. This indicates only the position about 20 mm from the top surface of the monolith was adequately irradiated, and further increase in length would decrease the efficiency of the monolith. A monolith length of 20 mm was selected for continuous flow system studies.

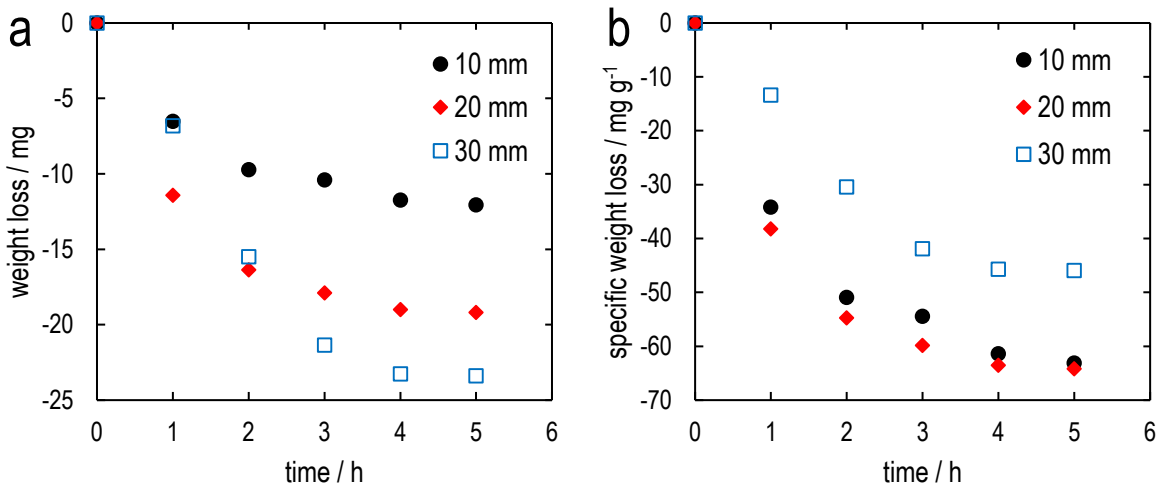

Fig. 2.9 a Weight loss and **b** weight loss per photocatalyst weight of degradation of salad oil in batch systems using uncalcined TiO_2−SiO_2 microhoneycombs with different monolith lengths

2.3.5 Photocatalytic Activity in a Continuous Flow System

Fig. 2.10 shows the photocatalytic activity in decolorization of MB in a continuous flow system using a TiO_2−SiO_2 microhoneycomb, compared with that using a TiO_2 disk. The microhoneycomb showed a higher conversion of 0.44 compared with the value of 0.10 when the TiO_2 disk was used at the same reaction conditions. This is in agreement with the result in the batch system described in the previous section that the high surface area of TiO_2−SiO_2 microhoneycombs is effective in improving photocatalytic activity. To prove this, TiO_2−SiO_2 microhoneycombs with different BET surface areas were synthesized by calcination at different temperatures, and their photocatalytic activity was measured. The results are shown in Table 2.1. As the conversion of MB increased with increasing surface area, it is clear that a high surface area is essential for the microhoneycombs to be effective photocatalysts.

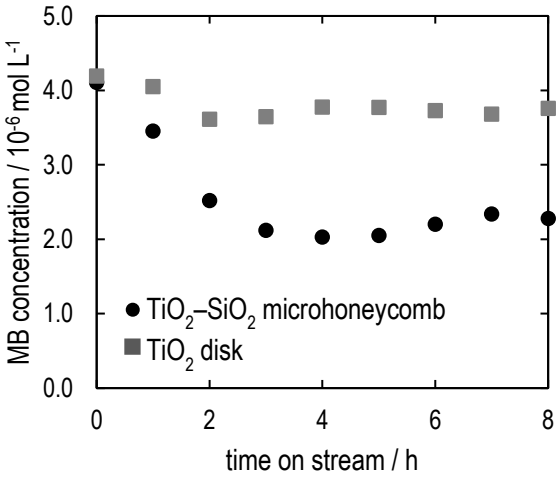

Fig. 2.10 Photocatalytic activity of an uncalcined TiO_2−SiO_2 microhoneycombs and TiO_2 disk in the decolorization of MB in continuous flow systems (feed concentration: 4 μmol L^{-1}, light intensity: 10 W m^{-2}, superficial velocity: 0.23 cm min^{-1})

Table 2.1 BET surface area and conversion of MB of TiO_2−SiO_2 microhoneycombs calcined at various temperatures (feed concentration: 4 μmol L^{-1}, light intensity: 10 W m^{-2}, superficial velocity: 0.23 cm min^{-1})

calcination temperature / °C	S_{BET} **/ m² g⁻¹**	**MB conversion / -**
uncalcined	612	0.44
600	423	0.33
1000	37	0.19

2.4 Conclusions

In this chapter, a synthesis method of TiO_2−SiO_2 microhoneycombs by the ice templating method from an inexpensive sodium silicate solution has been developed. The straight microchannels of the monoliths could minimize the pressure drop caused by the fluid flowing through them, compared with that of beds packed with particles having the same diffusion path length. In addition, the high specific surface area of the synthesized microhoneycombs could

facilitate both mass and radiative transport, leading to increased photocatalytic activity compared with disk-type photocatalysts, both in batch and continuous flow systems. Although calcination of samples at high temperatures did not cause phase transformation of TiO_2 to rutile, the decrease in specific surface area led to lower photocatalytic activity, which highlights the importance of photocatalysts having high surface area. The results indicates the potential of TiO_2−SiO_2 microhoneycombs to be used in continuous flow systems.

References

(1) Mills, A.; Le Hunte, S. An Overview of Semiconductor Photocatalysis. *J. Photochem. Photobiol. A Chem.* **1997**, *108* (1), 1.

(2) Mills, A.; Davies, R. H.; Worsley, D. Water Purification by Semiconductor Photocatalysis. *Chem. Soc. Rev.* **1993**, *22* (6), 417.

(3) Chong, M. N.; Jin, B.; Chow, C. W. K.; Saint, C. Recent Developments in Photocatalytic Water Treatment Technology: A Review. *Water Res.* **2010**, *44* (10), 2997.

(4) Mukherjee, P. S.; Ray, A. K. Major Challenges in the Design of a Large-Scale Photocatalytic Reactor for Water Treatment. *Chem. Eng. Technol.* **1999**, *22* (3), 253.

(5) Dong, H.; Zeng, G.; Tang, L.; Fan, C.; Zhang, C.; He, X.; He, Y. An Overview on Limitations of TiO_2-Based Particles for Photocatalytic Degradation of Organic Pollutants and the Corresponding Countermeasures. *Water Res.* **2015**, *79*, 128.

(6) Gmurek, M.; Olak-Kucharczyk, M.; Ledakowicz, S. Photochemical Decomposition of Endocrine Disrupting Compounds – A Review. *Chem. Eng. J.* **2017**, *310*, 437.

(7) Konstantinou, I. K.; Albanis, T. A. TiO_2-Assisted Photocatalytic Degradation of Azo Dyes in Aqueous Solution: Kinetic and Mechanistic Investigations. *Appl. Catal. B Environ.* **2004**, *49* (1), 1.

(8) Akpan, U. G.; Hameed, B. H. Parameters Affecting the Photocatalytic Degradation of Dyes Using TiO_2-Based Photocatalysts: A Review. *J. Hazard. Mater.* **2009**, *170* (2–3), 520.

(9) Malato, S.; Fernández-Ibáñez, P.; Maldonado, M. I.; Blanco, J.; Gernjak, W. Decontamination and Disinfection of Water by Solar Photocatalysis: Recent Overview and Trends. *Catal. Today* **2009**, *147* (1), 1.

(10) Heggo, D.; Ookawara, S. Multiphase Photocatalytic Microreactors. *Chem. Eng. Sci.* **2017**, *169*, 67.

(11) McCullagh, C.; Skillen, N.; Adams, M.; Robertson, P. K. J. Photocatalytic Reactors for Environmental Remediation: A Review. *J. Chem. Technol. Biotechnol.* **2011**, *86* (8), 1002.

(12) Gaya, U. I.; Abdullah, A. H. Heterogeneous Photocatalytic Degradation of Organic Contaminants over Titanium Dioxide: A Review of Fundamentals, Progress and Problems. *J. Photochem. Photobiol. C Photochem. Rev.* **2008**, *9* (1), 1.

(13) Van Gerven, T.; Mul, G.; Moulijn, J.; Stankiewicz, A. A Review of Intensification of Photocatalytic Processes. *Chem. Eng. Process. Process Intensif.* **2007**, *46* (9), 781.

(14) Sauer, M. L.; Ollis, D. F. Acetone Oxidation in a Photocatalytic Monolith Reactor. *Journal of Catalysis*. 1994, pp 81–91.

(15) Hossain, M. M.; Raupp, G. B. Radiation Field Modeling in a Photocatalytic Monolith Reactor. *Chem. Eng. Sci.* **1998**, *53* (22), 3771.

(16) Alexiadis, A. 2-D Radiation Field in Photocatalytic Channels of Square, Rectangular, Equilateral Triangular and Isosceles Triangular Sections. *Chem. Eng. Sci.* **2006**, *61* (2), 516.

(17) Gorges, R.; Meyer, S.; Kreisel, G. Photocatalysis in Microreactors. *J. Photochem. Photobiol. A Chem.* **2004**, *167* (2–3), 95.

(18) Lindstrom, H.; Wootton, R.; Iles, A. High Surface Area Titania Photocatalytic Microfluidic Reactors. *AIChE J.* **2007**, *53* (3), 695.

(19) Mukai, S. R.; Nishihara, H.; Tamon, H. Formation of Monolithic Silica Gel Microhoneycombs (SMHs) Using Pseudosteady State Growth of Microstructural Ice Crystals. *Chem. Commun.* **2004**, No. 7, 874.

(20) Yoshida, S.; Iwamura, S.; Ogino, I.; Mukai, S. R. Adsorption of Phenol in Flow Systems by a Monolithic Carbon Cryogel with a Microhoneycomb Structure. *Adsorption* **2016**, *22* (8), 1051.

(21) Yoshida, S.; Takahashi, K.; Kudo, S.; Iwamura, S.; Ogino, I.; Mukai, S. R. CO_2 Separation in a Flow System by Silica Microhoneycombs Loaded with an Ionic Liquid

Prepared by the Ice-Templating Method. *Ind. Eng. Chem. Res.* **2017**, *56* (10), 2834.

(22) Mukai, S. R.; Satoh, Y. Development of a Strong Acid Ion Exchange Resin with a Monolithic Microhoneycomb Structure Using the Ice Templating Method. *Ind. Eng. Chem. Res.* **2010**, *49* (21), 10438.

(23) Murakami, K.; Satoh, Y.; Ogino, I.; Mukai, S. R. Synthesis of a Monolithic Carbon-Based Acid Catalyst with a Honeycomb Structure for Flow Reaction Systems. *Ind. Eng. Chem. Res.* **2013**, *52* (44), 15372.

(24) Satoh, Y.; Yokoyama, Y.; Ogino, I.; Mukai, S. R. Synthesis of Sulfonic Acid Functionalized Silica Honeycombs. *Ind. Eng. Chem. Res.* **2013**, *52*, 15293.

(25) Ogino, I.; Suzuki, Y.; Mukai, S. R. Tuning the Pore Structure and Surface Properties of Carbon-Based Acid Catalysts for Liquid-Phase Reactions. *ACS Catal.* **2015**, *5* (8), 4951.

(26) Nishihara, H.; Mukai, S. R.; Shichi, S.; Tamon, H. Preparation of Titania–Silica Cryogels with Controlled Shapes and Photocatalysis through Unidirectional Freezing. *Mater. Lett.* **2010**, *64* (8), 959.

(27) Patrick, W. A. Silica Gel and Process of Making Same. U.S. Patent 1,297,724, 1918.

(28) Tosoh Silica Corporation. Manufacturing Processes http://www.n-silica.co.jp/english/technology/manufact.html (accessed May 6, 2019).

(29) Tamon, H.; Ishizaka, H.; Yamamoto, T.; Suzuki, T. Preparation of Mesoporous Carbon by Freeze Drying. *Carbon N. Y.* **1999**, *37* (12), 2049.

(30) Mills, A.; Lepre, A.; Elliott, N.; Bhopal, S.; Parkin, I. P.; O'Neill, S. A. Characterisation of the Photocatalyst Pilkington Activ^{TM}: A Reference Film Photocatalyst? *J. Photochem. Photobiol. A Chem.* **2003**, *160* (3), 213.

(31) Minabe, T.; Tryk, D. A.; Sawunyama, P.; Kikuchi, Y.; Hashimoto, K.; Fujishima, A. TiO_2-Mediated Photodegradation of Liquid and Solid Organic Compounds. *J. Photochem. Photobiol. A Chem.* **2000**, *137* (1), 53.

(32) Moreno-Calvo, E.; Gbabode, G.; Cordobilla, R.; Calvet, T.; Cuevas-Diarte, M. À.; Negrier, P.; Mondieig, D. Competing Intermolecular Interactions in the High-Temperature Solid Phases of Even Saturated Carboxylic Acids ($C_{10}H_{19}O_2H$ to

$C_{20}H_{39}O_2H$). *Chem. - A Eur. J.* **2009**, *15* (47), 13141.

(33) Zhao, X.; Bu, X.; Wu, T.; Zheng, S. T.; Wang, L.; Feng, P. Selective Anion Exchange with Nanogated Isoreticular Positive Metal-Organic Frameworks. *Nat. Commun.* **2013**, *4* (May), 1.

(34) Lane, C. A.; Burton, D. E.; Crabb, C. C. Accurate Molecular Dimensions from Stearic Acid Monolayers. *J. Chem. Educ.* **1984**, *61* (9), 815.

(35) Schmidt, W. F.; Barone, J. R.; Francis, B.; Reeves, J. B. Stearic Acid Solubility and Cubic Phase Volume. *Chem. Phys. Lipids* **2006**, *142* (1–2), 23.

(36) Yin, S.; Zhang, Q.; Saito, F.; Sato, T. Preparation of Visible Light-Activated Titania Photocatalyst by Mechanochemical Method. *Chem. Lett.* **2003**, *32* (4), 358.

(37) Hanaor, D. A. H.; Sorrell, C. C. Review of the Anatase to Rutile Phase Transformation. *J. Mater. Sci.* **2011**, *46* (4), 855.

(38) Nolan, N. T.; Synnott, D. W.; Seery, M. K.; Hinder, S. J.; Van Wassenhoven, A.; Pillai, S. C. Effect of N-Doping on the Photocatalytic Activity of Sol–Gel TiO_2. *J. Hazard. Mater.* **2012**, *211–212*, 88.

(39) Joo, J. B.; Zhang, Q.; Lee, I.; Dahl, M.; Zaera, F.; Yin, Y. Mesoporous Anatase Titania Hollow Nanostructures Though Silica-Protected Calcination. *Adv. Funct. Mater.* **2012**, *22* (1), 166.

(40) Li, Z.; Hou, B.; Xu, Y.; Wu, D.; Sun, Y.; Hu, W.; Deng, F. Comparative Study of Sol-Gel-Hydrothermal and Sol-Gel Synthesis of Titania-Silica Composite Nanoparticles. *J. Solid State Chem.* **2005**, *178* (5), 1395.

(41) Zhang, L.; D'Acunzi, M.; Kappl, M.; Imhof, A.; Van Blaaderen, A.; Butt, H. J.; Graf, R.; Vollmer, D. Tuning the Mechanical Properties of Silica Microcapsules. *Phys. Chem. Chem. Phys.* **2010**, *12* (47), 15392.

(42) Du, P.; Carneiro, J. T.; Moulijn, J. A.; Mul, G. A Novel Photocatalytic Monolith Reactor for Multiphase Heterogeneous Photocatalysis. *Appl. Catal. A Gen.* **2008**, *334* (1–2), 119.

Chapter 3

Improvement of Synthesis Method of TiO_2−SiO_2 Microhoneycombs

3.1 Introduction

In Chapter 2, a synthesis method for TiO_2−SiO_2 microhoneycombs from an inexpensive sodium silicate solution was developed. It was shown that the high surface area and the unique morphology of the microhoneycombs could be used to increase the photocatalytic activity, as well as minimizing the hydraulic resistance in applications in continuous flow systems. However, to obtain the microhoneycomb morphology by the synthesis method, the acidic TiO_2 sol has to be added to the SiO_2 sol just before the gelation point, which is difficult to determine in the case of SiO_2 systems.[1] SiO_2 sols just before gelation also have a relatively high viscosity, and to uniformly mix TiO_2 sol with this viscous material is challenging. From these aspects, an improved method to synthesize TiO_2−SiO_2 microhoneycombs is preferred.

It is previously reported that the final morphology of the samples synthesized by the ice templating method can be controlled by adjusting the firmness of the gel before unidirectional freezing.[2] If the gel is too soft, a lamella morphology will be obtained. Conversely, if the gel is too firm, polygonal fibers or powders will be obtained instead of a microhoneycomb. In the case of SiO_2-based system, this can be done by adjusting the pH of the sol before gelation.[1] In this chapter, an improved method to synthesize TiO_2−SiO_2 microhoneycombs, using two sources of commercial TiO_2 sol with different stabilization pH, was developed, so that the pH of the sol can be adjusted independently from TiO_2 content. The ratio between the two sources of TiO_2 was adjusted to get the optimal value giving a desired pH value, and the microhoneycombs synthesized by this improved method was compared with those synthesized by the method described in the previous section. In addition, the effect of calcination temperature to the compressive strength, adsorption properties, and photocatalytic activity of the samples was investigated. Finally, the results from photocatalytic systems using TiO_2−SiO_2 microhoneycombs was compared with those from systems using a packed bed of particles having identical TiO_2 content and porous properties, to investigate the effect of morphology.

3.2 Materials and Methods

3.2.1 Chemicals

Sodium silicate solution (assay 52.0–57.0 wt%, SiO_2 content 35.0–38.0 wt%, molar ratio (SiO_2/Na_2O): 2.06–2.31) and 2-methyl-2-propanol (Special Grade) were purchased from Wako. Ion-exchange resin (AmberliteTM IR120B) was supplied by Organo Corp. Two commercial titania sols, one stabilized using nitric acid (TKS-202, 33 wt% TiO_2) and the other in neutral condition (TKS-203, 20 wt% TiO_2), were obtained from Tayca. Methylene blue trihydrate (>98.5 wt%) used as a model substrate was purchased from Kanto Chemical. Azure A (AA) and Azure B (AB), main intermediates generated during decolorization of methylene blue, were supplied by Sigma-Aldrich (as a chloride salt, ~80%) and Wako, respectively.

3.2.2 Synthesis of TiO_2−SiO_2 Microhoneycombs

TiO_2−SiO_2 Microhoneycombs were synthesized according to the method previously reported,[3] similar to the method described in the previous section, but two sources of TiO_2 were used. A sodium silicate solution was diluted by distilled water so that the concentration of SiO_2 became 1.9 mol L^{-1}. Then, sodium ions were removed by addition of an ion-exchange resin to obtain a SiO_2 sol at pH 3. To this freshly prepared SiO_2 sol, acidic TiO_2 sol (TKS-202) was added and mixed vigorously in a planetary centrifugal mixer (AR-100, Thinky) at 2000 rpm for 3 min. Neutral TiO_2 sol (TKS-203) was then added to this mixture by a similar procedure. This order of addition was employed to prevent the mixture from entering the rapid gelation region of SiO_2 sol at pH 4–6[1] and point of zero charge (PZC) of TiO_2 at pH 4.2–6.8.[4] The TiO_2 content from the acidic source was varied from 2 to 5 mol% and the content from the neutral source was added to obtain the desired total TiO_2 content. Because the neutral sol used in the synthesis contained less TiO_2 content than the acidic sol, only samples containing a total TiO_2 content of 10 mol% or lower could be synthesized with reproducibility, so the target TiO_2 content of 10 mol% was selected. The mixture was then poured into polypropylene tubes (inner diameter: 12 mm, length: 125 mm) and incubated at 30 °C for gelation and aging. The aging time of the gels before dipping into a cold bath was set to be half of the gelation time (5–210 min).

Aged gels were then molded into a microhoneycomb morphology by dipping the tubes containing the hydrogels into a cold bath maintained at -196 °C at 6 cm h^{-1} using a modified micro feeder (JP-N, Furue Science). Frozen gels were then thawed, cut to approximately 1 cm in length, and immersed in 2-methyl-2-propanol at 50 °C for 2 days to exchange the water contained in the structure. The gels were freeze-dried at -10 °C for 2 days with 4 h prefreezing.

Because it is known that addition of a second component causes the compressive strength of the resulting monolithic microhoneycombs to decrease,[5] the obtained samples were optionally strengthened by calcination in air at 400–1000 °C. Only the samples with an optimal ratio of TiO_2 for the two sources were used for further characterization.

3.2.3 Characterization

The morphology and elemental composition of synthesized samples were observed by a scanning electron microscope (SEM, SU1510, Hitachi High-Technologies) equipped with energy dispersive X-ray spectrometer (EDS, EDAX Element EDS System, AMETEK). The light irradiation through the monoliths was measured by a UV meter (UV-340, Custom) using a UV LED lamp (LED365-9UV033B, OptoCode Corp.) as the light source. Compressive strength was measured using a load cell (EW-12Ki, A&D). The porous properties of the samples were investigated by nitrogen adsorption (BELSORP-mini, MicrotracBEL) at -196 °C after pretreating the crushed samples at 250 °C for 4 h under a nitrogen gas flow. Specific surface area was calculated using the Brunauer–Emmett–Teller (BET) method. Total pore volume (V_{total}) and micropore volume (V_{micro}) were calculated from the adsorption capacity at relative pressure values of 0.98 and 0.15, respectively. Mesopore volume (V_{meso}) was calculated by subtracting V_{micro} from V_{total}. In addition, surface area of mesopores was calculated by the grand canonical Monte Carlo method, assuming heterogeneous oxygeneous surface with cylindrical pores. To determine surface hydrophilicity, water vapor adsorption (BELSORP-Max, MicrotracBEL) was conducted at 25 °C. Crystal structure of TiO_2 was verified by X-ray diffraction (XRD, RINT-UltimaIV, Rigaku) using Cu Kα radiation (wavelength: 0.15405 nm).

Pressure drop across a monolith fixed in a heat shrink FEP tube (FEP-100, AS ONE, inner diameter: 12 mm) was measured by a pressure indicator (PZ-200, Copal Electronics). Water at 27 °C was used as the testing fluid at a flow rate of 0.1–10 mL min^{-1}. The values were compared with calculated values for multicapillaries having straight channels with circular cross section (Hagen–Poiseulle equation) and a packed bed (Kozeny–Carman equation, assuming spherical particle with the diameter of 5 μm, void fraction of 0.4, and Kozeny–Carman constant of 5).

MB adsorption capacity was determined by batch adsorption at 25 °C. The solution before and after adsorption was collected and analyzed using a UV-visible spectrophotometer (UV-2400PC, Shimadzu) at the wavelength range of 250–800 nm.

3.2.4 Photocatalytic Activity Measurement

Photocatalytic activity of synthesized samples was measured using the decolorization of MB as a model reaction in a system shown in Fig. 3.1. A microhoneycomb sample was fixed in a heat shrinkable FEP tube and a rubber cap was inserted to one side of the tube. Aqueous solution of MB was continuously fed to the bottom of the sample in dark condition for 24 h using a HPLC pump (PU-2080, Jasco) to assure adsorption equilibrium. Then, a UV LED lamp used as the light source was turned on. Liquid overflow was collected in a 3-mL holdup cap for analysis by UV-visible spectrophotometer.

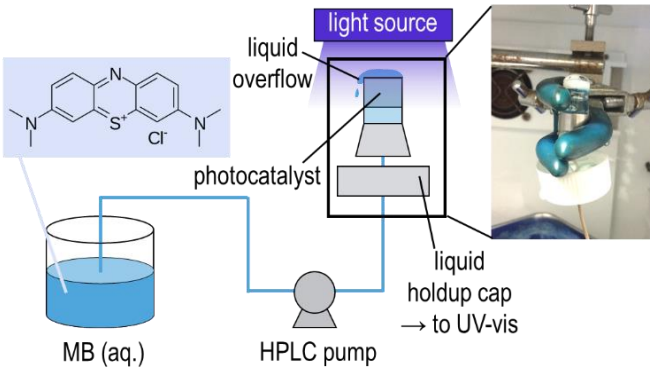

Fig. 3.1 Schematic setting of the photocatalytic system. The inset shows a photograph of a typical sample in the FEP tube, with a rubber cap (inside a stainless steel tube) and a liquid holdup cap

As it is known that photocatalytic degradation of MB generates demethylated intermediates which also show light absorption in the visible region which overlaps with that of MB,[6] it is necessary to separate the peaks of these intermediates from MB peak to correctly determine the conversion of MB. Absorption spectra of AB and AA (1st and 2nd demethylated intermediates, absorption maxima at 648 nm and 631 nm, respectively)[7] were collected and used for deconvolution of the spectra from outlet solution. Deconvolution was done using OriginPro 9.0 using the absorbance data from 540 to 700 nm. The baseline was determined using the data in the range of 740–800 nm. The values of peak center, width, and height ratio of major and minor peaks for each species were fixed, letting only the major peak heights to be varied. Although symmetric Gaussian function are usually used in deconvolution of UV-vis spectra, asymmetric Gaussian function gave the lowest total number of peaks and were used in this work. Effect from dimeric species discussed in the literature[8] was negligible in relatively low concentration (up to 6 μmol L^{-1}) used in this work. Therefore, no adjustments were made.

The peak parameters are shown in Table 3.1 and an example of deconvolution is shown in Fig. 3.2.

Table 3.1 Asymmetric Gaussian peak parameters of MB and intermediates and conversion factor to obtain concentration value. The highest peak for each component is given the height ratio of 1

peak name	**center /nm**	**width1 / nm[a]**	**width2 / nm[a]**	**height ratio / -**	**factor / µmol**
MB1	665.9	21.33	12.66	1	13.196
MB2	612.8	17.09	19.05	0.317	-
MB3	591.6	33.23	67.19	0.160	-
AB1	648.6	50.95	20.42	1	22.452
AB2	669.8	08.18	08.72	0.164	-
AA1	647.4	56.57	18.91	1	25.705
AA2	634.4	37.54	10.09	0.329	-

[a] Values of peak width shown in the table are σ values for left side (1) and right side (2), respectively.

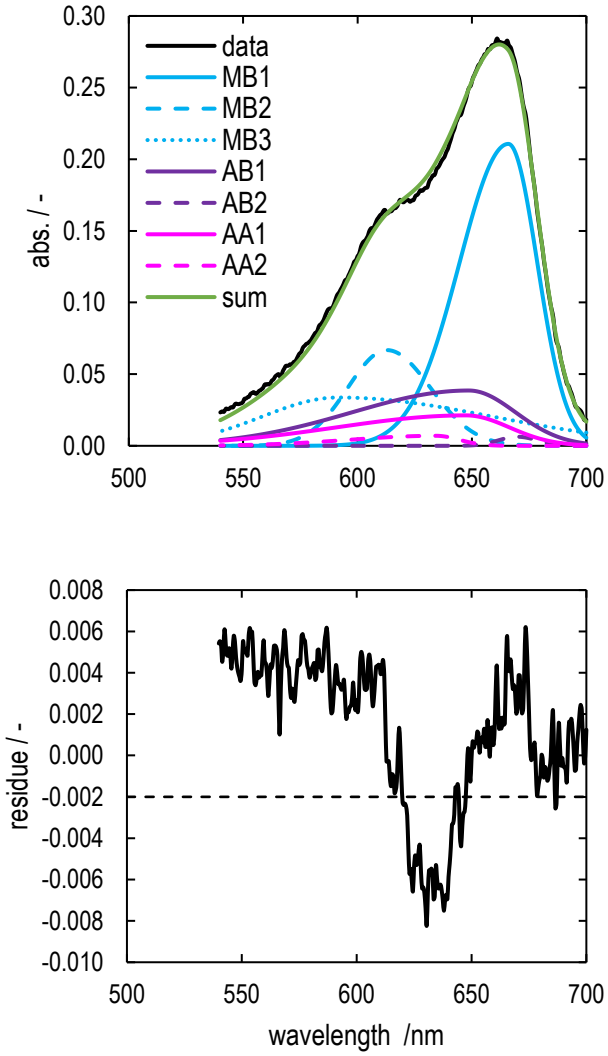

Fig. 3.2 Example of deconvolution of visible spectra collected from the outlet of TiO_2–SiO_2 microhoneycomb during the photocatalytic reaction of MB (sample calcination temperature: 400 °C, MB feed concentration: 4 μmol L^{-1}, superficial velocity: 0.76 cm min^{-1}, light intensity: 10 W m^{-2}, time after turning on the light source: 67 h)

3.3 Results and Discussion

3.3.1 Synthesis of TiO_2−SiO_2 Microhoneycombs

To obtain a microhoneycomb morphology, the firmness of the gel before ice templating should be in the proper range. The firmness was controlled by adjusting the ratio between two TiO_2 sols having different pH, and the results are shown in Table 3.2. Only the sol with the final pH of 2.8−3.0 gave monolithic samples after unidirectional freezing. The mixture with 2.5 mol% TiO_2 from TKS-202 (acidic sol) and 7.5 mol% TiO_2 from TKS-203 (neutral sol) gave a final

pH of 3, which is similar to that of a SiO_2-only sol after ion exchange, and had narrower gelation time range. Therefore, this condition was selected for further investigation.

Table 3.2 Synthesis of TiO_2–SiO_2 monoliths at different TiO_2 contents from acidic sol (TKS-202) and neutral sol (TKS-203)

TiO_2 from acidic sol / mol%	**TiO_2 from neutral sol / mol%**	**pH**	**gelation time / min**	**remarks**
5.0	5.0	1.8	340	long gelation time (low pH), monoliths not obtained
4.0	6.0	2.0	420	
3.0	7.0	2.8	80–225	monoliths obtained, relatively wide gelation time range
2.5	7.5	3.0	60–80	monoliths obtained, relatively narrow gelation time range, optimum condition
2.0	8.0	4.0	10	short gelation time (high pH), monoliths not obtained

Fig. 3.3 shows a SEM image of a typical monolith. It can be seen that a microhoneycomb morphology with channel sizes in the range of 15–40 μm was formed. The wall thickness of the sample was up to 5 μm, which is thought to facilitate the mass transfer of the substrate inside the walls. The actual TiO_2 content from elemental analysis was 13 mol% for a 10 mol% sample. Elemental mapping shows uniform distribution of Ti atoms inside Si matrix, indicating good mixing during synthesis.

In the design of photoreactors, the ratio between the coated surface area (in this case, lateral surface area of the channels) and the volume of the reactor is usually mentioned.[9] In this work, this ratio was estimated by assuming straight, cylindrical channels with a diameter of 15 μm and the number of channels was counted from SEM images. Even by this conservative estimation, this ratio could reach values higher than 20,000 $m^2\ m^{-3}$. Such values are at least an order of magnitude higher than those of honeycombs photoreactors with larger channels and is comparable to those of microreactors.[9–12] Furthermore, the light irradiation experiment shows that although the light was inevitably attenuated along the length of the monolith,

approximately 5% of the initial intensity could be detected at the opposite side of the light source for a 1-cm long sample. Therefore it can be said that the monolith was adequately irradiated. Because of the relatively transparent walls of the microhoneycombs, the irradiation depth is much deeper than in the case of larger honeycombs, where the light intensity dropped to only 1% of the value at the top surface at the depth of three times the opening size,[13] corresponding to the depth of approximately 100 μm for the microhoneycombs.

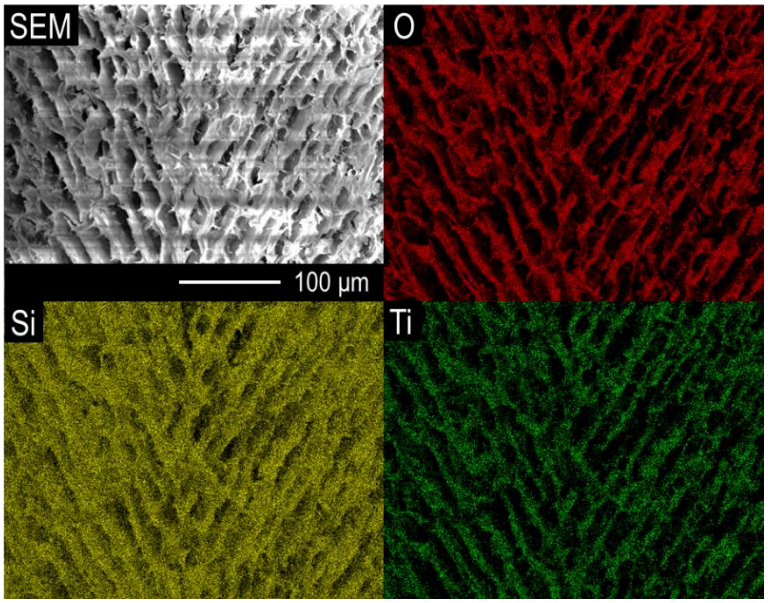

Fig. 3.3 SEM image, and mapping of O, Si, and Ti atoms of a typical uncalcined TiO_2–SiO_2 microhoneycomb

The nitrogen adsorption isotherm of a typical sample (Fig. 3.4) is of type I, indicating microporosity. The adsorption at relative pressure of 0.15–0.40 also indicates small mesopores. These small mesopores are essential for the adsorption of MB and will be discussed later. Although the shape of the adsorption isotherm is of the same type, the BET surface area of the samples synthesized by this improved method was slightly higher than that of the samples synthesized by the method described in Chapter 2 (897 and 583 $m^2\ g^{-1}$, respectively).

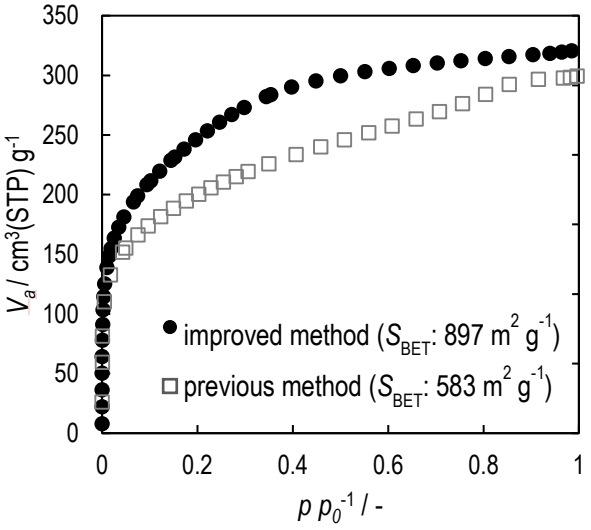

Fig. 3.4 Nitrogen adsorption isotherms of typical uncalcined TiO_2–SiO_2 microhoneycombs synthesized by different methods

The main purpose of calcination in this work is to improve the compressive strength of the monoliths. It is shown in Fig. 3.5 that the strength was successfully increased after calcination due to the condensation of surface silanol groups and structure densification.[14] The compressive strength could be increased to be higher than that of a SiO_2-only monolith (1.1×10^4 kg m^{-2})[5] after calcination at temperature higher than 800 °C. However, it was found that both BET surface area and pore volume decreased with increasing calcination temperature, especially after calcination at 1000 °C, where the obtained samples became almost nonporous. This decrease in surface area usually occurs after calcination due to pore collapsing. A high surface area of more than 500 m^2 g^{-1} could still be maintained even after calcination at 800 °C, so it is still acceptable to calcine the monoliths up to this temperature.

It is also known that the hydrophilicity of both TiO_2 and SiO_2 will change after calcination due to deliberation of water from surface hydroxyl groups. Water vapor adsorption is a useful technique to determine this hydrophilicity. The uptake ratio of water vapor to nitrogen at the relative pressure of 0.15 has been mentioned as a "hydrophilicity index" for zeolites[15], as well as porous carbons[16], and was used in this work. Fig. 3.5 shows that the hydrophilicity of the samples remained relatively unchanged ($X_{0.15}$: 0.50–0.65) after calcination at up to 600 °C, then the samples became significantly more hydrophobic ($X_{0.15}$: 0.18) after calcination at 800 °C. This change in hydrophobicity is expected to affect the adsorption of MB, which could also affect the apparent photocatalytic activity. This will be discussed in the following section. It should be noted that the adsorption capacity of samples calcined at 1000 °C was too low to

obtain a reliable uptake ratio (adsorption capacity of nitrogen: 22.3 cm^3 (STP) g^{-1} at relative pressure of 0.15).

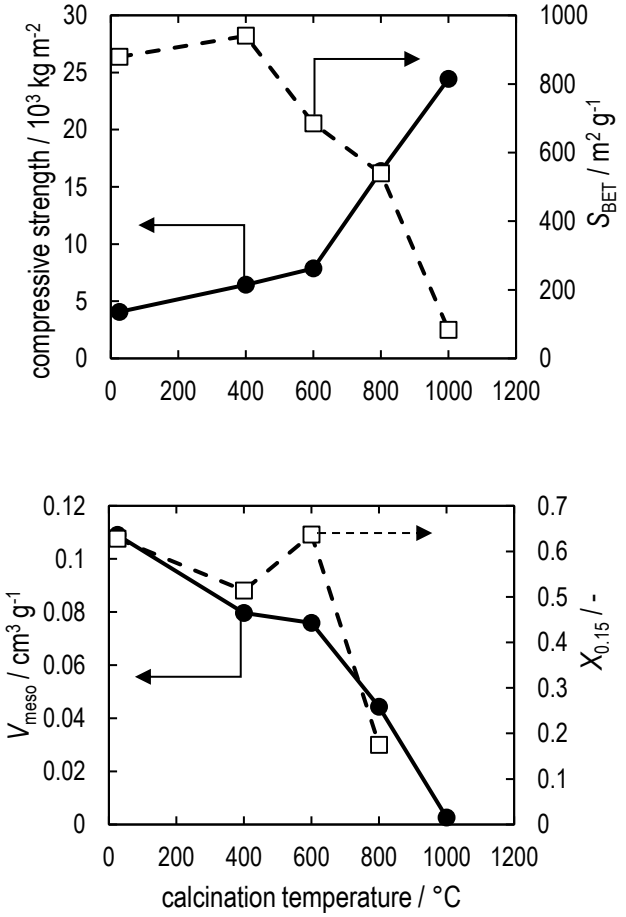

Fig. 3.5 Compressive strength and porous properties of TiO_2–SiO_2 microhoneycombs calcined at various temperatures (data point for uncalcined sample is shown at 25 °C). $X_{0.15}$ denotes the uptake ratio of H_2O and N_2 adsorption at the relative pressure of 0.15.[15] Note that the adsorption capacity of samples calcined at 1000 °C was too low to obtain a reliable uptake ratio.

Crystalline phase of TiO_2 determines the photocatalytic activity of the samples. As stated in Chapter 2, it is preferred to avoid phase transformation of TiO_2 which is likely to occur when the sample is calcined under high temperature. Fig. 3.6 shows that phase change of TiO_2 to rutile occurred after calcination at 1000 °C. At this temperature, the peak of anatase became sharper, indicating aggregation of TiO_2 particles. The phase transformation in samples synthesized by this method occurred at lower temperatures than those synthesized by the method described in Chapter 2, possibly because carbon content in the stabilizer of neutral

TiO_2 promoted the phase transformation to rutile. Even so, the transformation temperature of the samples is still higher than that of typical TiO_2 samples (~ 700 °C). Judging from porous properties and crystalline data, calcination at 1000 °C should be avoided.

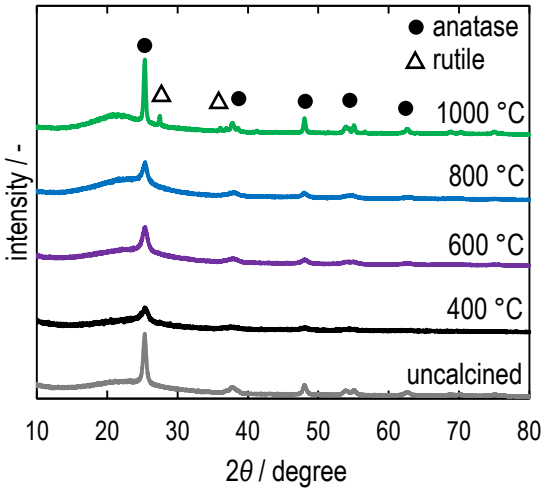

Fig. 3.6 XRD patterns of 10 mol% TiO_2–SiO_2 microhoneycombs, before and after calcination.

3.3.2 Hydraulic Resistance

The hydraulic resistance of a typical microhoneycomb sample was determined by measuring the pressure drop which occurs when water was passed through an uncalcined monolith. As shown in Fig. 3.7, the pressure drop which occurs across the system of a monolithic microhoneycomb is comparable to a bundle of capillaries with a diameter of 12 μm. This diameter size is slightly lower than the typical size of the channels, possibly due to tortuosity. However, it was confirmed that the pressure drop values are less than a hundredth of that of packed bed systems with similar diffusion path lengths. This is in agreement with the result shown in Chapter 2 and in the literature.[17,18]

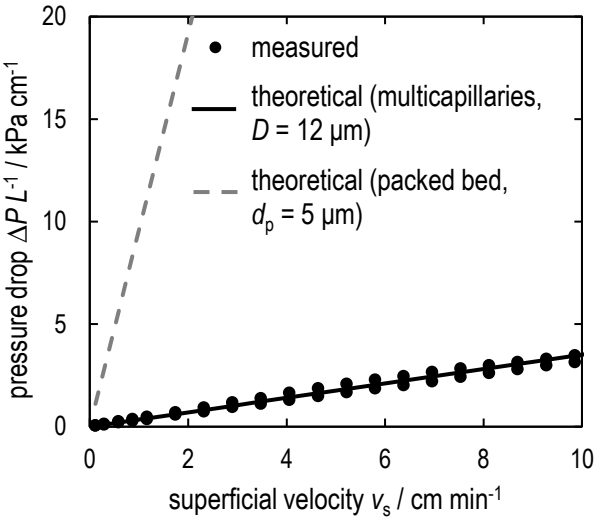

Fig. 3.7 Pressure drop of water (27 °C) flowing through a typical uncalcined TiO_2–SiO_2 microhoneycomb compared with calculated data for multicapillaries and a packed bed column.

3.3.3 Adsorption and Decolorization of MB

The surface coverage of MB on TiO_2–SiO_2 microhoneycombs was determined at an equilibrium concentration of 4 μmol L^{-1}. Due to the relatively large molecular size of MB (longest dimension: 1.634 nm)[19], only the surface area of mesopores (2 nm and larger) is included in the calculation. From Fig. 3.8, samples with a relatively higher hydrophilicity (calcination temperature up to 600 °C), showed slight increase in surface coverage with increasing calcination temperature. Samples calcined at 800 °C, which showed significantly lower hydrophilicity, has the highest MB coverage among the synthesized samples.

Fig. 3.9 compares the concentration change with time on stream between a system using an uncalcined monolith and a system using a monolith calcined at 600 °C. During a few minutes after turning on the light source, a sudden increase of the MB concentration in the outlet flow was observed in the system using an uncalcined monolith. This immediate desorption can be thought as a result of the change in adsorption behavior of the sample under irradiation[20]. Conversely, the system with the calcined monolith did not show such immediate increase. It should be noted that the samples calcined at 600 °C showed higher conversion of MB, so the decolorization rate might be fast enough to decolorize the desorbed MB, and the outlet concentration surge were not observed. The cause of the increase in photocatalytic activity will be discussed later. Both systems reached athe steady state at 4 h.

The photocatalytic activity of the samples calcined at different temperatures was measured, and the effect of surface coverage of MB to the activity is shown in Fig. 3.8. Samples calcined at 600 °C or lower, which have relatively constant hydrophilicity, showed increased activity with increasing surface MB coverage, reaching the maximum MB conversion calcined at 600 °C. Although the BET surface area of the samples decreased with increasing calcination temperature, samples calcined at 600 °C synthesized by this improved method still possessed high surface area of more than 650 m^2 g^{-1} (compared with the value of 423 m^2 g^{-1} for the samples synthesized by the method described in Chapter 2). The retention of this level of surface area is thought to minimally affect the photocatalytic activity.

Although samples calcined at 800 °C have significantly higher surface coverage (0.14 nm^{-2} compared with about 0.05 nm^{-2}) as the hydrophobicity of their surfaces are relatively higher, it is more difficult for water to be adsorbed to such surfaces, leading to a lower production rate of •OH radicals. The surface area of mesopores was also significantly lower than that of samples calcined at 600 °C (114 and 209 m^2 g^{-1}, respectively). These changes in surface properties could possibly be the cause of the decrease in the apparent photocatalytic activity. Finally, samples calcined at 1000 °C not only had a significantly lower surface area, but also contained rutile, which is usually reported as less active than anatase. Therefore, the conversion of MB dramatically decreased. It should be noted that samples calcined at 1000 °C were not completely inactive, but the MB adsorption capacity of them was so low and the conversion did not rise above 13% even at a low flow rate of 0.2 mL/min.

The quantum efficiency is defined as the ratio between the number of molecules transformed and the number of photons interacted with the samples. The value estimated for the most active samples (calcined at 600 °C) was 0.83%. This value is similar to the values reported in the literature for degradation of MB.[21,22]

Although samples calcined at 600 °C performed the best in terms of photocatalytic activity alone, samples calcined at 800 °C may also be used in conditions requiring a high compressive strength. Therefore, it is possible to tune the strength and the activity of TiO_2–SiO_2 microhoneycombs to fit process demands.

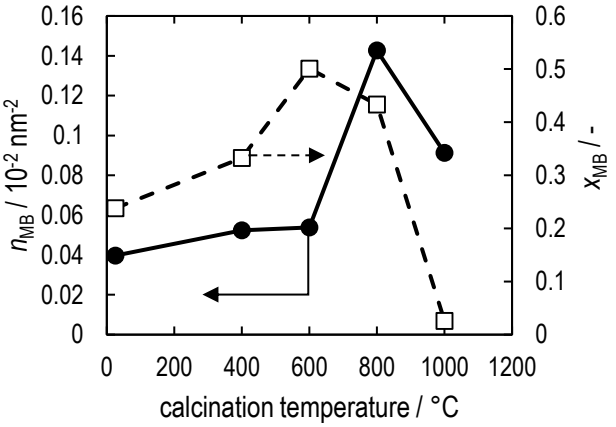

Fig. 3.8 Surface coverage (n_{MB}) and conversion (x_{MB}) of MB over TiO_2–SiO_2 microhoneycombs calcined at various temperatures (feed concentration: 4 μmol L^{-1}, light intensity: 10 W m^{-2}, superficial velocity: 0.76 cm min^{-1}, data point for uncalcined sample is shown at 25 °C). Only the surface area of mesopores was considered in calculation of surface coverage.

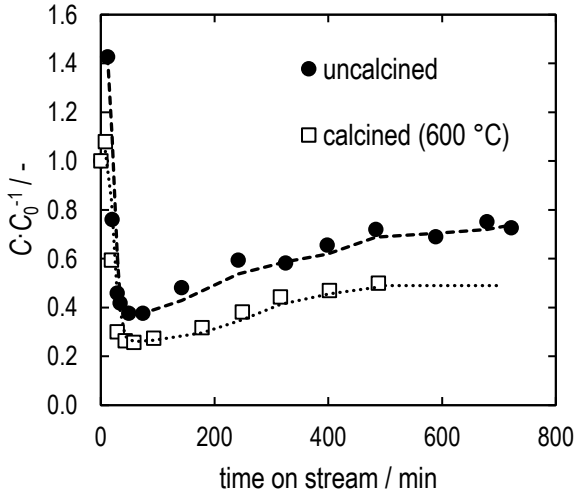

Fig. 3.9 Concentration of MB with time on stream from the outlet of TiO_2–SiO_2 microhoneycombs, uncalcined or calcined at 600 °C (feed concentration: 4 μmol L^{-1}, light intensity: 10 W m^{-2}, superficial velocity: 0.76 cm min^{-1}). Dashed lines are included as a visual guide for steady state concentration. Immediate surge in MB concentration after turning on the light source was possibly due to the change in adsorption behavior after irradiation[20].

Photocatalytic activity of the uncalcined samples synthesized by the improved method introduced in this chapter was also compared with that of the samples synthesized by the

previous method. One disadvantage of the method introduced in this chapter is that the total TiO_2 could not be higher than 10 mol%, so it is natural to assume that samples synthesized by the previous method with 25 mol% would show higher photocatalytic activity given the same reaction conditions. However, when the MB conversion was determined by the method described in the previous chapter (direct measurement of absorbance at 665 nm), uncalcined samples synthesized by the improved method and samples synthesized by the previous method showed similar photocatalytic activity (MB conversion of 0.51 and 0.44, respectively) when the flow rate was set to 0.2 mL min^{-1}. The lower TiO_2 content in the samples synthesized by this improved method was more efficiently utilized due to the uniform distribution achieved by the synthesis method. It is also expected that samples calcined at 600 °C, which is the most active, would show even higher activity in such conditions.

Photocatalytic activity of the uncalcined microhoneycombs was also compared with that of a packed bed of particles. The particles used in this packed bed was made from crushed uncalcined microhoneycombs, therefore, apart from different morphology, the porous properties of the samples in both systems are exactly the same. To avoid fluidization, the flow rate was set to 0.2 mL min^{-1}. It was found that the conversion achieved using a packed bed was quite similar to that achieved using a monolith (0.71 and 0.60, respectively). However, if the packed bed system was not properly set up, the conversion could drop to as low as 0.2 due to non-uniform flow and partial fluidization. This maldistribution can be observed even when quartz wool was placed under the bed to increase the uniformity of the flow (Fig. 3.10). The problems from flow distribution could be avoided in a monolithic system. It was observed that the fluid flow was still well distributed inside the monolith even though the feed flow could contact only a part of the cross section and the steady state conversion could be maintained for more than 40 h. This highlights the ease of sample handling when monolithic samples were used.

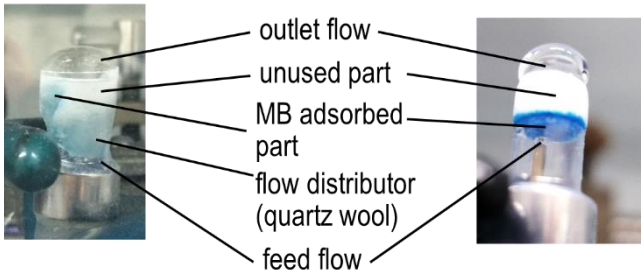

Fig. 3.10 Flow distribution of MB feed in a packed bed from ground microhoneycomb (left) and a monolithic microhoneycomb (right).

3.4 Conclusions

In this chapter, an improved method to synthesize TiO_2−SiO_2 microhoneycomb photocatalysts was developed based on the ice templating method, by using two sources of commercial TiO_2 sols stabilized under different pH values. In addition to the advantages of the ice templating method described in Chapter 2, the improved synthesis method also resulted in uniform distribution of TiO_2, and more active samples could be obtained. It was also found that the straight channels in the microhoneycombs could also help in distributing the feed flow across the monolith while retaining a conversion comparable to that of a system using a packed bed of particles. Finally, calcination of the microhoneycombs at 600–800 °C could improve the strength of the samples, as well as the photocatalytic activity. These results indicate that TiO_2–SiO_2 microhoneycomb photocatalysts synthesized by the method described in this chapter have the potential to be used for wastewater treatment in continuous flow systems.

References

(1) Iler, R. K. *The Chemistry of Silica*; Wiley: New York, 1979.

(2) Mukai, S. R.; Nishihara, H.; Tamon, H. Morphology Maps of Ice-Templated Silica Gels Derived from Silica Hydrogels and Hydrosols. *Microporous Mesoporous Mater.* **2008**, *116* (1–3), 166.

(3) Mukai, S. R.; Nishihara, H.; Tamon, H. Formation of Monolithic Silica Gel Microhoneycombs (SMHs) Using Pseudosteady State Growth of Microstructural Ice Crystals. *Chem. Commun.* **2004**, No. 7, 874.

(4) Liu, X.; Chen, G.; Keller, A. A.; Su, C. Effects of Dominant Material Properties on the Stability and Transport of TiO_2 Nanoparticles and Carbon Nanotubes in Aquatic Environments: From Synthesis to Fate. *Environ. Sci. Process. Impacts* **2013**, *15* (April 2016), 169.

(5) Mukai, S. R.; Mitani, K.; Murata, S.; Nishihara, H.; Tamon, H. Assembling of Nanoparticles Using Ice Crystals. *Mater. Chem. Phys.* **2010**, *123* (2–3), 347.

(6) Zhang, T.; Oyama, T.; Horikoshi, S.; Hidaka, H.; Zhao, J.; Serpone, N. Photocatalyzed *N*-Demethylation and Degradation of Methylene Blue in Titania Dispersions Exposed to Concentrated Sunlight. *Sol. Energy Mater. Sol. Cells* **2002**, *73* (3), 287.

(7) Mohammad, T.; Morrison, H. Simultaneous Photoconjugation of Methylene Blue and

cis-Rh(Phen)$_2$Cl$_2^+$ to DNA via a Synergistic Effect. *Photochem. Photobiol.* **2000**, *71* (4), 369.

(8) Marbán, G.; Vu, T. T.; Valdés-Solís, T. A Simple Visible Spectrum Deconvolution Technique to Prevent the Artefact Induced by the Hypsochromic Shift from Masking the Concentration of Methylene Blue in Photodegradation Experiments. *Appl. Catal. A Gen.* **2011**, *402* (1–2), 218.

(9) Van Gerven, T.; Mul, G.; Moulijn, J.; Stankiewicz, A. A Review of Intensification of Photocatalytic Processes. *Chem. Eng. Process. Process Intensif.* **2007**, *46* (9), 781.

(10) Sauer, M. L.; Ollis, D. F. Acetone Oxidation in a Photocatalytic Monolith Reactor. *Journal of Catalysis*. 1994, pp 81–91.

(11) Lin, H.; Valsaraj, K. T. Development of an Optical Fiber Monolith Reactor for Photocatalytic Wastewater Treatment. *J. Appl. Electrochem.* **2005**, *35* (7–8), 699.

(12) Du, P.; Carneiro, J. T.; Moulijn, J. A.; Mul, G. A Novel Photocatalytic Monolith Reactor for Multiphase Heterogeneous Photocatalysis. *Appl. Catal. A Gen.* **2008**, *334* (1–2), 119.

(13) Hossain, M. M.; Raupp, G. B. Radiation Field Modeling in a Photocatalytic Monolith Reactor. *Chem. Eng. Sci.* **1998**, *53* (22), 3771.

(14) Zhang, L.; D'Acunzi, M.; Kappl, M.; Imhof, A.; Van Blaaderen, A.; Butt, H. J.; Graf, R.; Vollmer, D. Tuning the Mechanical Properties of Silica Microcapsules. *Phys. Chem. Chem. Phys.* **2010**, *12* (47), 15392.

(15) Thommes, M.; Mitchell, S.; Pérez-Ramírez, J. Surface and Pore Structure Assessment of Hierarchical MFI Zeolites by Advanced Water and Argon Sorption Studies. *J. Phys. Chem. C* **2012**, *116* (35), 18816.

(16) Ogino, I.; Suzuki, Y.; Mukai, S. R. Tuning the Pore Structure and Surface Properties of Carbon-Based Acid Catalysts for Liquid-Phase Reactions. *ACS Catal.* **2015**, *5* (8), 4951.

(17) Murakami, K.; Satoh, Y.; Ogino, I.; Mukai, S. R. Synthesis of a Monolithic Carbon-Based Acid Catalyst with a Honeycomb Structure for Flow Reaction Systems. *Ind. Eng. Chem. Res.* **2013**, *52* (44), 15372.

(18) Yoshida, S.; Iwamura, S.; Ogino, I.; Mukai, S. R. Adsorption of Phenol in Flow Systems by a Monolithic Carbon Cryogel with a Microhoneycomb Structure. *Adsorption* **2016**, *22* (8), 1051.

(19) Zhao, X.; Bu, X.; Wu, T.; Zheng, S. T.; Wang, L.; Feng, P. Selective Anion Exchange with Nanogated Isoreticular Positive Metal-Organic Frameworks. *Nat. Commun.* **2013**, *4* (May), 1.

(20) Ollis, D. F. Kinetics of Liquid Phase Photocatalyzed Reactions: An Illuminating Approach †. *J. Phys. Chem. B* **2005**, *109* (6), 2439.

(21) Matthews, R. W. Photocatalytic Oxidation and Adsorption of Methylene Blue on Thin Films of Near-Ultraviolet-Illuminated TiO_2. *J. Chem. Soc. Faraday Trans. 1 Phys. Chem. Condens. Phases* **1989**, *85* (6), 1291.

(22) Houas, A.; Lachheb, H.; Ksibi, M.; Elaloui, E.; Guillard, C.; Herrmann, J.-M. Photocatalytic Degradation Pathway of Methylene Blue in Water. *Appl. Catal. B Environ.* **2001**, *31* (2), 145.

Part 2

Continuous Adsorption of Phenol in Wastewater using Carbon Gel Monoliths with Introduced Straight Microchannels Synthesized by the Fiber Templating Method

Chapter 4

Development of Carbon Gel Monoliths with Introduced Straight Microchannels by the Fiber Templating Method

4.1 Introduction

Phenol and its derivatives are included in wastewater from many industries, such as refineries, petrochemical production, plastics factories, pharmaceuticals, and paper industries.[1,2] Due to its high toxicity to organisms and high environmental impact (lethal dose in human: 50–500 mg kg^{-1})[3], strict standards and regulations have been applied for the concentration of phenol in effluents (as low as 15 ppm for plastic production industries in the US,[4] up to 0.3 ppm in the EU,[5] 5 ppm in Japan)[6]. To treat wastewater with phenol so that the concentration could pass the standard, many treatment techniques were studied, such as liquid-liquid extraction,[7] adsorption (including reactive adsorption),[8,9] biodegradation,[10] wet air oxidation,[11,12] membrane separation,[13] and photocatalysis[14]. Among these techniques, adsorption of phenol using activated carbons (ACs) is very common, especially for the diluted feeds.[2] Activated carbons from solid wastes also have relatively cheap price, and the precursors are widely available.[15–17] However, it is difficult to control the porous structure of the ACs because the structure of them would generally resemble their precursors. Conversely, carbon gels synthesized through the polycondensation of resorcinol and formaldehyde allow the control of porous structure by the adjustment of synthesis method.[18] Because of this, adsorption of phenol using carbon xerogels synthesized by this polycondensation reaction has been reported.[19] Furthermore, the ability to independently tune the micro-, meso-, and macroporosity of carbon gels was demonstrated by the addition of poly(methylmethacrylate) (PMMA) particles as the templates for macropores.[20] Although the method was originally reported for electrochemical applications, it can also be used for applications in adsorption as well, as mesopores and macropores efficiently provide the diffusion pathway for adsorbates.

Another drawback in the use of carbonaceous adsorbents in continuous flow systems is that, the adsorbents are generally used in the form of particles and are packed in columns when used. The hydraulic resistance of the packed particles would be inversely proportional to the particle size, so a relatively large particle size (approximately 0.5 mm) is used to avoid severe pressure drop.[21] On the other hand the use of such large particles would lead to long diffusion path length, and the adsorbents are not used efficiently. This contradiction shows that it is difficult

to realize both short diffusion path length and low hydraulic resistance when the conventional packed bed of particles is used.

Monolithic honeycombs consists of straight, parallel channels with mm-order openings. Due to these straight channels, the pressure drop across the monolith is greatly lower than that of the columns packed with particles, and the monoliths are widely used in catalytic converters for automobiles and air pollution control devices in general, where pressure drop of the system is one of the main issues.[22–24] Applications of monolithic honeycombs for adsorption have been studied as well.[21,25] However, it is difficult to fabricate a monolith to have adequately thin walls, so that mass transfer inside the monolith wall is fast enough.

Synthesis of miniaturized version of monolithic honeycombs, namely "microhoneycombs" using ice crystals as templates was reported for carbon gels.[26] The ice used as templates can be easily removed by thawing, and the template removal step generates no toxic wastes. The synthesized carbon microhoneycombs have a channel size up to 100 μm and thin walls in the micrometer-order. Similar to other microhoneycomb materials, the monoliths are expected to display both short diffusion path length and low hydraulic resistance, and the application of carbon microhoneycombs for phenol adsorption has been reported.[27] However, even though it is possible to change the channel size in the ice templating method, the thickness of the walls also changes with the channel size, and it is difficult to adjust the channel size and the wall thickness independently.[28,29] The thin walls of the monoliths also make them fragile, and the monoliths usually collapse during activation. Therefore, another method to synthesize monoliths with straight microchannels is required.

In this chapter, a new synthesis method to introduce straight microchannels to carbon gel monoliths was proposed. Polyester fibers were selected as templates because they almost completely decompose at the conditions used for carbonization. The name "fiber templating method" was proposed for the synthesis method, and "fiber-templated carbon gel monoliths (FCGMs)" for the synthesized samples. The previous work regarding the synthesis of carbon gels with introduced spherical macropores by PMMA particles showed that the size of the macropores could be easily tuned by changing the size of the template particles.[20] In the same fashion, the size of the microchannels was adjusted by changing the size of the fibers in this work. In addition, the wall thickness (the channel density) of the samples was adjusted by changing the amount of the template fibers. Activation, either physically or chemically, is usually applied to carbon adsorbents to increase their surface area and adsorption capacity.[30]

In this work, physical activation under a CO_2 flow was selected because this method generates less waste than chemical methods. The effects of channel size, wall thickness, and degree of activation to continuous adsorption of phenol in water were then studied.

4.2 Materials and Methods

4.2.1 Chemicals

All chemicals were used without further purifications.

Resorcinol (>99.0%), formaldehyde solution (36.0–38.0%), sodium carbonate (>99.8%), and 2-methyl-2-propanol (>99.0%) were purchased from FUJIFILM Wako Pure Chemical Corporation. Polyester fibers having a diameter of 69 μm were supplied from MonotaRO as a form of paintbrushes. Polyester fibers having a diameter of 104 (Ajing Master #0.4) and 165 μm (Shikake Harris #1) were obtained as fishing lines from Morris and Sunline, respectively.

4.2.2 Synthesis of FCGMs

RF sols were prepared from an aqueous solution of resorcinol (R) and formaldehyde (F), using sodium carbonate (C) as a polycondensation catalyst similar to the procedure reported in the literature [31]. R/C, R/W, and R/F ratios were adjusted to 1000 mol mol^{-1}, 0.5 g mL^{-1}, and 0.5 mol mol^{-1}, respectively. Polyester fibers, cut to a length of approximately 4 cm and aligned to the same direction, were inserted into heat shrinkable fluorinated ethylene propylene (FEP) tubes (FEP-100, AS ONE, inner diameter after heating: 9.0 mm). Then, one side of the tubes was closed using adhesive tape, and the prepared sols were poured into them. The sols were incubated for 48 h at 30 °C for gelation, then incubated for 72 h at 60 °C for aging. Aged gels were immersed in 2-methyl-2-propanol at 50 °C for 2 days, then freeze-dried at -10 °C for 2 days with 4-h prefreezing.

Carbonization and simultaneous template removal were done under a N_2 flow (100 mL min^{-1}) at a 5 °C min^{-1} ramp and holding at 1000 °C for 4 h to obtain fiber-templated carbon gel monoliths (FCGMs). FCGMs were optionally activated at 1000 °C under 16.7 vol% CO_2 in N_2 (total flow rate: 120 mL min^{-1}). The degree of activation is represented by the burn-off ratio (B.O.), which can be calculated by Eq. 4.1

$$\text{B.O. [\%]} = 100 \times \frac{m_i - m_f}{m_i} \tag{4.1}$$

Here, m_i and m_f denote the masses of the sample before and after activation, respectively.

4.2.3 Characterization

Thermogravimetric analysis (TGA, STA 2500 Regulus, NETZSCH) was conducted to observe the decomposition of RF gels before carbonization, as well as fibers used as templates. Approximately 5 mg of the samples were placed under a nitrogen gas flow (20 mL min^{-1}). The final temperature was 1000 °C with a 5 °C min^{-1} ramp. The apparatus was left to cool down naturally after the measurement. The morphology of the samples was observed by scanning electron microscope (SEM, SU1510, Hitachi High-Technologies), and the void fraction of the monoliths (excluding the pores in the walls) was calculated directly from SEM images.

Hydraulic resistance of the monoliths was determined by measuring the pressure drop (PZ-200, Copal Electronics) which occurs across the monolith. The monolith was fixed using a heat shrinkable FEP tube (FEP-070, AS ONE, inner diameter after heating: 6.0 mm) and water at 25 °C was used as the testing fluid at a flow rate of 0.25–10 mL min^{-1}. The values were compared with calculated values assuming the monolith as a bundle of capillaries in which water is flowing as a laminar flow, where the pressure drop can be determined by the Hagen–Poiseuille equation. Pressure drop values of packed beds having the same particle size as the average wall thickness were also calculated as a reference using the Kozeny–Carman equation as a reference, using the value of Kozeny–Carman constant k and void fraction ε_v at 5 and 0.4, respectively. The value of D_p, the particle size, was determined from the average wall thickness T of the corresponding monolith using Eq. 4.2, derived from the geometry of a theoretical monolith with perfectly equally spaced channels with circular openings:

$$T = D\left(\sqrt{\frac{\pi}{2\sqrt{3}\cdot\varepsilon_v}} - 1\right) \tag{4.2}$$

Here, D and ε_v denote the channel diameter and the monolith void fraction, respectively.

Mechanical strength of the monoliths was determined through a crushing test using a load cell (EW-12Ki, A&D). Porous properties of the monoliths were determined by nitrogen adsorption (BELSORP-mini, MicrotracBEL) at -196 °C. Crushed samples were pretreated at 250 °C for 4 h before measurements.

4.2.4 Phenol Adsorption

Phenol adsorption in a batch system was conducted as a preliminary experiment. Samples were crushed then pretreated at 120 °C for 2 h. After pretreatment, 60 g of samples was put into a polytetrafluoroethylene (PTFE)-coated 100-mL polyethylene bottle and 100 mL of an aqueous

solution of phenol at a known concentration was added. The mixture was kept at 30 °C for 24 h to let the concentration reach an equilibrium. The concentration of phenol was determined using a UV-visible spectrophotometer (UV-2400PC, Shimadzu) set at a wavelength of 270 nm. The obtained isotherms were fitted with the Langmuir equation (Eq. 4.3) and Freundlich equation (Eq. 4.4), both frequently used in describing the phenol adsorption isotherms of carbon materials: [9,27,32–34]

$$q = \frac{q_0 K_L C_e}{(1+K_L C_e)} \tag{4.3}$$

$$q = K_F C_e^{\,1/n} \tag{4.4}$$

Here, q and q_0 denote the adsorption capacity and the monolayer capacity of phenol. K_L is the Langmuir parameter. K_F and n denote the Freundlich parameters. C_e is the equilibrium liquid phase concentration of phenol.

The performance of FCGMs was evaluated by adsorption of phenol in a continuous flow system shown in Fig. 4.1. The monoliths were pretreated by the procedure similar to what described above. Pretreated samples were fixed in a heat shrinkable FEP tube (FEP-070, AS ONE, inner diameter after heating: 6.0 mm), which was connected to stainless steel pipes and placed in an oven (CTO-10A V, Shimadzu) maintained at 30 °C. An aqueous phenol solution at 100 ppm was fed to the bottom of the sample by an HPLC pump (PU-2080 Plus, Jasco) and the outlet solution was analyzed continuously by a UV-visible detector (SPD-10A VP, Shimadzu) set at a wavelength of 270 nm. The breakthrough curve was plotted and the length of unused bed (LUB) was calculated by Eq. 4.5:

$$\mathrm{LUB} = \frac{L}{t_s}\,(t_s - t_b) \tag{4.5}$$

Here, L is the length of the bed, and t_s and t_b denote the time when the breakthrough ratio is 0.5 and 0.05, respectively.

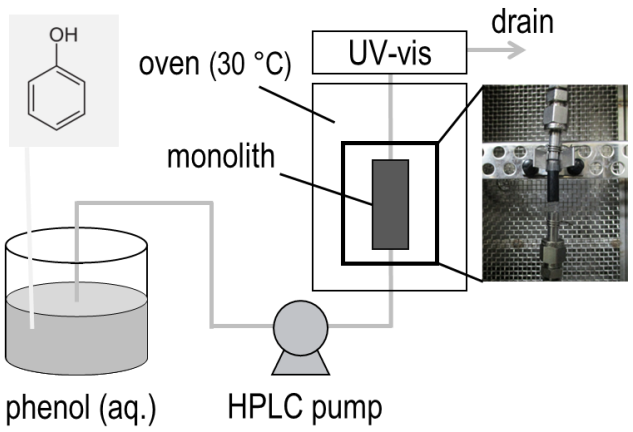

Fig. 4.1 Schematic setting of the continuous flow adsorption system. The photograph shows a typical sample in a FEP tube, connected to stainless steel pipes, inside the oven

4.3 Results and Discussion

4.3.1 Synthesis of FCGMs

Fig. 4.2 shows the TGA data of the synthesized RF gel (before carbonization) and fibers used as templates. It can be seen that at temperature used in carbonization (1000 °C), about 40% of the initial weight of the RF gel remained, while only 8% of the initial weight of the fibers was left. This almost complete decomposition of the fiber suggests the potential of them to be used as templates to introduce microchannels to the monolith.

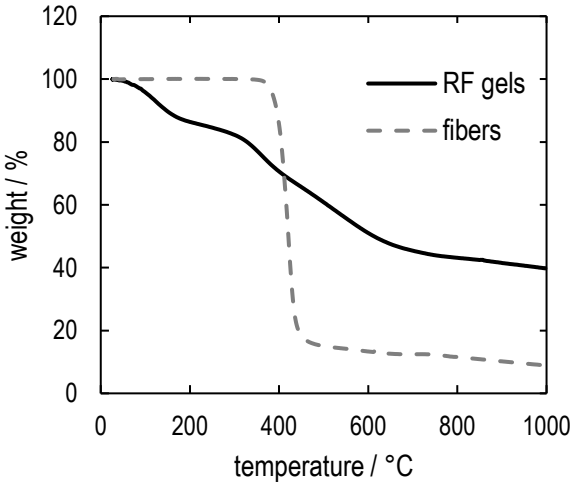

Fig. 4.2 TGA data of typical RF gels (R/C = 1000) before carbonization and polyester fibers (diameter: 165 μm) used as templates

The visual appearance of a typical FCGM is shown in Fig. 4.3a. The monoliths were black cylinders resembling the tubes used during the gelation step. Fig. 4.3b and c shows that straight microchannels with circular opening could be successfully introduced to the monoliths. Although the channel size of the monoliths was slightly smaller than the size of the templates (60 μm and 69 μm, respectively), no serious cracks were observed. This is because the shrinkage percentage of these FCGMs was almost identical to that of carbon gels synthesized without the addition of templates,[35] which indicates that shrinkage occurred uniformly throughout the samples. The distribution of the channel size was narrow, which reflects the uniformity of the template size. This is expected to be beneficial for applications in continuous flow systems, as the hydraulic resistance which occurs in each channel would be approximately the same, and non-uniform flow distribution is more unlikely to occur.

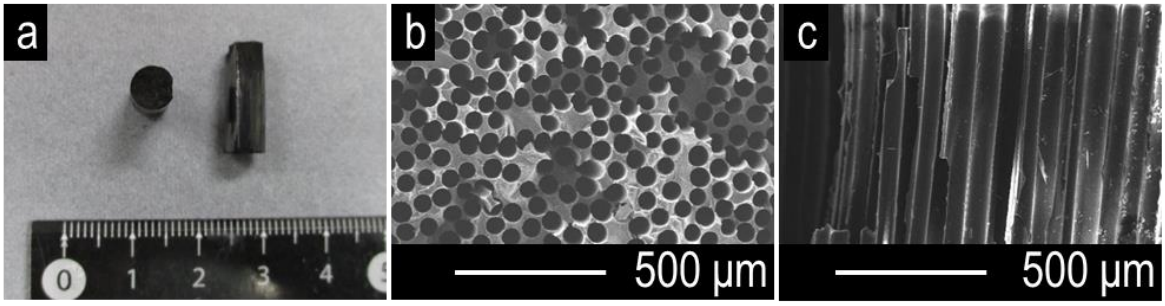

Fig. 4.3 a Photograph of typical FCGMs (fiber diameter: 69 μm, void fraction: 0.50) before activation, showing the top and the side of cylindrical monoliths and SEM images showing **b** cross-section and **c** vertical section of the monolith

Fig. 4.4 show SEM images of FCGMs synthesized to have different channel sizes and channel densities. The adjustment of channel size and channel density could be done by changing the size and the amount of the fibers, which could be done independently. By this adjustment, the wall thickness of the monolith could also be adjusted. Therefore, it is possible to tune the diffusion path length of the monoliths. The void fraction ε_v, was calculated from SEM images, and the maximum ε_v that can be achieved by this method was around 0.6. Above this value, severe cracks formed at the outer surface of the monoliths (Fig. 4.5). Because the void fraction of a bed packed with particles is approximately 0.4 regardless of particle size, this fiber templating method has a potential to improve the performance of adsorption systems.

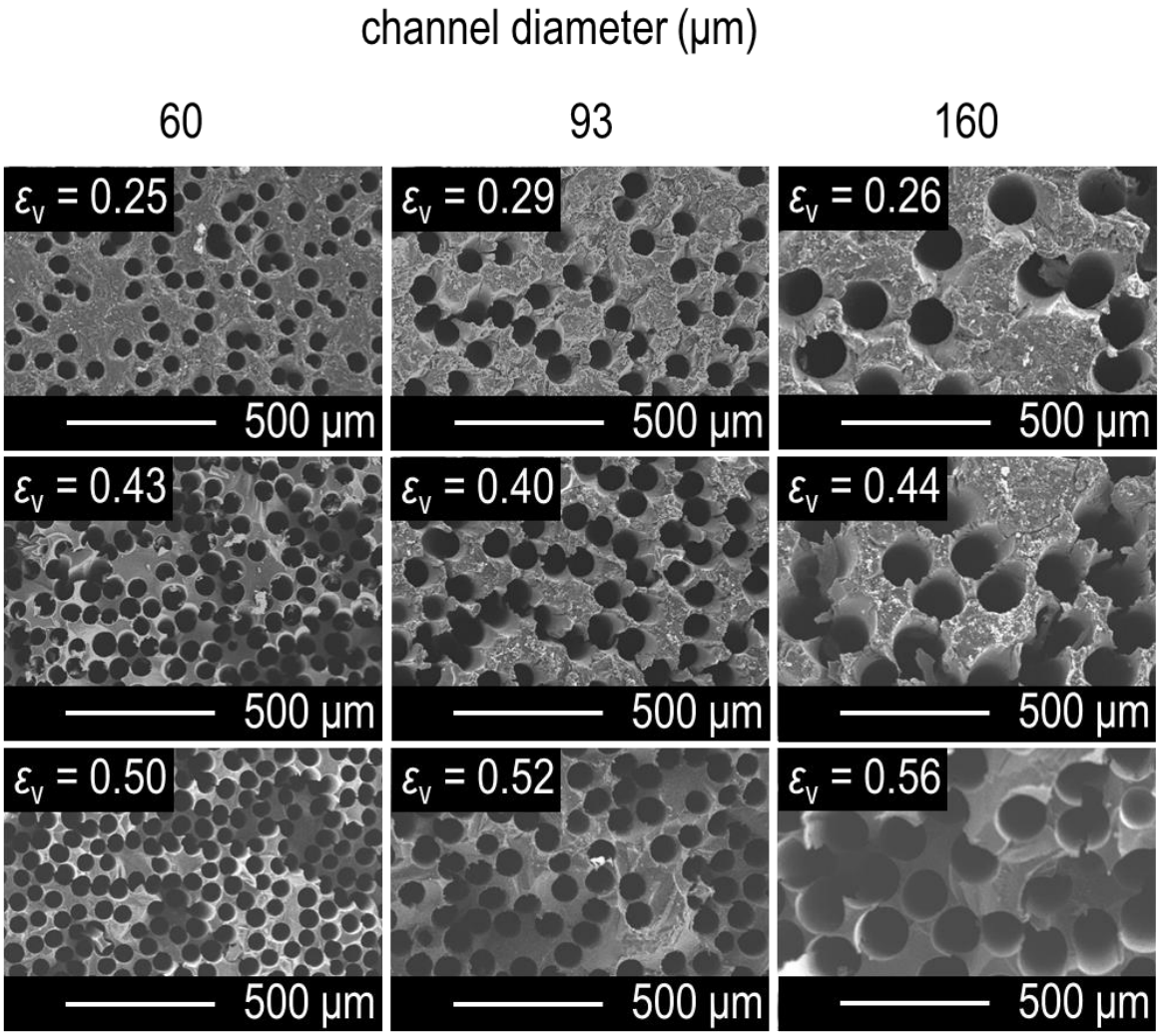

Fig. 4.4 Cross-sectional SEM images of FCGMs before activation, with channel sizes of 60–160 μm and channel densities (in the form of void fraction ε_v) of 0.25–0.56

Fig. 4.5 Visual appearance of a FCGM with an expected void fraction ε_v of 0.69. Severe cracks due to fiber overload can be clearly seen

4.3.2 Hydraulic Resistance

Hydraulic resistance of the monoliths was evaluated by the pressure drop which occurs across the monolith under a water flow. Fig. 4.6 shows that the pressure drop increases linearly with the flow rate, and the calculated values assuming a multicapillary model with a channel size similar to the actual channel size (49, 88 and 146 μm for the actual channel size of 60, 93 and 160 μm, respectively) can be used to describe the system behavior. Due to the straight channels, the pressure drop across the monolith was less than a hundredth of the values for a bed packed with particles having approximately the same diffusion path length. Therefore, the monoliths are expected to allow a high flow rate through them when used in adsorption units. These results are also in agreement with the results in Chapter 2 and 3, as well as those reported for other application of the samples synthesized by the ice templating method.[27,36]

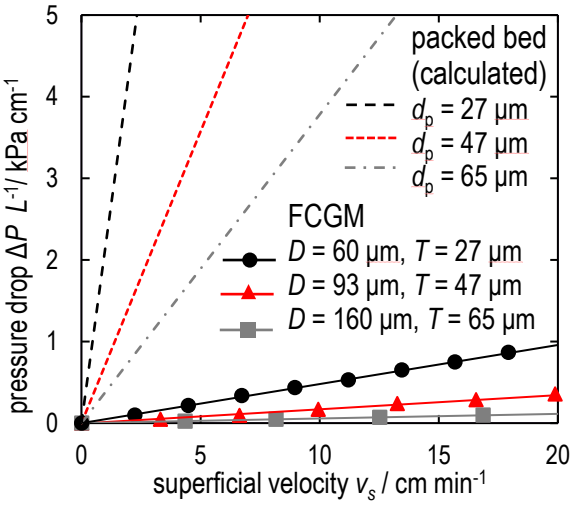

Fig. 4.6 Pressure drop of water (25 °C) flowing through unactivated FCGMs with ε_v = 0.40–0.46 and channel sizes (D) of 60 μm, 93 μm, and 160 μm. Solid lines show calculated data for a bundle of capillaries with similar channel diameters, and broken lines show calculated data for beds packed with particles having the same particle diameter (d_p) as the monolith wall thickness (T)

4.3.3 Activation of FCGMs

Carbon adsorbents are generally activated to increase their surface area and adsorption capacity. The crushing strength of synthesized FCGMs after carbonization was over 12 kg per monolith, which is strong enough for them to be handled without special care at laboratory scale, so they were also thought to be strong enough for activation. As shown in Fig. 4.7a, the visual

appearance of activated monoliths remained unchanged up to a B.O. of about 50%. Above this value, large cracks were observed. The channel structure of the monoliths remained unchanged after activation even at a B.O. value near the limit (Fig. 4.7b and c).

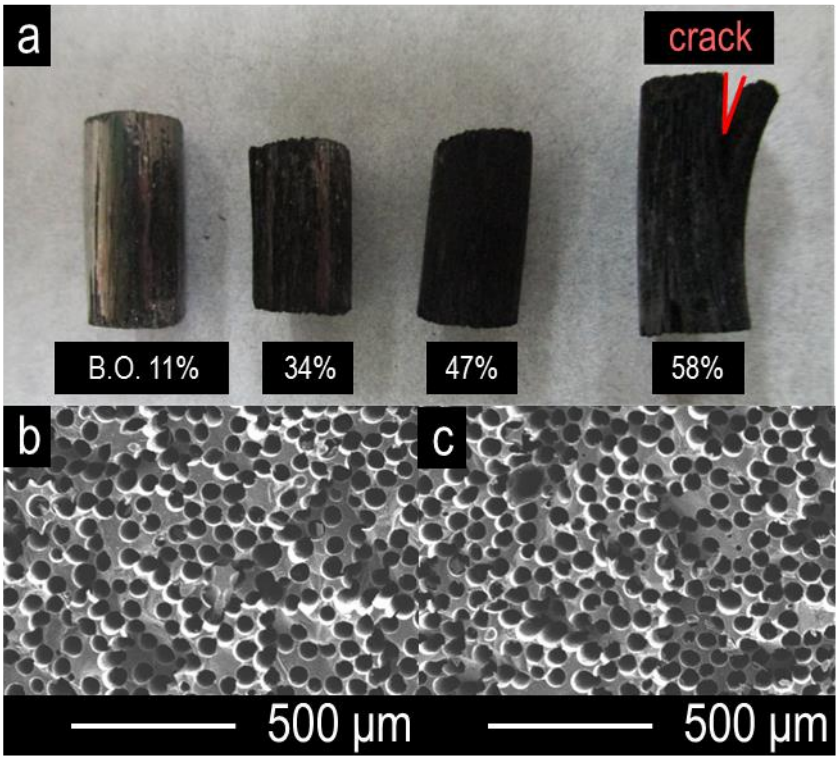

Fig. 4.7 **a** Photograph of FCGMs after activation at B.O. values of 11–58% and SEM images of a typical FCGM at **b** B.O. 0% (before activation) and **c** B.O. 47% (channel size: 60 µm, void fraction: 0.50)

Fig. 4.8 shows nitrogen adsorption isotherms of FCGMs and carbon gels (synthesized without additional templates) at different B.O. values. The values of BET surface area and pore volumes are also shown in Table 4.1. Before activation, the adsorption isotherms of FCGM and carbon gel were almost identical in the lower relative pressure region. However, mesopores were less developed in FCGMs, probably due to the interruption by the template fibers. Because mesopores are crucial in obtaining high surface area carbons [35], the BET surface areas of FCGMs after activation were slightly lower than those of carbon gels. It is still possible to increase the surface area of FCGMs by activation, as the BET surface area increased from 620 $m^2\ g^{-1}$ to up to 1630 $m^2\ g^{-1}$.

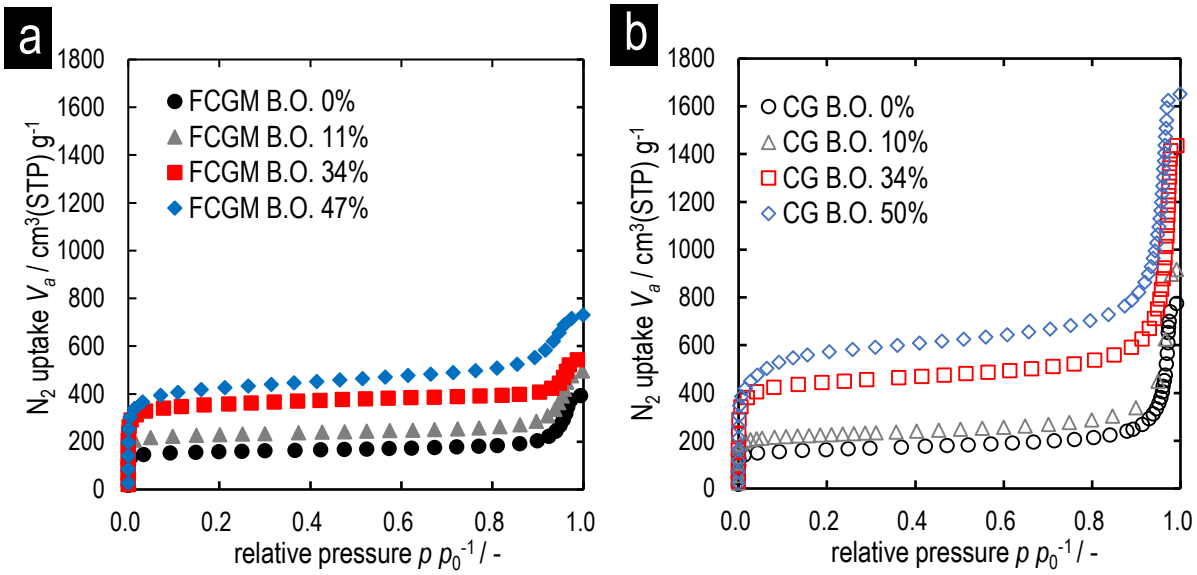

Fig. 4.8 Nitrogen adsorption isotherms of **a** FCGMs (channel size: 60 μm, void fraction: 0.43–0.50) and **b** carbon gels (synthesized without template addition) at B.O. values of 0%, 10–11%, 34%, and 47–50%

Table 4.1 Porous properties of FCGMs (channel size: 60 μm, void fraction: 0.43–0.50) and carbon gels at various degrees of activation

FCGM				CG			
B.O.	S_{BET} / $m^2\ g^{-1}$	V_{micro} / $cm^3\ g^{-1}$	V_{meso} / $cm^3\ g^{-1}$	B.O.	S_{BET} / $m^2\ g^{-1}$	V_{micro} / $cm^3\ g^{-1}$	V_{meso} / $cm^3\ g^{-1}$
0%	620	0.24	0.35	0%	613	0.25	0.90
11%	901	0.35	0.38	10%	875	0.34	1.04
34%	1390	0.55	0.29	34%	1710	0.68	1.51
47%	1630	0.65	0.46	50%	2110	0.87	1.65

4.3.4 Adsorption of Phenol

To evaluate the effect of activation on phenol adsorption capacity, batch adsorption experiments were conducted. The obtained adsorption isotherms are shown in Fig. 4.9a. and the Langmuir and Freundlich parameters are shown in Table 4.2. Although both Langmuir and Freundlich equations can be used to fit these isotherms, the Langmuir equation has better fitting

and was selected for further analysis. The adsorption capacity increased with increasing degree of activation, as expected from larger pore volumes. Because the Langmuir parameter K_L was almost constant for all the investigated samples, the monolayer capacity q_0 of all samples was plotted against their micropore volume, and a nearly linear relationship was obtained (Fig. 4.9b), while the plot using mesopore volume did not show such a linear relationship. This is in agreement with adsorption studies with other carbon adsorbents that adsorption of phenol mostly occurs in the micropores due to its small molecular size.[32]

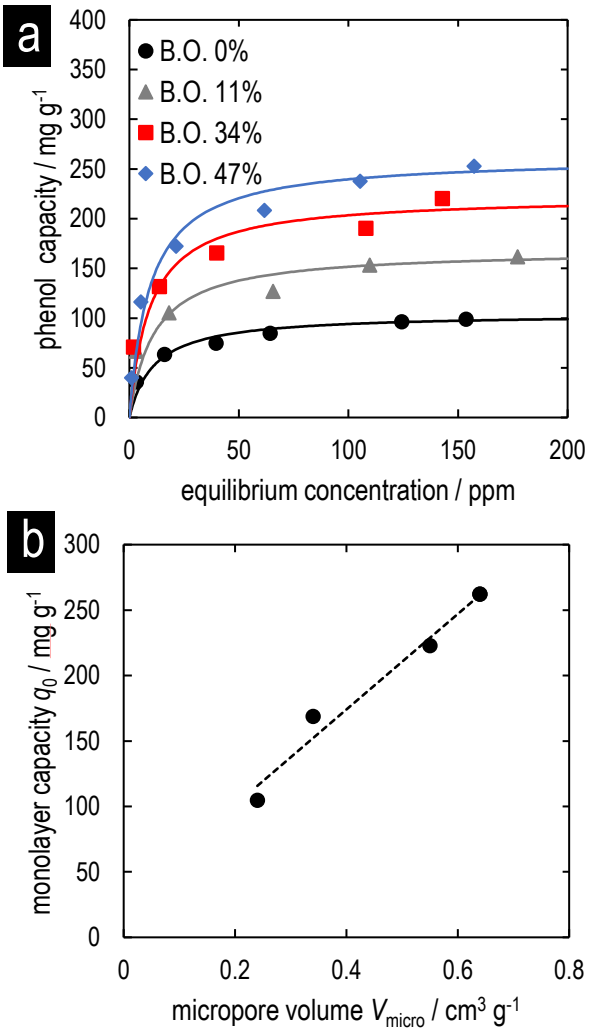

Fig. 4.9 a Phenol adsorption isotherms of FCGMs (channel size: 60 µm, void fraction: 0.43–0.50) with B.O. values of 0%, 11%, 34%, and 47% measured at 30 °C in batch systems. Solid lines show calculated Langmuir isotherms **b** Relationship between the monolayer capacity q_0 and micropore volume. Dashed line was included as a visual guide

Table 4.2 Adsorption parameters for Langmuir and Freundlich equations of FCGMs in batch adsorption of phenol

B.O.	**Langmuir isotherm**			**Freundlich isotherm**		
	K_L / L mg^{-1}	q_0 / mg g^{-1}	R^2 / -	K_F / [(mg g^{-1}) (L mg^{-1})$^{1/n}$]	n / -	R^2 / -
0 %	0.0890	105	0.996	28.1	3.85	0.976
11 %	0.0889	169	0.992	52.6	4.53	0.987
34 %	0.105	223	0.988	62.9	3.97	0.980
47 %	0.107	262	0.996	49.7	2.87	0.923

The phenol adsorption capacity of FCGMs with a channel size of 60 μm, void fraction of 0.50 and various degrees of activation was also measured in a continuous flow system, and the obtained breakthrough curves are shown in Fig. 4.10a. The phenol adsorption capacity at equilibrium concentration was compared between batch and continuous flow system (Fig. 4.10b) and the capacity obtained were approximately the same, with the exception of B.O. 0% samples. This could be due to the carbonaceous residue from the fibers which had surface properties different from the carbon from RF gels, which is the major constituent and which was exposed by grinding prior to batch experiments. The residue from fiber is thought to be removed during activation. For samples after activation, the results indicate that the monoliths were effectively used as adsorbents for phenol in a continuous flow system.

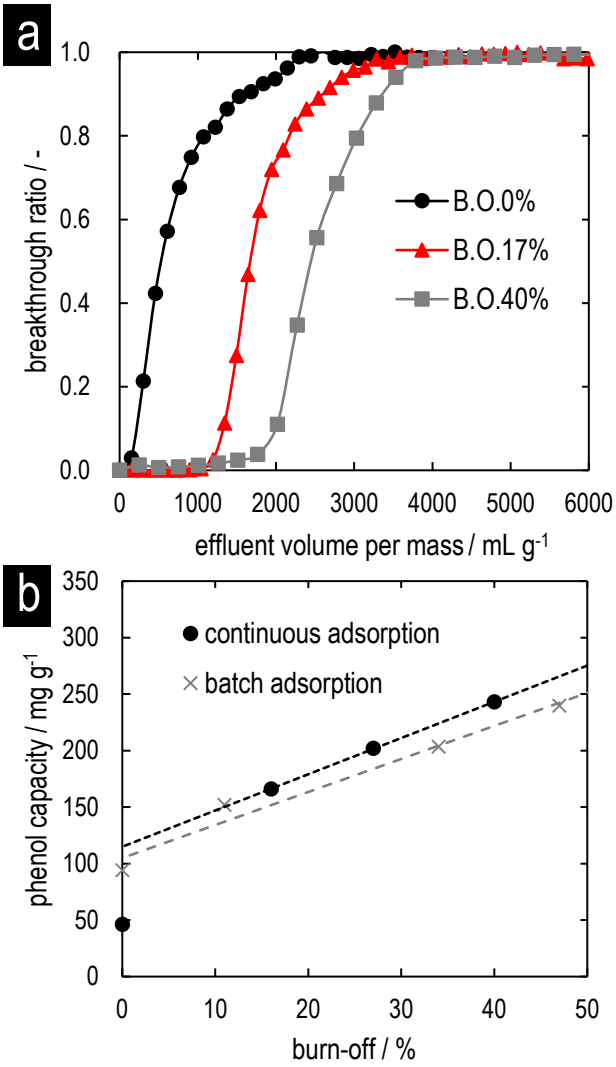

Fig. 4.10 a Phenol breakthrough curves of FCGMs with a channel size of 60 μm, a void fraction ε_v of 0.5, and B.O. values of 0%, 17%, and 40% **b** Comparison of phenol adsorption capacity in a continuous flow system and a batch system at an equilibrium concentration of 100 ppm and adsorption temperature of 30 °C. Broken lines were included as visual guides

As the synthesized FCGMs showed promising results to be used as effective adsorbents for phenol removal, the effects of channel size and channel density on phenol adsorption abilities in continuous flow systems were investigated. Breakthrough experiments were conducted using monoliths having different channel sizes (void fraction: 0.39, B.O.: 18–19%) and the results are shown in Fig. 4.11. When the size of the channels was 100 μm or smaller, no apparent differences in the breakthrough curves could be seen. However, the breakthrough curves obtained with a monolith with 160-μm channels was slightly more dispersed compared with samples with small channels. Calculated LUB (entries 1–3 in Table 4.3) shows that the

value almost tripled when the channel size was increased from 93 μm to 160 μm (0.4 and 1.1 cm, respectively), while the capacity was comparable. This could be caused by the increase of wall thickness along with the increase in channel size, leading to the increase in the required diffusion time for phenol to reach the center of the wall thickness. These results indicates that the channel size has to be about 100 μm or smaller for the FCGMs to be used as effective adsorbents.

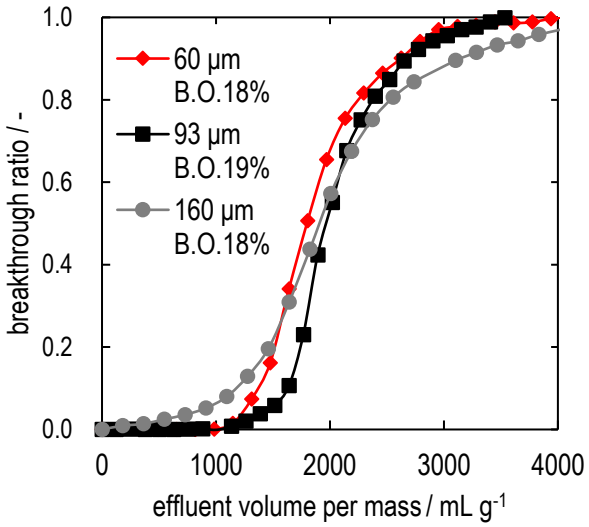

Fig. 4.11 Phenol breakthrough curves of FCGMs with a void fraction ε_v of 0.39, a B.O. in the range of 18–19%, and channel sizes of 60 μm, 93 μm, and 160 μm (feed concentration: 100 ppm, temperature: 30°C)

Table 4.3 Phenol adsorption capacity and LUB in continuous flow systems using FCGMs having various channel sizes and channel densities

entry	channel size / μm	wall thickness / μm	void fraction / -	monolith length / cm	B.O.	capacity / mmol g^{-1}	LUB / cm
1	60	31	0.39	1.8	18%	180	0.5
2	93	49	0.39	1.9	19%	195	0.4
3	160	84	0.39	2.1	18%	190	1.1
4	60	21	0.50	1.7	17%	166	0.4
5	60	71	0.19	2.0	15%	121	1.0

The effect of channel density (void fraction) on adsorption in continuous flow systems was investigated for monoliths with 60-μm channels (B.O.: 15–18%). The obtained data are shown in entries 1, 4 and 5 in Table 4.3, and the breakthrough curves are shown in Fig. 4.12. When the thickness of the wall exceeds 60 μm, the breakthrough curve became more dispersed, LUB doubled (from 0.4–0.5 cm to 1.0 cm), and the adsorption capacity decreased by more than 25%. This could also be explained by the increase in the required diffusion time due to thicker walls mentioned previously. From the results, the thickness of the walls should be 70 μm or below.

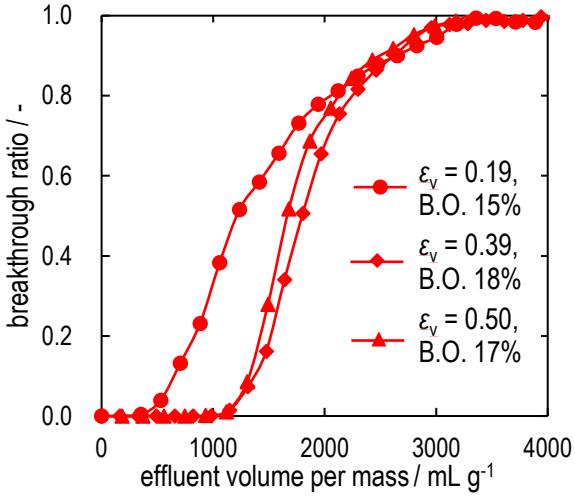

Fig. 4.12 Phenol breakthrough curves of FCGMs with a channel size of 60 μm, a B.O. in the range of 15–18%, and void fractions ε_v of 0.19, 0.39, and 0.50 (feed concentration: 100 ppm, temperature: 30°C)

4.4 Conclusions

In this chapter, a new method to synthesize carbon gel monoliths with introduced straight microchannels was developed. The proposed "fiber templating method" has an advantage over the ice templating method discussed in Part 1 that it allows the independent control of channel size and channel density, by simply changing the size and the amount of the template fibers, respectively. Synthesized monoliths also had adequate mechanical strength to be activated to increase their volume of micropores, and, in turn, adsorption capacity of phenol, without altering the overall morphology. Phenol adsorption experiments in continuous flow systems shows that monoliths with a channel size in the range of 60–93 μm and a wall thickness of up to 70 μm could adsorb phenol effectively. The results indicates the potential of the synthesis method to synthesize adsorbents which the dimensions could be tuned to fit the process demands.

References

(1) Busca, G.; Berardinelli, S.; Resini, C.; Arrighi, L. Technologies for the Removal of Phenol from Fluid Streams: A Short Review of Recent Developments. *J. Hazard. Mater.* **2008**, *160* (2–3), 265.

(2) Mohammadi, S.; Kargari, A.; Sanaeepur, H.; Abbassian, K.; Najafi, A.; Mofarrah, E.

Phenol Removal from Industrial Wastewaters: A Short Review. *Desalin. Water Treat.* **2015**, *53* (8), 2215.

(3) National Library of Medicine (US). Hazardous substances data bank [Internet] https://toxnet.nlm.nih.gov/cgi-bin/sis/search2/r?dbs+hsdb:@term+@DOCNO+113 (accessed Sep 18, 2018).

(4) Code of Federal Regulations, Title 40, section 414.91, Toxic pollutant effluent limitations and standards for direct discharge point sources that use end-of-pipe biological treatment. https://www.govinfo.gov/app/details/CFR-2018-title40-vol31/CFR-2018-title40-vol31-sec414-91/summary (1993) (accessed Sep 19, 2018)

(5) The European Commission. establishing best available techniques (BAT) conclusions for waste treatment, under Directive 2010/75/EU of the European Parliament and of the Council https://eur-lex.europa.eu/eli/dec_impl/2018/1147/oj (accessed May 9, 2019).

(6) Government of Japan. Ministry of the Environment.: National Effluent Standards http://www.env.go.jp/en/water/wq/nes.html (accessed Sep 19, 2018).

(7) Jiang, H.; Fang, Y.; Fu, Y.; Guo, Q.-X. Studies on the Extraction of Phenol in Wastewater. *J. Hazard. Mater.* **2003**, *101* (2), 179.

(8) Sharma, M.; Vyas, R. K.; Singh, K. Theoretical and Experimental Analysis of Reactive Adsorption in a Packed Bed: Parallel and Branched Pore-Diffusion Model Approach. *Ind. Eng. Chem. Res.* **2016**, *55* (20), 5945.

(9) Otero, M.; Zabkova, M.; Rodrigues, A. E. Adsorptive Purification of Phenol Wastewaters: Experimental Basis and Operation of a Parametric Pumping Unit. *Chem. Eng. J.* **2005**, *110* (1–3), 101.

(10) Veeresh, G. S.; Kumar, P.; Mehrotra, I. Treatment of Phenol and Cresols in Upflow Anaerobic Sludge Blanket (UASB) Process: A Review. *Water Res.* **2005**, *39* (1), 154.

(11) Kim, K.-H.; Ihm, S.-K. Heterogeneous Catalytic Wet Air Oxidation of Refractory Organic Pollutants in Industrial Wastewaters: A Review. *J. Hazard. Mater.* **2011**, *186* (1), 16.

(12) Mishra, V. S.; Mahajani, V. V.; Joshi, J. B. Wet Air Oxidation. *Ind. Eng. Chem. Res.* **1995**, *34* (1), 2.

(13) Bódalo, A.; Gómez, E.; Hidalgo, A. M.; Gómez, M.; Murcia, M. D.; López, I. Nanofiltration Membranes to Reduce Phenol Concentration in Wastewater. *Desalination* **2009**, *245* (1–3), 680.

(14) Inumaru, K.; Yasui, M.; Kasahara, T.; Yamaguchi, K.; Yasuda, A.; Yamanaka, S. Nanocomposites of Crystalline TiO_2 Particles and Mesoporous Silica: Molecular Selective Photocatalysis Tuned by Controlling Pore Size and Structure. *J. Mater. Chem.* **2011**, *21* (32), 12117.

(15) Crini, G. Non-Conventional Low-Cost Adsorbents for Dye Removal: A Review. *Bioresour. Technol.* **2006**, *97* (9), 1061.

(16) Salleh, M. A. M.; Mahmoud, D. K.; Karim, W. A. W. A.; Idris, A. Cationic and Anionic Dye Adsorption by Agricultural Solid Wastes: A Comprehensive Review. *Desalination* **2011**, *280* (1–3), 1.

(17) Rengaraj, S.; Moon, S.-H.; Sivabalan, R.; Arabindoo, B.; Murugesan, V. Agricultural Solid Waste for the Removal of Organics: Adsorption of Phenol from Water and Wastewater by Palm Seed Coat Activated Carbon. *Waste Manag.* **2002**, *22* (5), 543.

(18) Pekala, R. W. Organic Aerogels from the Polycondensation of Resorcinol with Formaldehyde. *J. Mater. Sci.* **1989**, *24* (9), 3221.

(19) Rodrigues, L. A.; Campos, T. M. B.; Alvarez-Mendes, M. O.; Coutinho, A. D. R.; Sakane, K. K.; Thim, G. P. Phenol Removal from Aqueous Solution by Carbon Xerogel. *J. Sol-Gel Sci. Technol.* **2012**, *63* (2), 202.

(20) Mori, T.; Iwamura, S.; Ogino, I.; Mukai, S. R. PMMA-Templated Carbon Gel Monoliths with Independently Tunable Micro-, Meso-, and Macropores. *J. Chem. Eng. Japan* **2017**, *50* (4), 315.

(21) Patton, A.; Crittenden, B. D.; Perera, S. P. Use of the Linear Driving Force Approximation to Guide the Design of Monolithic Adsorbents. *Chem. Eng. Res. Des.* **2004**, *82* (8), 999.

(22) de Nevers, N. *Air Pollution Control Engineering*, 2nd ed.; McGraw-Hill Education (Asia): Singapore, 2000.

(23) Farrauto, R. J.; Heck, R. M. Catalytic Converters: State of the Art and Perspectives. *Catal. Today* **1999**, *51* (3–4), 351.

(24) Roy, S.; Bauer, T.; Al-Dahhan, M.; Lehner, P.; Turek, T. Monoliths as Multiphase Reactors: A Review. *AIChE J.* **2004**, *50* (11), 2918.

(25) Gadkaree, K. P. Carbon Honeycomb Structures for Adsorption Applications. *Carbon N. Y.* **1998**, *36* (7–8), 981.

(26) Nishihara, H.; Mukai, S. R.; Tamon, H. Preparation of Resorcinol–Formaldehyde Carbon Cryogel Microhoneycombs. *Carbon N. Y.* **2004**, *42* (4), 899.

(27) Yoshida, S.; Iwamura, S.; Ogino, I.; Mukai, S. R. Adsorption of Phenol in Flow Systems by a Monolithic Carbon Cryogel with a Microhoneycomb Structure. *Adsorption* **2016**, *22* (8), 1051.

(28) Mukai, S. R.; Nishihara, H.; Yoshida, T.; Taniguchi, K.; Tamon, H. Morphology of Resorcinol–Formaldehyde Gels Obtained through Ice-Templating. *Carbon N. Y.* **2005**, *43* (7), 1563.

(29) Nishihara, H.; Mukai, S. R.; Yamashita, D.; Tamon, H. Ordered Macroporous Silica by Ice Templating. *Chem. Mater.* **2005**, *17* (3), 683.

(30) Ahmadpour, A.; Do, D. D. The Preparation of Active Carbons from Coal by Chemical and Physical Activation. *Carbon N. Y.* **1996**, *34* (4), 471.

(31) Tamon, H.; Ishizaka, H.; Yamamoto, T.; Suzuki, T. Preparation of Mesoporous Carbon by Freeze Drying. *Carbon N. Y.* **1999**, *37* (12), 2049.

(32) Juang, R. S.; Tseng, R. L.; Wu, F. C. Role of Microporosity of Activated Carbons on Their Adsorption Abilities for Phenols and Dyes. *Adsorption* **2001**, *7* (1), 65.

(33) Kumar, A.; Kumar, S.; Kumar, S.; Gupta, D. Adsorption of Phenol and 4-Nitrophenol on Granular Activated Carbon in Basal Salt Medium: Equilibrium and Kinetics. *J. Hazard. Mater.* **2007**, *147* (1–2), 155.

(34) Srivastava, V. C.; Swamy, M. M.; Mall, I. D.; Prasad, B.; Mishra, I. M. Adsorptive Removal of Phenol by Bagasse Fly Ash and Activated Carbon: Equilibrium, Kinetics and Thermodynamics. *Colloids Surfaces A Physicochem. Eng. Asp.* **2006**, *272* (1–2), 89.

(35) Tsuchiya, T.; Mori, T.; Iwamura, S.; Ogino, I.; Mukai, S. R. Binderfree Synthesis of High-Surface-Area Carbon Electrodes via CO_2 Activation of Resorcinol–

Formaldehyde Carbon Xerogel Disks: Analysis of Activation Process. *Carbon N. Y.* **2014**, *76*, 240.

(36) Murakami, K.; Satoh, Y.; Ogino, I.; Mukai, S. R. Synthesis of a Monolithic Carbon-Based Acid Catalyst with a Honeycomb Structure for Flow Reaction Systems. *Ind. Eng. Chem. Res.* **2013**, *52* (44), 15372.

Chapter 5

Determination of Optimal Dimensions of Fiber Templated Carbon Gel Monoliths (FCGMs) via Breakthrough Curve Simulation

5.1 Introduction

In Chapter 4, a method to synthesize monoliths with introduced straight microchannels by fiber templating, was developed. The main advantage of the synthesis method is the ability to adjust the channel size and the channel density (void fraction) independently. However, as shown by the results for continuous phenol adsorption, there exists a proper range of channel size and void fraction so that the monolith can be used effectively under given process conditions. Since it is easy to adjust the dimensions of the monoliths using the fiber templating method, the method to calculate the optimal dimensions of the monolith is necessary.

The design guidelines of larger monolithic adsorbents were discussed in the literature, based on the performances on diffusion (both external and internal) and pressure drop.[1] In this chapter, similar concepts were applied in the determination of monolith dimensions, namely channel size and wall thickness of the fiber templated carbon gel monoliths (FCGMs). The coefficients related to mass transfer were determined from the breakthrough curves obtained from continuous adsorption of phenol, and the maximum channel size and wall thickness were determined from the limiting diffusion time required for the adsorbate. The data regarding mass transfer obtained from the breakthrough experiments conducted using FCGMs were also used for the simulation of a monolith with optimal dimensions, and compared with the theoretical data for the beds packed with particles having similar properties in mass transfer. Finally, the pressure drop across the FCGMs was calculated and compared with those of columns packed with particles to demonstrate the advantages in using the monolithic adsorbents.

5.2 Theory

5.2.1 Simulation of Breakthrough Curves

Mass balance of continuous adsorption in a bed, based on the convection-dispersion model, can be written as Eq. 5.1:[2,3]

$$-D_{\mathrm{L}}\frac{\partial^2 C}{\partial z^2}+\frac{\partial(v_{\mathrm{i}}\mathrm{C})}{\partial z}+\frac{\partial C}{\partial t}+\frac{(1-\varepsilon_{\mathrm{v}})}{\varepsilon_{\mathrm{v}}}\frac{\partial \bar{q}}{\partial t}=0 \qquad (5.1)$$

Here, D_L, C, z, v_i, t, ε_v, and $\bar{q}$ denote axial diffusivity, concentration of the substrate in the solution, axial distance from the entrance, interstitial velocity, time, void fraction of the monoliths (excluding the pores in the walls), and average uptake of the adsorbate, respectively.

In common practice, linear adsorption isotherm and linear driving force, given in Eq. 5.2, are used to simplify the equation without introducing unacceptable errors.[3]

$$\frac{\partial \bar{q}}{\partial t} = k\left(q^* - q\right) = kK(C - C^*) \tag{5.2}$$

Here, q^* denotes the uptake of the adsorbate in equilibrium with C, and C^* denotes the concentration in equilibrium with q. The parameters k and K are overall effective mass transfer coefficient and dimensionless Henry's law constant, respectively. The values of k and K are determined from experiments.

Generally, the axial diffusion term is neglected ($D_L = 0$), and the analytical solution of Eq. 5.1 and 5.2 is given as Eq. 5.3:[4,5]

$$\frac{C}{C_0} = \frac{1}{2}\left[1 + \mathrm{erf}(\sqrt{\tau} - \sqrt{\xi} + \frac{1}{8\sqrt{\tau}} + \frac{1}{8\sqrt{\xi}})\right] \tag{5.3}$$

Here, C_0 denotes the feed concentration. τ, ξ, and erf denote the dimensionless time, dimensionless distance, and the error function, the definitions given in Eq. 5.4, 5.5, and 5.6, respectively.

$$\tau = k\left(t - \frac{L}{v_i}\right) \tag{5.4}$$

$$\xi = \frac{kKL}{v_i}\left(\frac{1 - \varepsilon_v}{\varepsilon_v}\right) \tag{5.5}$$

$$\mathrm{erf}(x) = \frac{2}{\sqrt{\pi}}\int_0^x \exp(-s^2)\, ds \tag{5.6}$$

Here, L is the length of the bed.

The length of unused bed (LUB) is a useful parameter to indicate the effectiveness of the adsorption and is calculated by Eq. 5.7:

$$\mathrm{LUB} = \frac{L}{t_s}\ (t_s - t_b) \tag{5.7}$$

Here, t_s and t_b denote the time when the breakthrough ratio is 0.5 (stoichiometric time) and 0.05 (breaktime), respectively.

5.2.2 Resistances in Mass Transfer and Diffusion Time

It is assumed that overall resistance in mass transfer (the reciprocal of kK) is the sum of the resistance from external mass transfer and intraparticle mass transfer (Eq. 5.8)

$$\frac{1}{kK}=\frac{1}{a_{\mathrm{v}}k_{\mathrm{f}}}+\frac{1}{k_{\mathrm{p}}D_{\mathrm{e}}} \tag{5.8}$$

Here, a_{v}, k_{f}, k_{p}, and D_{e} denote the external surface area of the adsorbent (in FCGMs, the total lateral surface area of the channels) per unit volume, external mass transfer coefficient, intraparticle mass transfer coefficient, and effective intraparticle diffusivity, respectively.

The value of external mass transfer coefficient k_{f} can be estimated from the correlation for Sherwood number Sh represented by Eq. 5.9:

$$Sh=\frac{k_{\mathrm{f}}D}{D_{\mathrm{m}}}=Sh_{\infty}\left[1+c\left(\frac{D}{L}\right)ReSc\right]^{0.45} \tag{5.9}$$

Here, D_{m}, Sh_{∞}, c, D, Re, and Sc denote the molecular diffusivity of the adsorbate, asymptotic Sherwood number for fully developed flow inside the channels, tube roughness constant, channel size, Reynolds number, and Schmidt number, respectively. The value of Sh_{∞} was set to 3.66 for circular channels, and a typical value of c is 0.095.[6] The value of D_{m} for phenol in water is 1.018×10^{-9} m^2 s^{-1}.[7] The values of Re and Sc were defined by Eq. 5.10 and 5.11:

$$Re=\frac{\rho D v_{\mathrm{i}}}{\mu} \tag{5.10}$$

$$Sc=\frac{\mu}{\rho D_{\mathrm{m}}} \tag{5.11}$$

Here, ρ and μ denote the density and the dynamic viscosity of the fluid, respectively. Since the channel size of the monoliths is much smaller than the length of the monolith (the ratio between D and L is less than 0.01), then the Sherwood number reaches the asymptotic value. Therefore, the value of 3.66 was used in this work.

The intraparticle mass transfer coefficient k_{p} of the monolith can be estimated by that of a hollow cylinder with insulated external surface shown in Eq. 5.12:[1]

$$k_{\mathrm{p}}=\frac{4}{\left\{\left[\left(\frac{r_{\mathrm{o}}}{r_{\mathrm{i}}}\right)-1\right]\left(r_{\mathrm{o}}^2-r_{\mathrm{i}}^2\right)-\left(\frac{1}{r_{\mathrm{i}}(r_{\mathrm{o}}-r_{\mathrm{i}})}\right)\left[\frac{1}{2}\left(r_{\mathrm{o}}^4-r_{\mathrm{i}}^4\right)-\frac{4r_{\mathrm{o}}}{3}\left(r_{\mathrm{o}}^3-r_{\mathrm{i}}^3\right)+r_{\mathrm{o}}^2\left(r_{\mathrm{o}}^2-r_{\mathrm{i}}^2\right)\right]\right\}} \tag{5.12}$$

Here, r_{o} and r_{i} denote the outer and inner radius of the model hollow cylinder. In the case of FCGMs, the inner radius r_{i} is equal to the channel radius (D/2). The outer radius r_{o} can be

estimated by the ideal monolith geometry with equally-spaced channels and is represented by Eq. 5.13:

$$r_o = \sqrt{\frac{\pi}{2\sqrt{3}\varepsilon_v}}\, r_i \tag{5.13}$$

After obtaining the value of effective intraparticle diffusivity D_e from Eq. 5.8, the diffusion time for external and intraparticle diffusion steps, t_{ext} and t_{int}, can be calculated by Eq. 5.14 and 5.15, respectively:

$$t_{ext} = \frac{r_i^2}{2D_m} \tag{5.14}$$

$$t_{int} = \frac{T^2}{4D_e} \tag{5.15}$$

Here, T denotes the average wall thickness of the FCGMs calculated by Eq. 5.16:

$$T = D\left(\sqrt{\frac{\pi}{2\sqrt{3}\cdot\varepsilon_v}} - 1\right) \tag{5.16}$$

To illustrate the performance of FCGMs in continuous adsorption, breakthrough curves of beds packed with spherical particles of uniform size were simulated. The equation for total resistance in mass transfer (Eq. 5.8) can be rewritten as Eq. 5.17:[8]

$$\frac{1}{kK} = \frac{d_p}{6k_f} + \frac{d_p^2}{60D_e} \tag{5.17}$$

Here, d_p is the particle diameter. The external mass transfer coefficient k_f of packed bed of particles at low Reynolds number can be calculated from Eq. 5.18:[9]

$$\frac{k_f}{v_s} Sc^{0.58} = 2.40 \left(\frac{Re_p}{\varepsilon_v}\right)^{-0.66} \tag{5.18}$$

The Schmidt number Sc has the same definition as Eq. 5.11. The Reynolds number Re_p can be calculated by Eq. 5.19. Note that Eq. 5.18 is valid for the values of Re_p/ε_v in the range of 0.08 to 125.

$$Re_p = \frac{\rho d_p v_s}{\mu} \tag{5.19}$$

5.2.3 Critical Void Fraction

When the values of D_e was determined, the critical void fraction in which the time required for external diffusion step and the intraparticle diffusion step is equal can be calculated (Eq. 5.20):

$$\frac{T^2}{D^2}=\frac{D_e}{D_m} \tag{5.20}$$

By rearrangement and substitution of Eq. 5.20 into Eq. 5.16, the critical void fraction $\varepsilon_{v,c}$ is represented by Eq. 5.21:

$$\varepsilon_{v,c}=\frac{\pi}{2\sqrt{3}}\left(\frac{1}{\sqrt{D_e/D_m}+1}\right)^2 \tag{5.21}$$

5.2.4 Pressure Drop

Similar to the procedures in the previous chapters, the pressure drop caused by the liquid flow through the monolith is calculated by the Hagen–Poiseuille equation (Eq. 5.23), assuming laminar flow inside the channels:

$$\Delta P = \frac{32\mu v_s L}{\varepsilon_v D^2} \tag{5.23}$$

Here, v_s denotes the superficial ("empty-tower") velocity of the fluid. For comparison, the pressure drop across a packed bed of particles is calculated by the Kozeny–Carman equation (Eq. 5.24):

$$\Delta P = 36k\frac{(1-\varepsilon_v)^2}{\varepsilon_v{}^3}\frac{\mu v_s L}{d_p{}^2} \tag{5.24}$$

Here, k denotes the Kozeny–Carman constant. The values of k and ε_v were respectively set to 5 and 0.4, typical values for a bed packed with spherical particles.

5.3 Experimental Section

The FCGMs used in the experiments were synthesized by the method discussed in Chapter 4. The channel sizes of the synthesized monolith were 60, 93, 126 and 160 μm, the void fraction of the monoliths were in the range of 0.19–0.50, and the burn-off ratio (B.O.) were in the range of 15–19%.

Breakthrough experiments were conducted using 100 ppm phenol in water at 30 °C in the system shown in Fig. 5.1. Samples were pretreated under vacuum at 120 °C for 2h, and were fixed in a heat shrinkable FEP tube (FEP-070, AS ONE, inner diameter after heating: 6.0 mm),

which was connected to stainless steel pipes and placed in an oven (CTO-10A V, Shimadzu). Phenol concentration was measured by a UV-visible detector (SPD-10A VP, Shimadzu) set at a wavelength of 270 nm. The breakthrough curves were plotted and analyzed by the equations described in the previous section. After determination of k, K and D_e from the breakthrough curves, the curves for packed bed of particles were simulated assuming equal bed mass and fluid superficial velocity. The adsorption capacity (K) and intraparticle diffusivity (D_e) were set to be the same as in the case of FCGMs. Three breakthrough curves for the packed bed system were simulated based on equal surface area per volume a_v, equal intraparticle mass transfer coefficient k_p, and equal response. The particle diameter for each case was determined, and the pressure drop caused by such beds were calculated and compared with the value of FCGMs.

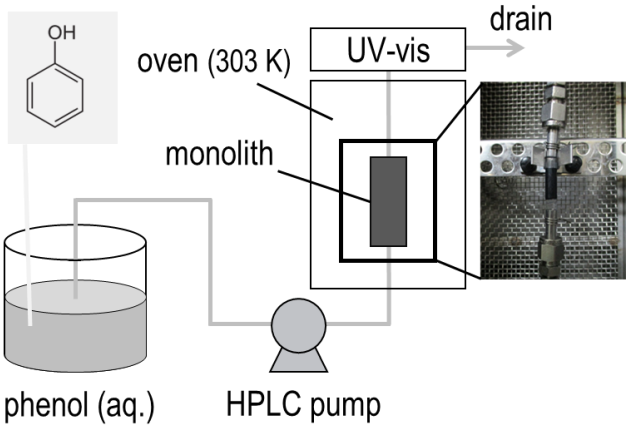

Fig. 5.1 Schematic setting of the continuous flow adsorption system. The photograph shows a typical sample in a FEP tube, connected to stainless steel pipes, inside the oven

5.4 Results and Discussion

5.4.1 Simulation of Breakthrough Curves

Fig. 5.2 shows a breakthrough curve obtained from the continuous adsorption experiment using a FCGM (D = 60 μm, ε_v = 0.19). Because the breakpoint (breakthrough ratio: 0.05) and the stoichiometric point (breakthrough ratio: 0.5) are usually used in calculations regarding continuous adsorption, only the data points from the beginning of the experiments until the breakthrough ratio reached just above 0.5 were used in the curve fitting. The values of parameters for the simulation of breakthrough curves, and the calculated diffusion time for each step are shown in Table 5.1. Note that the value of D_e should be obtained from experiment(s) with intraparticle diffusion as the rate limiting step. Therefore, the value of 3.88

$\times 10^{-10}$ m^2 s^{-1} was used for the calculation of intraparticle diffusion time. This diffusivity value is comparable to those reported for other carbon adsorbents.[10,11] It can be seen that the experiments conducted under mass transfer limitation have the longest diffusion time of 1.63 s and above. Therefore, the limiting time range was set to 1.06–1.63 s for continuous adsorption of phenol at 30 °C, C_0 of 100 ppm and v_s of 3 cm min^{-1}. The critical void fraction $\varepsilon_{v,c}$ was calculated to be 0.35, so the limiting channel size and wall thickness were in the range of 93–115 μm and 57–71 μm, respectively.

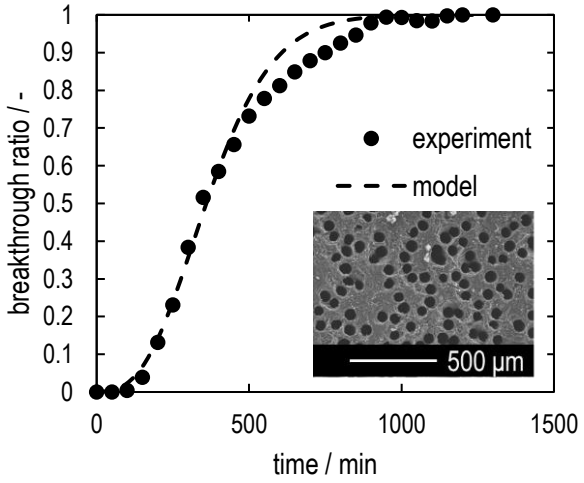

Fig. 5.2 Breakthrough curve of a FCGM (D = 60 μm, ε_v = 0.19, B.O. = 15%) for continuous adsorption of 100 ppm phenol in water at 30 °C (v_s: 3.0 cm min^{-1}). The inset shows SEM image of the sample

Table 5.1 Parameters for the simulation of breakthrough curves and calculated diffusion time (B.O. = 15–19%, residence time ≈ 30 s)

channel size D / μm	60	60	60	93	160
void fraction ε_v / -	0.19	0.39	0.50	0.39	0.39
wall thickness T / μm	71	31	21	49	84
superficial velocity v_s / cm min^{-1}			3.0		
interstitial velocity v_i / cm min^{-1}	15.8	7.7	6.0	7.7	7.7
overall effective mass transfer coefficient k / 10^{-4} s^{-1}	4.3	18.1	44.8	30.8	6.1
dimensionless Henry' law constant K / -	732	1202	788	1206	1171
external mass transfer coefficient k_f / 10^{-5} m s^{-1}	6.21	6.21	6.21	4.01	2.33
surface area per volume a_v / 10^3 m^2 m^{-3}	12.7	26.0	33.3	16.8	9.8
intraparticle mass transfer coefficient k_p / 10^9 m^{-2}	1.36	9.11	22.8	3.79	1.28
effective intraparticle diffusivity D_e / 10^{-10} m^2 s^{-1}	3.88	neg[a]	neg[a]	neg[a]	neg[a]
length of unused bed LUB[b] / mm	10.9	5.5	4.3	4.9	11.5
external diffusion time t_{ext} / s	0.44	0.44	0.44	1.06	3.14
intraparticle diffusion time t_{int} / s	1.63	0.32	0.14	0.77	2.27

[a] Negative value (intraparticle diffusion is not a rate limiting step)

[b] Sample length of 20 mm

The prediction of adsorption efficiency was then conducted for a FCGM with channel size D of 126 μm (synthesized using 151 μm fishing lines, YGK Yoz-ami) and void fraction ε_v of 0.43, which was not included in the determination of limiting diffusion time. Although the relatively high void fraction of the sample resulted in thin walls (57 μm, corresponding to t_{int} of 1.05 s), the large channel size would increase the time required for external diffusion. Since calculated

diffusion time exceeds the limit (t_{ext}: 1.95 s), mass transfer limitation should be observed. Fig. 5.3 shows the resulting breakthrough curve and the curve simulated from experimental data. The calculated k was 1.84×10^{-4} s^{-1} and LUB was 12.5 mm, which clearly indicates mass transfer limitation in agreement with the prediction. Therefore, the use of diffusion time is one of the useful ways to limit the size range in the design of a monolith.

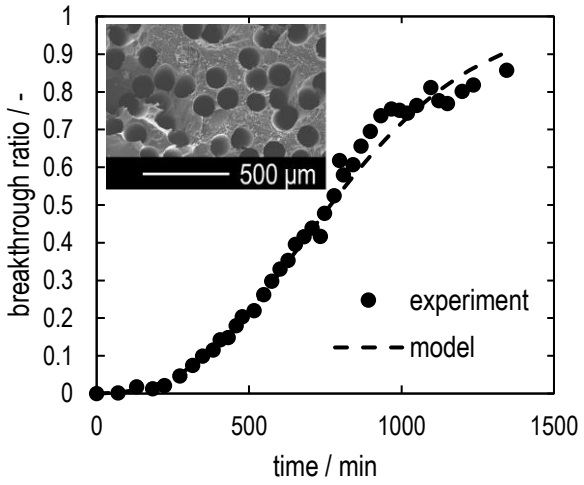

Fig. 5.3 Breakthrough curve of a FCGM (D = 126 µm, ε_v = 0.43, B.O. 17%) for continuous adsorption of 100 ppm phenol in water at 30 °C (v_s: 3.0 cm min^{-1}). The inset shows SEM image of the sample

To use the limiting diffusion time for the prediction of adsorption experiments with different feed flow rate, the concept of residence time (or space velocity) was introduced. The residence time is frequently used in catalysis and reactor design. However, it is less frequently mentioned in the field of adsorption. The work regarding the use of a carbon honeycomb (larger size) showed that the resulting breakthrough curves are the same for process conditions with the same residence time, although the fluid velocity were different.[12] Fig. 5.4 shows the breakthrough curves of FCGMs with a channel size D of 93 µm and a void fraction ε_v of 0.39, with different residence time. The system with 15 s residence time should have the limiting diffusion time half as long as the system with 30 s residence time. So the new limiting diffusion time was 0.5–0.8 s, which is shorter than the longest diffusion time of the monolith (1.06 s). Therefore, mass transfer limitation was observed (k: 4.69×10^{-4} s^{-1} and LUB: 13.1 mm for a 23-mm long sample).

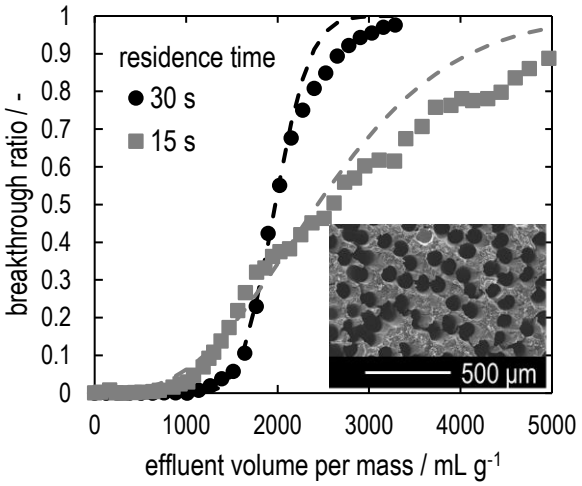

Fig. 5.4 Breakthrough curves of FCGMs (D = 93 μm, ε_v = 0.39, B.O. = 17–19%) for continuous adsorption of 100 ppm phenol in water at 30 °C (v_s: 3.0 or 6.0 cm min^{-1}, corresponding to residence time of 30 or 15 s). The inset shows SEM image of the samples, and the dashed lines show simulation results of the curves

The use of diffusion time for the design of FCGMs could be summarized as follows. Note that the method can be applied to any adsorbate in general, as long as the value of D_m is known.

1. Determine the value of D_e from breakthrough curves of the systems with intraparticle mass transfer limitation (small channel size and thick walls) using Eq. 5.3–5.13.

2. Calculate the critical void fraction $\varepsilon_{v,c}$ using Eq. 5.21.

3. Calculate the diffusion times from Eq. 5.14 and 5.15. If t_{ext} is longer than t_{int} (external mass transfer limited), redo the experiment using samples with smaller channels and/or thicker walls.

4. Calculate the limiting values of channel size and wall thickness.

The monoliths with smaller sizes than the limit may also be used. However, the pressure drop might also increase and prevent the use of such monolith under high flow rate.

5.4.2 Pressure Drop

In continuous flow processes, the pressure drop across the bed is usually reported in length basis. Conversely, the capacity of the adsorbent is usually reported in mass basis. Therefore, it is preferred to convert the pressure drop data from length-based values to mass-based values so that the pressure drop values of monoliths having the same adsorption capacity can be directly compared. The values were calculated with respect to those of the monolith with ε_v =

0.40 and are plotted in Fig. 5.5. The minimum pressure drop per mass was found at $\varepsilon_v = 0.50$. The operation cost (from pump power) would be lowest at this void fraction. On the other hand, samples with ε_v near 0.4 would cause slightly higher pressure drops. However, the required monolith length would be about 80% of the samples with $\varepsilon_v = 0.50$. Therefore, equipment cost could be minimized in this case. It should also be noted that the calculated critical void fraction $\varepsilon_{v,c}$ coincidentally fell into this range.

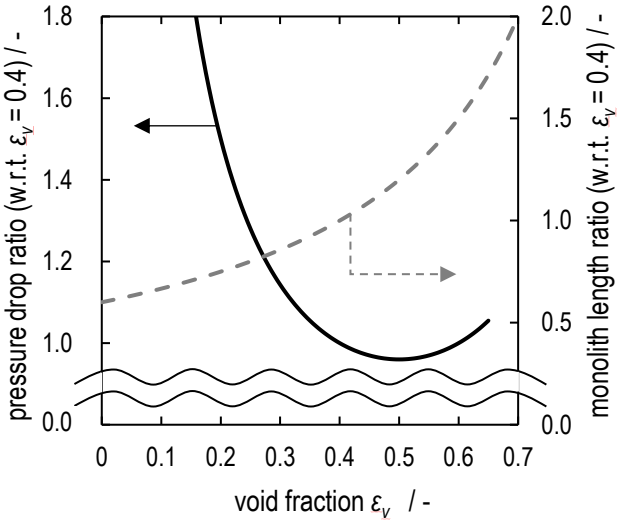

Fig. 5.5 pressure drop ratio and monolith length ratio with respect to those of a monolith having $\varepsilon_v = 0.4$ with equal mass

5.4.3 Comparison with a Packed Bed of Particles

The breakthrough curve for phenol adsorption was simulated for a 20-cm sample with D = 93 μm and $\varepsilon_v = 0.35$ ($\varepsilon_v = \varepsilon_{v,c}$ and $t_{ext} = t_{int}$ =1.06 s) and compared with simulated breakthrough curves of beds filled with spherical particles having the same mass and used under the same process conditions. The particle sizes used for the simulation was selected to be the values given equal surface area per volume a_v (case 1), equal intraparticle mass transfer coefficient k_p (case 2), and equal response (case 3), respectively. The breakthrough curves are shown in Fig. 5.6, and the simulation parameters, as well as calculated LUB and pressure drop are shown in Table 5.2, respectively. It has been discussed in the literature that monolith adsorbents should be designed so that intraparticle mass transfer is adequate in the case of larger honeycombs.[1] When this was considered in the simulation, it can be seen that FCGMs were superior to beds packed with particles, thanks to their short diffusion path length. Although it is possible to find the particle size to give the same response as the systems using FCGMs, the pressure drop

caused by the bed would be far higher than that caused by the FCGMs. The simulated results could be used to emphasize the advantage of using FCGMs over conventional packed beds, that it is possible to have adsorption systems with short diffusion path length (rapid intraparticle mass transfer) and low hydraulic resistance at the same time.

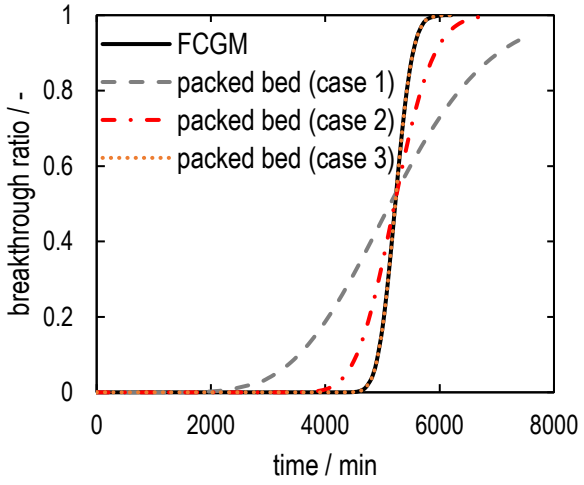

Fig. 5.6 Simulated breakthrough curve of a 20-cm long FCGM (D = 93 μm, ε_v = 0.35), compared with the curves of beds packed with particles. The particle diameters were selected to have equal surface area per volume a_v (case 1), equal intraparticle mass transfer coefficient k_p (case 2), and equal response (case 3), as the FCGM

Table 5.2 Parameters for the simulation of breakthrough curves of a FCGM and packed beds of particles having equal surface area per volume a_v (case 1), equal intraparticle mass transfer coefficient k_p (case 2), and equal response (case 3)

	FCGM	**packed bed (case 1)**	**packed bed (case 2)**	**packed bed (case 3)**
void fraction ε_v / -	0.35	0.40	0.40	0.40
bed length L / m	0.20	0.22	0.22	0.22
characteristic length D or d_p / μm	93	402	151	64
intersititial velocity v_i / cm min^{-1}	8.57	7.50	7.50	7.50
pressure drop ΔP / kPa	0.852	0.588	3.84	21.4

Table 5.2 Parameters for the simulation of breakthrough curves of a FCGM and packed beds of particles having equal surface area per volume a_v (case 1), equal intraparticle mass transfer coefficient k_p (case 2), and equal response (case 3) (continued)

	FCGM	**packed bed (case 1)**	**packed bed (case 2)**	**packed bed (case 3)**
overall effective mass transfer coefficient k / 10^{-4} s^{-1}	30.8	0.932	6.07	30.9
external mass transfer coefficient k_f / 10^{-5} m s^{-1}	4.01	3.41	6.51	11.5
surface area per volume a_v / 10^3 m^2 m^{-3}	14.9	14.9	39.7	93.8
intraparticle mass transfer coefficient k_p / 10^9 m^{-2}	2.63	0.371	2.63	14.6
length of unused bed LUB / mm	14.7	84.5	35.2	16.0

5.5 Conclusions

In this chapter, the optimal dimensions of FCGMs for continuous phenol adsorption were determined via the simulation of breakthrough curves. The concept of limiting diffusion time was introduced to determine whether a monolith would suffer from mass transfer limitations under given process conditions. The use of this concept not only proved successful in predicting the behavior of adsorption systems using monoliths having different dimensions from the training dataset, but also be able to predict the behavior of the systems with different residence time. The guideline of using the limiting diffusion time for the design of FCGMs was also established to obtain the optimal dimensions. Finally, the simulated breakthrough curve of a FCGM having optimal dimensions was compared with those of beds packed with spherical particles, and the results showed that FCGMs could perform better both in terms of diffusion and pressure drop. This emphasize the advantage of using FCGMs for applications in continuous adsorption.

References

(1) Patton, A.; Crittenden, B. D.; Perera, S. P. Use of the Linear Driving Force Approximation to Guide the Design of Monolithic Adsorbents. *Chem. Eng. Res. Des.* **2004**, *82* (8), 999.

(2) Henley, E. J.; Seader, J. D.; Roper, D. K. *Separation Process Principles*, 3rd ed.; John Wiley & Sons (Asia): Hoboken, NJ, 2011.

(3) Ruthven, D. M. *Principle of Adsorption and Adsorption Processes*; Wiley: New York, 1984.

(4) Klinkenberg, A. Numerical Evaluation of Equations Describing Transient Heat and Mass Transfer in Packed Solids. *Ind. Eng. Chem.* **1948**, *40* (10), 1992.

(5) Klinkenberg, A. Heat Transfer in Cross-Flow Heat Exchangers and Packed Beds. *Ind. Eng. Chem.* **1954**, *46* (11), 43.

(6) Hawthorn, R. D. Afterburner Catalysts—Effects of Heat and Mass Transfer between Gas and Catalyst Surface. *AIChE-IChemE Symp. Ser.* **1974**, *70*, 428.

(7) Niesner, R.; Heintz, A. Diffusion Coefficients of Aromatics in Aqueous Solution. *J. Chem. Eng. Data* **2000**, *45* (6), 1121.

(8) Glueckauf, E. Theory of Chromatography. Part 10.—Formulæ for Diffusion into Spheres and Their Application to Chromatography. *Trans. Faraday Soc.* **1955**, *51*, 1540.

(9) Williamson, J. E.; Bazaire, K. E.; Geankoplis, C. J. Liquid-Phase Mass Transfer at Low Reynolds Numbers. *Ind. Eng. Chem. Fundam.* **1963**, *2* (2), 126.

(10) Bhatia, S. K.; Kalam, A.; Joglekar, H. S.; Joshi, J. B. Effective Diffusivity of Phenol in Activated Carbon. *Chem. Eng. Commun.* **1990**, *98* (1), 139.

(11) Srivastava, V. C.; Swamy, M. M.; Mall, I. D.; Prasad, B.; Mishra, I. M. Adsorptive Removal of Phenol by Bagasse Fly Ash and Activated Carbon: Equilibrium, Kinetics and Thermodynamics. *Colloids Surfaces A Physicochem. Eng. Asp.* **2006**, *272* (1–2), 89.

(12) Gadkaree, K. P. Carbon Honeycomb Structures for Adsorption Applications. *Carbon N. Y.* **1998**, *36* (7–8), 981.

Chapter 6

Conclusions

Soluble aromatics in wastewater could cause serious effects to health and the environment, even at ppm-level concentrations. Several treatment techniques are suggested for the treatment of these compounds, including adsorption and photocatalysis. Although these two techniques show many promising treatment results, mass transfer limitations usually occurring in the systems limits their performance. In this work, the use of monoliths with introduced microchannels was suggested to overcome the mass transfer limitations in continuous treatment of soluble aromatics in wastewater. These miniaturized version of conventional honeycomb monoliths can be thought as a combination between larger monolithic honeycombs and numbered-up microdevices. The thin walls and straight microchannels formed between these walls are shown to facilitate mass transfer while minimizing pressure drop across the monoliths under fluid flow as well. The synthesis methods, as well as the applications of the monoliths, were investigated.

In Chapter 2, TiO_2−SiO_2 microhoneycomb photocatalysts were synthesized from ice templating method using an inexpensive sodium silicate solution as SiO_2 precursor, which resembles the production of silica gels in industries. The use of reactive alkoxides of Ti was avoided by using a commercial TiO_2 sol as a source. Samples with a microhoneycomb morphology containing 25 mol% TiO_2 could be obtained similar to the synthesis method using alkoxides as precursors previously reported in the literature. The channel size of the samples was 26 μm on average, surrounded by thin walls of up to 5 μm. These straight microchannels were effective in reducing the pressure drop across the bed to less than a hundredth of that of the beds packed with particle with the same diffusion path length. The microhoneycombs also had high BET surface area of over 500 m^2 g^{-1}. Their high surface area led to improved photocatalytic activities compared with disk-type photocatalysts, both in batch and continuous flow systems. The effect of calcination temperature to the specific surface area and the photocatalytic activity of the samples was also investigated. Although TiO_2 in the microhoneycombs could retain the all-anatase phase even after calcination at 1000 °C, the decrease in specific surface area after calcination led to lower photocatalytic activity. The results indicate the importance of photocatalysts with high specific surface area, which could be realized in uncalcined TiO_2−SiO_2 microhoneycombs synthesized by the ice templating method.

In Chapter 3, the synthesis method for TiO_2−SiO_2 microhoneycomb photocatalysts based on sodium silicate solution was further improved. Two sources of commercial TiO_2 sol, stabilized at different pH, were used so that it is possible to control the morphology (via pH adjustment) independently from TiO_2 content. This synthesis method resulted in uniform distribution of TiO_2 inside a SiO_2 matrix, so 10 mol% samples synthesized by the improved method had photocatalytic activity as high as the 25 mol% samples synthesized by the previous method. The microhoneycombs calcined at 600–800 °C had higher crushing strength than the uncalcined samples, as well as higher photocatalytic activity due to the change in surface properties and structure densification, while still retaining a high BET surface area of more than 500 $m^2\ g^{-1}$. In addition, it was found that the microhoneycomb morphology was effective not only for minimizing the pressure drop of the system while retaining rapid mass transfer, but also for uniform distribution of fluid flow, compared with systems packed with particles having identical adsorption properties as the microhoneycombs. The results indicates the potential of TiO_2−SiO_2 microhoneycombs to be used as photocatalysts in continuous flow systems under various process demands.

In Chapter 4, a new synthesis method to synthesize monoliths with straight microchannels, the fiber templating method, was developed. Straight polyester fibers with circular cross section were selected as templates because they decompose at high temperatures, leaving only a trace of themselves behind. The method also allows independent control of channel size and channel density by adjusting the size and the amount of fibers, respectively. Carbon gel monoliths with introduced microchannels were successfully synthesized by the fiber templating method. The synthesized monoliths also have adequate strength to be activated, and samples having BET surface area as high as 1630 $m^2\ g^{-1}$ could be obtained at a burn-off ratio of 47%, without altering the overall morphology. The monoliths also showed high adsorption capacities of phenol in water, both in batch and continuous systems. It was found that a monolith with a channel size between 60 and 93 μm and a wall thickness of up to 70 μm could effectively adsorb phenol at the superficial velocity of 3 cm min^{-1}, and the length of unused bed of these samples were 5 mm or less even when the length of the monolith was 20 mm. The results show the high potential of the synthesized monoliths to be used for continuous adsorption of phenol.

In Chapter 5, the optimal dimensions (channel size and wall thickness) of the monoliths synthesized by the fiber templating method were investigated. The breakthrough curves obtained from continuous adsorption experiments were fitted with theoretical equations to obtain parameters in mass transfer. The concept of limiting diffusion time was introduced to

determine the rate limiting mass transfer step, as well as to predict whether a monolith with given dimensions would suffer from mass transfer limitations under a certain set of process conditions. It was found that this concept could correctly predict the behavior of systems with the monolith having dimensions different from the experiments used for the determination of limiting diffusion time, and systems with different process conditions. The guideline to determine an optimal dimensions of the monoliths from breakthrough experiments was established. Finally, the breakthrough curve of a monolith having optimal dimensions was simulated and compared with simulated curves of beds packed with spherical particles. It was found that the monolith could effectively adsorb phenol while causing minimal pressure drop, which is difficult to realize in packed bed systems. The results confirm the advantages of using the fiber templating method to synthesize the monoliths to be used in continuous adsorption.

In summary, this work shows the potential of monolithic materials with introduced straight microchannels to be used in continuous treatment of soluble aromatics in wastewater. The high surface area, as well as thin walls of the samples could facilitate both mass and radiative transport, while the straight channels could minimize the pressure drop occurring under a continuous fluid flow, as well as uniformly distribute the fluid flowing through the monoliths. The results indicate that monoliths with introduced straight microchannels are suitable to improve the performance of materials used for continuous wastewater treatment.

Research Achievements

Original Papers

1. Kasama Urkasame, Seiichiro Yoshida, Taihei Takanohashi, Shinichiroh Iwamura, Isao Ogino, and Shin R. Mukai. Development of TiO_2–SiO_2 Photocatalysts Having a Microhoneycomb Structure by the Ice Templating Method. *ACS Omega* **2018**, 3, 14274–14279.
2. Kazuya Takahashi, Seiichiro Yoshida, Kasama Urkasame, Shinichiroh Iwamura, Isao Ogino, and Shin R. Mukai. Carbon gel monoliths with introduced straight microchannels for phenol adsorption. *Adsorption* **2019**, 25, 1241–1249.

International Conferences

1. Kasama Urkasame, Seiichiro Yoshida, Shinichiroh Iwamura, Isao Ogino, and Shin R. Mukai. Evaluation of TiO_2–SiO_2 Microhoneycomb Photocatalysts Using Model Simulation. The 10th International Conference on Multifunctional Materials and Applications, 2016.12.01–03, Khon Kaen, Thailand, Oral.
2. Kasama Urkasame, Seiichiro Yoshida, Shinichiroh Iwamura, Isao Ogino, and Shin R. Mukai. Model Simulation of Continuous Flow Photocatalytic Systems with TiO_2–SiO_2 Microhoneycombs. 16th Korea-Japan Symposium on Catalysis & 3rd International Symposium of Institute for Catalysis, 2017.05.15–17, Sapporo, Japan, Poster.
3. Kasama Urkasame, Seiichiro Yoshida, Shinichiroh Iwamura, Isao Ogino, and Shin R. Mukai. Improvement of Flow Behavior in Continuous Flow Photocatalytic Reaction Using TiO_2–SiO_2 Microhoneycombs. Pre-conference of TOCAT8 and the 5th International Symposium of Institute for Catalysis, 2018.08.03–04, Sapporo, Japan, Poster.
4. Kasama Urkasame, Seiichiro Yoshida, Shinichiroh Iwamura, Isao Ogino, and Shin R. Mukai. Effect of Calcination Temperature to Adsorption and Photocatalytic Properties of TiO_2–SiO_2 Microhoneycombs. 8th Pacific Basin Conference on Adsorption Science and Technology, 2018.09.03–06, Sapporo, Japan, Poster.
5. Kazuya Takahashi, Seiichiro Yoshida, Kasama Urkasame, Shinichiroh Iwamura, Isao Ogino, and Shin R. Mukai. Carbon Gel Monoliths with Introduced Straight Microchannels for Phenol Adsorption. 8th Pacific Basin Conference on Adsorption Science and Technology, 2018.09.03–06, Sapporo, Japan, Poster.

Awards

1. Otsuka Hiroshi Sensei Memorial Award, Graduate School of Chemical Sciences and Engineering, Hokkaido University, 2017.03.23

Acknowledgements

At the time of writing this, I still cannot believe I have spent more than five years doing research in Japan. I have realized that this thesis could not be finished without the help and support from many people, so I would like to use this opportunity to express my gratitude to them.

First of all, I would like to thank my advisor, Prof. Shin R. Mukai. Before entering the graduate program, I would focus on only the research topic of my to-be advisor. But he showed me that not only he has impressive knowledge in the related fields, but also he has the kindness and patience to guide me through my graduate program. He also truly listened to me during discussions, and his word selection during the discussions was very careful. This surely inspired me to be not only a better researcher, but a better person in general.

I would like to thank Assoc. Prof. Isao Ogino for his careful checking of my work, which became a part of my standard for experiments and academic writing. (Yes, there were the periods I would bring research papers to read in the restaurant queue!) I would also like to express my gratitude to Asst. Prof. Shinichiroh Iwamura for his first checking of my work. Actually, the flow of the first draft of my work looked nothing like the final version, and the mediocre would have been released to the public without his checking.

I also deeply appreciate the comments and questions from the committee during my defense, especially from Prof. Takao Masuda and Prof. Atsushi Fukuoka. Their comments surely helped improving my thesis, as well as giving ideas for the future work.

Sincere gratitude would go to Dr. Seiichiro Yoshida, who acted as my mentor during his stay in the laboratory for his Ph.D. program. His advices and emotional support made me go through the hard time and failures during my work. I also appreciate the help from Ms. Akane Kunifuji for both technical and general support in the laboratory.

I would also like to thank the members of Laboratory of Material Design and Engineering for their support. Especially Mr. Taihei Takanohashi for Chapter 2, as well as Mr. Kazuya Takahashi, Mr. Hiroyuki Mega, and Mr. Takuya Sugawara for Chapter 4. This thesis could not be completed without their contribution.

I have been given an opportunity to be a teaching assistant for the undergraduate laboratory class during the second year of my Ph.D. program. I would like to express my gratitude to Asst. Prof. Haruo Kumagai who trusted me to do the job in a class taught in Japanese, even though I am not a native speaker. The experiences from the class are surely valuable.

I would like to thank the Government of Japan for giving me an opportunity and the scholarship to study here without worrying too much about the financial problems. I also thank Assoc. Prof. Tawatchai Charinpanitkul of Chulalongkorn University for introducing me Hokkaido University and this wonderful laboratory.

The professors I met during my undergraduate program in Thailand also made a great contribution during my graduate program in Japan. I would like to thank my advisor during my undergraduate program, Assoc. Prof. Tharathon Mongkhonsi, who is a role model mainly for the research ethics and experimental set-up. I also would like to express my gratitude to the late Assoc. Prof. M.L. Supakanok Thongyai. He taught me how to use the solver function in Excel, which I mainly used to obtain the results in Chapter 5. He will forever be remembered.

Doing research would be much more difficult with personal issues, and I would like to thank the counselor of the Office of International Affairs, Dr. Harue Ishii, for helping me going through the hard time during the beginning of my Ph.D. Because of her, I had tried many new things and could fully enjoy my life during the Ph.D. program.

I would like to thank my parents and my sister. Thesis writing is not easy, and it is difficult for someone who has never gone through the writing process to understand these difficulties. Fortunately, my sister was also writing her graduation thesis during my Ph.D. course. The advices I gave her not only contribute in her success, but also motivates myself to improve my writing as well.

Finally, I would also like to thank all of my friends from all over the world. The distance is never a problem for them to send me love and support.